universität wien

MASTERARBEIT / MASTER'S THESIS

Titel der Masterarbeit / Title of the Master's Thesis

„Geochemical investigation of impactites from the Boltysh impact structure and possible relationship to early Danian sediments from the Umbria-Marche Basin, Italy"

verfasst von / submitted by

Sophia Wernitznig BSc

angestrebter akademischer Grad / in partial fulfilment of the requirements for the degree of

Master of Science (MSc)

Wien, 2023 / Vienna 2023

Studienkennzahl lt. Studienblatt / degree programme code as it appears on the student record sheet:	UA 066 815
Studienrichtung lt. Studienblatt / degree programme as it appears on the student record sheet:	Masterstudium Erdwissenschaften
Betreut von / Supervisor:	Univ. -Prof. Dr. Christian Koeberl
Mitbetreut von / Co-Supervisor:	Dipl.-Min. Dr. Toni Schulz

Acknowledgment

I would like to thank all those who have supported me during the process of my master thesis and all those who have contributed to it.

I would especially like to thank my supervisor Univ.-Prof. Dr. Christian Koeberl for making this master's thesis possible for me and supporting me throughout the entire process. I am grateful for his investment in the outcome of this thesis and the opportunity to work in this field.

Special thanks also go out to my co-supervisor Dipl.-Min. Dr. Toni Schulz, who took the time teaching me the necessary laboratory and analytically knowledge to obtain my results and also helping me throughout the writing process.

I am also very grateful to Mag. Dr. Dieter Mader for measuring the INAA samples and his ongoing support.

Many thanks to Dr. Alessandro Montanari for supplying the Italian samples and making this whole thesis possible.

Lastly, I want to thank my amazing family and friends, who supported me every step of the way.

Abstract

The 65.4 Ma old, ~24 km diameter Boltysh impact structure is located in central Ukraine and despite extensive geochemical studies conducted by various authors, the Boltysh impactites have not yet been investigated with regards to their Os concentrations and Os isotopic composition. The recent $^{40}Ar/^{39}Ar$ age dating by Pickersgill et al. (2021) of the Boltysh impact structure coincides with the astronomical age of the so-called ALE ash layer in the Danian pelagic succession of the Scaglia Rossa formation in the Umbria-Mache sequence, Italy. This coincidence raises the question if there is a possible connection between the Boltysh impact event and the ALE ash layer. Distal ejecta from the Boltysh impact might have been deposited in the Scaglia Rossa formation in form of the ALE ash.

The ALE ash layer occurs in three Italian sections, at Morello, Bottaccione, and Contessa Highway. This study attempts a search for a meteoritic component in the ALE ash layer of those sections to evaluate a possible connection to the Boltysh impact structure. Six Boltysh impactites and twenty samples of the three Italian sites, comprising ALE ash samples and carbonate samples from underneath and above the ALE ash, were studied in this thesis. Geochemical analyses of trace element abundances were conducted with INAA and highly siderophile elements (HSEs), along with Os isotopic compositions, were measured using isotope-dilution mass spectrometry.

Meteoritic signatures were found in at least two of the Boltysh impactites, exhibiting near-chondritic $^{187}Os/^{188}Os$ ratios of 0.13 and small Ir abundance anomalies (0.16-0.36 ppm Ir). Potential meteoritic signatures have also been identified within the ALE ash layers or the adjacent layers, indicating the possible deposition of Boltysh ejecta within/as the ALE ash in the Danian pelagic succession in Italy. Although some degree of alteration might have led to minor leaching of HSEs, their elevated concentrations, in combination with lower $^{187}Os/^{188}Os$ ratios (of 0.16-0.23), in the ALE ash and its adjacent layers relative to the carbonates indicate the possibility that a minor meteoritic contribution is present in the ALE ash. Although the age dating shows that the deposition of the ALE ash coincides with the Boltysh impact event, and a potential meteoritic component has been identified in the ALE ash layer, a definitive connection with Boltysh cannot be confirmed unequivocally.

Zusammenfassung

Die 65.4 Millionen Jahre alte Boltysh Impaktstruktur befindet sich im Zentrum der Ukraine und trotz umfangreichen geochemischen Studien wurden bisher weder Osmiumkonzentrationen noch Osmium-Isotopen-Zusammensetzungen gemessen. Die neueste $^{40}Ar/^{39}Ar$ Altersdatierung des Boltysh Ereignisses von Pickersgill et al. (2021) stimmt mit dem Alter der sogenannten ALE-ash in der pelagischen Abfolge der Scaglia Rossa Formation in Mittelitalien überein. Dies wirft die Frage auf, ob das Boltysh Impaktereignis mit der Ablagerung der „ALE ash“ in Verbindung gebracht werden kann. Distale Ablagerungen, die während des Boltysh Impaktereignisses entstanden sind, könnten sich in der Scaglia Rossa Formation als ALE ash abgelagert haben.

Die ALE ash ist in drei italienischen Aufschlüssen (Morello, Bottaccione und Contessa Highway) in der Nähe von Gubbio zu finden. Im Rahmen dieser Masterarbeit wurde versucht, eine meteoritische Komponente in der ALE ash zu finden und eine Verbindung mit dem Boltysh Impaktereignis zu untersuchen. Dazu wurden sechs Impaktgesteine von Boltysh, zusammen mit zwanzig Proben der italienischen Aufschlüsse -darunter ALE ash- und Karbonatproben-, geochemisch analysiert. Spurenelementanalysen wurden mithilfe von INAA durchgeführt und hoch-siderophile Elemente, sowie die Os-Isotopen-Zusammensetzung, wurden mittels Isotopenverdünnungsanalyse und Massenspektrometrie gemessen.

Meteoritische Signaturen mit nahezu chondritischen $^{187}Os/^{188}Os$ Verhältnissen von 0.13 und kleinen Ir Anomalien (von 0.16-0.36 ppm) wurden in zumindest zwei Boltysh Impaktiten gefunden. Ebenso wurden in den ALE ash und den angrenzenden Karbonatlagen meteoritische Signaturen gefunden. Zusammen mit dem übereinstimmenden Alter von Boltysh und der ALE ash deutet das auf eine Ablagerung distaler Auswürfe des Boltysh Impaktereignisses in oder als ALE ash Lage hin. In den italienischen Aufschlüssen kam es vermutlich durch Verwitterungsprozesse zu einer Mobilisation von HSEs, weshalb die meteoritische Signatur in manche, an die ALE ash-angrenzende, Lagen gewandert ist. Trotzdem findet man in der ALE ash und angrenzenden Lagen für terrestrisches Krustenmaterial untypisch hohe HSE-Konzentrationen und unradiogene Os-Isotopen-Zusammensetzungen ($^{187}Os/^{188}Os$ = 0.16-0.23), die durch meteoritische Kontamination erklärt werden kann.

Table of Contents

CHAPTER 1

Introduction

1.1. Thesis Objectives

The objective of this master's thesis is to perform geochemical analyses of melt rocks and suevites from the 24-km-diameter Boltysh impact crater in Ukraine and the coeval so-called "ALE ash" from Central Italy. At a distance of about 1600 km from the Boltysh impact structure, the ALE ash layer can be found in three Italian sections: Morello, Bottaccione, and Contessa Highway (see Figure 1); samples from each section were investigated in this study. In these outcrops, the ALE ash is located about two meters above the K-Pg boundary, and its origin is so far unknown. The recently published $^{40}Ar/^{39}Ar$ age of 65.39 ± 0.14/0.16 Ma of the Boltysh impact structure by Pickersgill et al. (2021) is consistent with the estimated astronomical age of the ALE ash (65.440 ± 0.005 Ma; Sinnesael et al. 2016), raising the question of whether the ALE ash could be related to the Boltysh impact event, as distal impact ejecta. To test this assumption, a meteoritic signature is being searched for in samples from the ALE ash. If such a geochemical signature is present, it may be connected to the Boltysh impact event. Units above and underneath the ALE ash were also sampled for comparison.

In addition, a first analysis of the Re-Os isotopic composition of melt rocks and suevites from the Boltysh impact structure is attempted. Additional information about the geochemistry of the Boltysh impactites may help with the correlation to potential distal ejecta.

To do so, this study focuses on determining the concentrations of selected highly siderophile elements (Re, Os, Ir, Pt, Ru, and Pd) and the Re-Os isotopic composition of samples from impact melt rocks and suevites of the Boltysh impact structure and from the Italian ALE ash. This was done using isotope dilution for the determination of element concentrations and isotope composition analysis via mass spectrometry (TIMS). In addition, instrumental neutron activation analyses (INAA) were used to determine minor and trace element concentrations of the samples and to provide further insight into the geochemistry of these rocks. This study aims to contribute to the investigations made so far on the Boltysh impact melt rocks and breccias and attempts to determine the possible presence of a meteoritic signature in the ALE

ash, to constrain the possible relationship between the ALE ash layer in Italy and the Boltysh impact event in Ukraine.

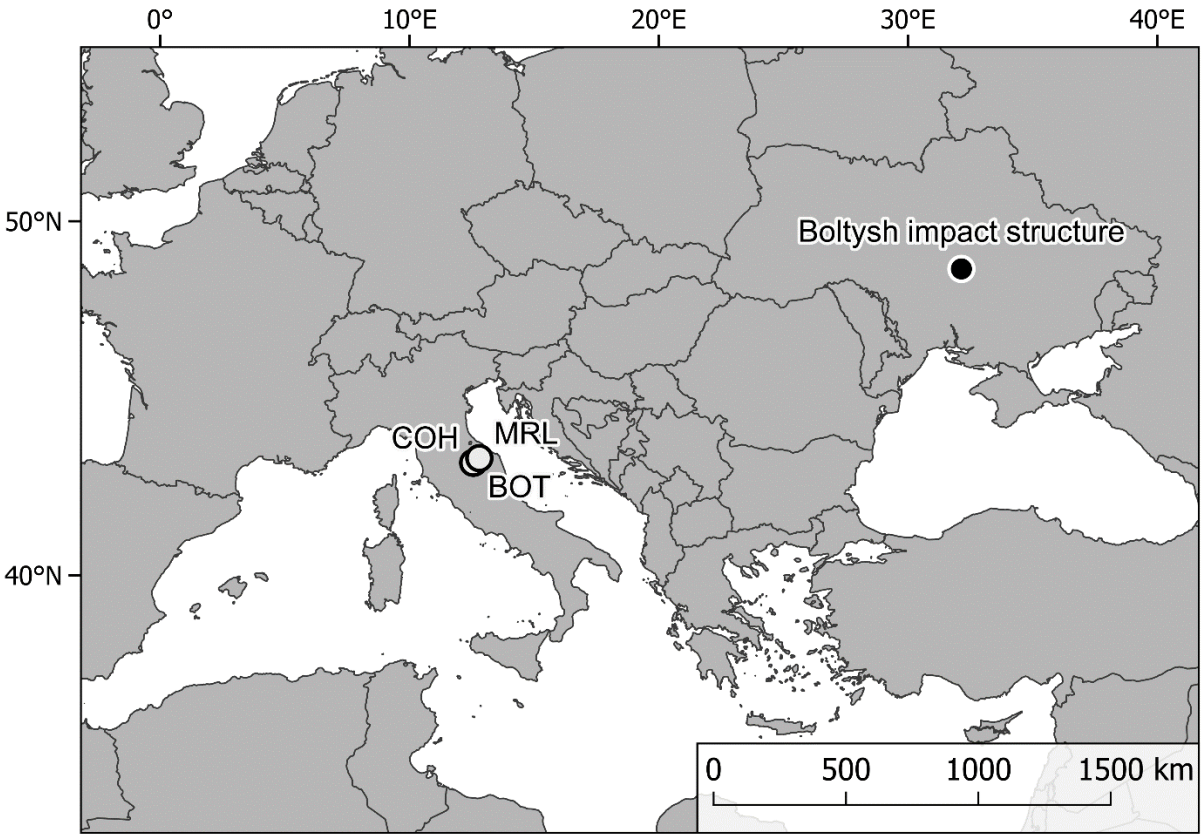

Figure 1. *Location of the Italian sections Morello (MRL), Bottaccione (BOT), and Contessa Highway (COH), and the Boltysh impact structure in Ukraine (the Bottaccione and Contessa Highway section overlap in this figure). The present-day distance between the impact structure and the pelagic sections is approximately 1600 km.*

1.2. Meteorite Impacts and Crater Formation

Impact craters are one of the most common geological features in the solar system. They are present on nearly all solid planetary bodies, such as rocky terrestrial planets, moons, and asteroids. Unlike on Earth, impact craters are often the dominant landform on the surface of planets and moons. Due to various geological processes on Earth, such as plate tectonics, vulcanism, and erosion, the surface of the Earth is continuously renewed. Therefore, many, especially older impact craters, are covered up or erased from the rock record. Despite this, numerous impact craters have been found on Earth; one of the first to be identified as such was studied from 1906 onwards by Daniel M. Barringer: the Meteor Crater in Arizona (e.g., Shoemaker 1987; Osinski and Pierazzo 2012). To date, 190 confirmed impact structures have been identified on Earth, according to the Earth Impact Database (2023). One of the largest known terrestrial impact structures is located in Sudbury (Canada), it has an estimated (pre-deformation) diameter of about 180 km, although the diameter is difficult to determine, due to the heavy level of erosion (e.g., Grieve and Shoemaker 1994). One of the most famous impact structures is the ca. 200-km-diameter Chicxulub impact structure in Yucatán, Mexico. Based on the spatial overlap between the Chicxulub impact event and the Cretaceous-Paleogene (K-Pg) boundary, as well as Ir-anomalies at various K-Pg boundaries, it is widely accepted that the Chicxulub impact caused the devastating mass extinction event at the end of the Cretaceous (e.g., Schulte et al. 2010).

1.2.1. Crater Morphology

It is necessary to distinguish between an impact crater and an impact structure. Impact craters are the unaltered result of the impact itself, whereas an impact structure is what can be observed today after alteration, erosion, and burial over a long period of time (e.g., Koeberl 2013). Impact craters can be divided into two main groups based on their morphology: simple and complex craters (e.g., Melosh 1989; Grieve and Shoemaker 1994). Simple craters are characterized by a bowl-shaped depression and a small, uplifted, and overturned rim (e.g., Melosh 1989, Grieve and Robertson 1987). The low level of shock suggests that the lithologies of simple craters are formed by slumping of the cavity walls, rather than deposition during fallback (e.g., Osinski and Pierazzo 2012). Simple craters usually are small in diameter, limited to a maximum of 2-4 km diameter on Earth, depending on the properties of the target rock (e.g., Grieve and Robertson 1987; Melosh 1989; Koeberl 2013). Complex craters, on the other hand, have larger diameters (>2-4 km), but are usually shallower in depth

relative to their diameter (e.g., Grieve and Robertson 1987; Koeberl 2013). A characteristic feature of complex craters is the central uplift in the crater, where rocks from the deep underground are brought closer to the surface (e.g., Grieve and Robertson 1987; Koeberl 2013). Due to erosional processes and sediment deposition on Earth, some of the crater morphology can be lost. In most cases, the crater rims visible today are only the remains of previously much higher crater rims, and/or belong to young craters. Over time the crater depression is filled with post-impact sediments, slowly burying the entire structure (e.g., Koeberl 2006; Osinski and Pierazzo 2012). There are some craters that have been completely buried, such as the Chicxulub impact structure in Mexico or the Boltysh crater in Ukraine (Grieve et al. 1987; Grieve and Shoemaker 1994).

1.2.2. Formation of Impact Craters

When an extraterrestrial body (projectile) hits the Earth's surface, with cosmic velocities of about 11-72 km/s, a large amount of kinetic energy is released (e.g., Melosh 1989; Koeberl 2013). The formation of the crater is a very rapid process, that can be divided into three main phases: (1) contact and compression, (2) excavation, and (3) post-impact modification (e.g., Melosh 1989; Koeberl 2013). In the first stage, the projectile, an asteroid, or a comet, hits the surface of the target, converting its kinetic energy into shock waves that penetrate the target material. This leads to the compression of the target rocks, resulting in shock metamorphism, melting, and/or vaporization of the rocks. The shock waves also propagate into the projectile, when they reach the upper surface of the projectile, they are reflected back in the form of rarefaction waves, causing almost instantaneous melting and vaporization of the projectile (e.g., Melosh 1989). In the following excavation stage, the actual crater is formed. A hemispherical shock wave penetrates the target rock, causing it to fracture and be ejected outward. The interaction of outward-propagating shock waves and the downward-directed rarefaction waves results in the excavation of a bowl-shaped depression, a "transient cavity" (e.g., Melosh 1989). The ejected material forms the ejecta blanket, while part of the melt rocks and rock debris remains in the transient cavity, forming the crater-fill impactites. Eventually, the shock and rarefaction waves have lost so much energy that they can no longer excavate and move target material (e.g., Melosh 1989). In the modification stage, the fate of the crater form depends on whether it is a simple or complex crater. Simple craters, undergo only minor modifications, resulting in a bowl-shaped crater with a small crater rim (similar to the original rim of the transient cavity). Due to the mere size of the complex crater, it succumbs to the gravitational forces and initially collapses, while the center of the crater rises

and forms the uplift (e.g., Melosh 1989; Osinski and Pierazzo 2012). The excavation phase takes place in only 1-2 minutes, even in large craters (e.g., Koeberl 2013).

1.2.3. Impactites

Under the extreme conditions of an impact event, the material of the projectile and the target rock is transported and mixed, whereas part of it is melted and vaporized. The term "impactite" refers to all rocks affected by a hypervelocity impact, on Earth or other planetary bodies. They can be divided into proximal impactites, which are deposited up to three radii around the crater, and distal impactites, which can be deposited over much greater distances. Stöffler and Grieve (2007) classified the wide variety of impactites (from a single impact event) into three main groups, based on texture, degree of shock metamorphism, and lithological components: (1) shocked rocks, (2) impact melt rocks, and (3) impact breccias (see Figure 2) (Stöffler and Grieve 2007).

(1) Shocked rocks, as part of the proximal impactites, represent non-brecciated rocks, which have effects of shock metamorphism, but no melt content. They can further be classified based on their progressive stage of shock metamorphism (Stöffler and Grieve 2007).

(2) Impact melt rocks consist of molten, generally mixed, target rocks and can contain both shocked and unshocked minerals and lithic clasts (Osinski and Pierazzo 2012). They can be divided into three subgroups depending on their clast content: clast-rich, clast-poor, and clast-free. According to their crystallinity, they can be further divided, into glassy, hypocrystalline, and holocrystalline melt rocks (Stöffler and Grieve 2007). Impact melt rocks usually have similar compositions to their target rocks, especially in large craters, where a large amount of continental crust is transformed into melt rock (e.g., Osinski and Pierazzo 2012; Koeberl 2014). While melt rocks can occur in impact breccias or dykes, the majority of melt rocks form a coherent melt sheet above the crater floor (e.g., Osinski and Pierazzo 2012).

(3) Impact breccias are divided into three subgroups as well, based on their components and the degree of mixing. The components can be remains of the target rocks or melt rocks. Monomict breccias contain only target rock components with almost no shock metamorphism. Lithic breccias are polymict breccias with a matrix composed of only

lithic and mineral clasts. If the matrix of such a polymict breccia additionally contains melt particles, then it is called a suevite breccia (Stöffler and Grieve 2007).

(4) Tektites and microtektites, which are distal impactites, represent natural glasses that are chemically homogeneous. While they are only a few centimeters in size, tektites often have a spherically symmetrical shape. Their formation is not yet fully understood, but they are likely formed by melting and quenching of terrestrial rocks during the impact. Besides tektites on land, so-called "microtektites" were found in deep-sea cores. They are smaller than tektites, usually smaller than one millimeter in diameter. Both tektites and microtektites can be transported over great distances and occur in strewn fields, which can be far from the crater itself. Currently, there are four known strewn fields on Earth, for example, the Central European strewn field, which has been correlated with the Ries impact structure in Germany. The correlation is possible due to age dating and the similar physical, chemical, and petrological properties of the tektites (e.g., Koeberl 2013, 2014).

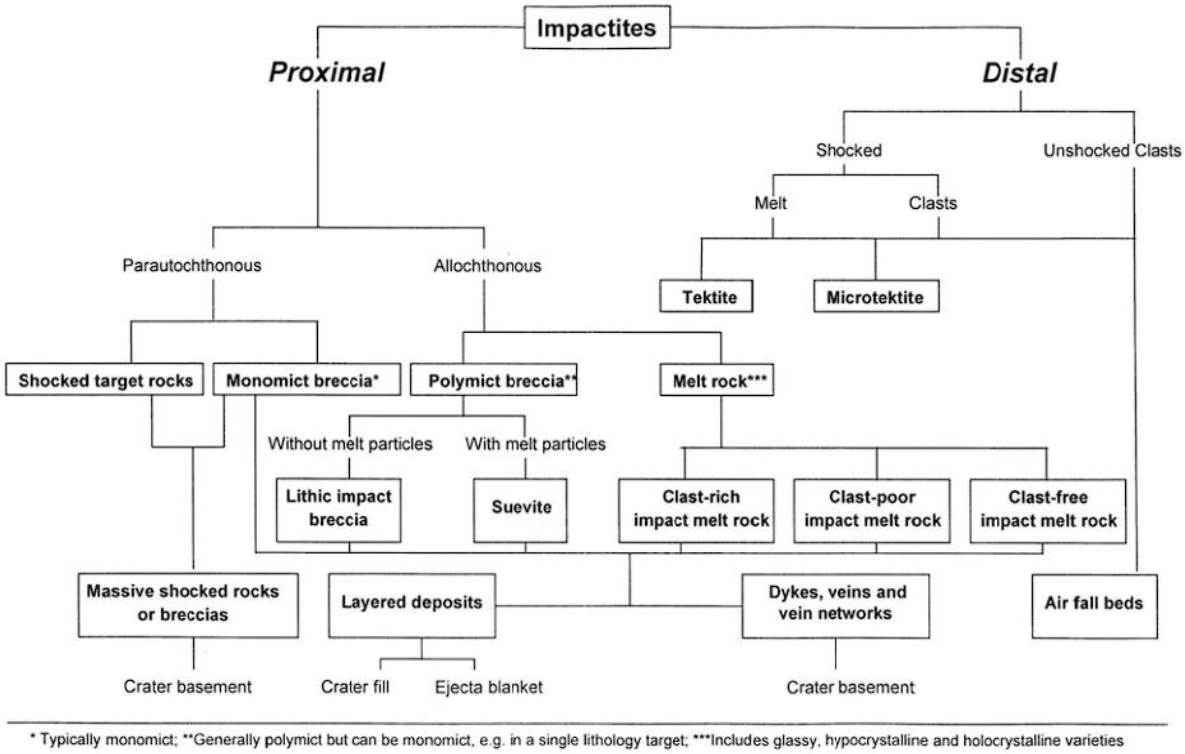

Figure 2. *Classification of impactites of single impact events, based on location, texture, composition, and degree of shock metamorphism (from Stöffler and Grieve 2007).*

1.2.4. Shock Metamorphism

The passage of high-pressure shock waves through the rock during impact leads to specific changes in the target rocks and minerals; this process is called shock metamorphism (cf. French and Koeberl 2010). The features of shock metamorphism are only known to be (naturally) generated by hypervelocity impacts and are, therefore, unambiguous evidence or indication of impact events (e.g., French and Koeberl 2010). Within a few seconds, the structural order of rocks and minerals is broken by the extreme pressure and temperature, straining and quenching the rock (e.g., Langenhorst and Deutsch 2012). Depending on different shock pressures, certain shock features occur. Planar deformation features (PDFs) in minerals (e.g., quartz, feldspar) are characteristic of shock metamorphism. They form at pressures >10 GPa and can only be found in impactites (French and Koeberl 2010; Koeberl 2013). Maskelynite glass, high-pressure mineral phases such as coesite and stishovite, and even impact diamonds can also form under these conditions (French and Koeberl 2010; Koeberl 2013). At lower pressures (2-10 GPa), shatter cones can form in the target rocks, which is the only macroscopic feature, that can be exhibited in form of cone-shaped striated features on fracture planes (e.g., French and Koeberl 2010).

1.2.5. Geochemistry of Impactites

Aside from the mineralogical and physical characteristics that can develop during impact, there are several geochemical tools for the identification of impact structures. Because there are many geological processes, such as volcanism (calderas), collapse structures, or subsidence, that can form shapes similar to impact structures, methods to distinguish between impact structures and other non-impact generated landforms are necessary (e.g., Koeberl 2014). In most cases, no projectile fragments sustain the impact, but during the vaporization and melting of the projectile and target rock, a small amount of meteoritic material is incorporated into the impact breccia and melt rocks (e.g., Koeberl 1998; Koeberl et al. 2012). Since the impactor is diluted by much larger volumes of target rock, the amount of meteoritic material in impactites is very small (usually <1 wt%), but the quantity is often sufficient enough to detect the extraterrestrial signature in impactites using analytical methods (e.g., Koeberl 1998).

1.2.5.1. Moderately and Highly Siderophile Elements

The contents of the highly siderophile elements (HSEs), as well as Cr, Co, and Ni, can be used to identify the presence of a meteoritic signature in melt rocks and impact breccias. These siderophile elements are present in meteorites and asteroids in much higher concentrations (by several orders of magnitudes) than in the continental crust (e.g., Koeberl et al. 2012). Even if only minor amounts of meteoritic components are present in impactites, elevated levels of the HSEs can often be measured analytically (Koeberl 2014).

The concentrations of Cr, Co, and Ni (collectively termed moderately siderophile elements), as well as their interelement ratios, have been used in the past to determine meteoritic signatures and, in some cases, even the type of meteorite involved. Since there is a wide variety of meteorites with different geochemical compositions, it is sometimes possible to estimate, or at least narrow down, the type of impactor. However, the abundances of Cr, Co, and Ni in the continental crust can be just as high as in meteorites; therefore, the characterization of meteorites using this technique must be done with caution and can only be achieved when a substantial amount of meteoritic material was admixed to the impactites (i.e. percent level). In addition, an extensive petrographic and geochemical inspection of the impact and target rocks, as well as mixing calculations are necessary to obtain reasonable results (e.g., Koeberl 1998; Koeberl et al. 2002; Mougel et al. 2019).

A different method to detect evidence of meteoritic signatures is to measure the abundances of the platinum-group elements: ruthenium (Ru), rhodium (Rh), palladium (Pd), osmium (Os), iridium (Ir), and platinum (Pt) (e.g., Koeberl 2014). Sometimes the gold (Au) and rhenium (Re) abundances are measured as well, because of their similar properties. Together they represent the Highly Siderophile Elements (HSEs), which are elements with a strong affinity for metallic iron (cf. Rollinson and Pease 2021). The abundances of these elements are significantly higher in most meteorites compared to the values in the terrestrial crust. In addition, the interelement ratios of the PGEs are different in meteorites. Typical Os and Ir concentrations in chondrites vary between 400 and 900 ppb and 350 and 800 ppb, respectively, with Os/Ir ratios of 1.0-1.1 (Fischer-Gödde et al. 2010). In contrast, the average terrestrial upper continental crust (UCC) has concentrations of only about 0.031 ppb Os and 0.022 ppb Ir and an Os/Ir ratio of about 1.5 (Peucker-Ehrenbrink and Jahn 2001). In the absence of any other terrestrial enrichment processes (e.g., mafic contamination or hydrothermal overprint), distinctly elevated levels of PGEs in impactites compared to target rock abundances can thus indicate a chondritic or iron projectile (Koeberl et al. 2012). In

contrast, achondritic projectiles have relatively low abundances of the PGEs and are, therefore, much more difficult to detect (Koeberl et al. 2012).

1.2.5.2. The Re-Os Isotope System

The rhenium-osmium (Re-Os) isotopic system has been extensively used in the field of geochronology and geochemistry, particularly in the study of meteorites and impactites. It is based on the β^- decay of ^{187}Re to ^{187}Os with a half-life of 42.3 ± 1.3 Ga (e.g., Shirey and Walker 1998). Due to the long half-lives of the Re isotope, the Re-Os system was used for the age dating of meteorites and processes that took place in the early stages of the solar system (e.g., Herr et al. 1961; Luck et al. 1980; Shen et al. 1996; Smoliar et al. 1996).

In addition to age dating of meteorites, the Re-Os isotopic system has been successfully used in various studies to determine meteoritic signatures in impactites and ejecta layers (see e.g., Turekian 1982; Koeberl and Shirey 1993; Meisel et al. 1995; Koeberl and Shirey 1996; Frei and Frei 2002; Lee et al. 2006; Schulz et al. 2017; Daly et al. 2018; Ozdemir et al. 2019). Most meteorites, with the exception of achondrites (meteorites with low Re and Os concentrations that underwent magmatic differentiation), have high Os and moderately high Re contents (e.g., Mason 1971; Koeberl and Shirey 1997; Koeberl 1998; Fischer-Gödde et al. 2010). As already mentioned above, the Os concentration is several orders of magnitude higher in chondrites than in terrestrial crustal rocks. The Re content of the UCC with an average of 198 ppb (Peucker-Ehrenbrink and Jahn 2001) is slightly higher compared to chondrites with values ranging from 40 to 100 ppb (e.g., Shirey and Walker 1998; Walker et al. 2002; Tagle and Berlin 2008; Fischer-Gödde et al. 2010). This results in chondritic Re/Os ratios that are less or equal to 0.1, whereas the terrestrial crust (UCC) has ratios greater than 10 (e.g., Peucker-Ehrenbrink and Jahn 2001; Koeberl 2014).

Rhenium and osmium were some of the first elements to condense in the early stages of our solar system, due to their high condensation temperatures (Wasson 1985). During the formation of the Earth, the terrestrial crust incorporated relatively high amounts of incompatible Re, resulting in elevated Re/Os ratios compared to the depleted mantle (e.g., Shirey and Walker 1998; Dabek and Halas 2007). Over time, this led to accumulation of the radiogenic ^{187}Os isotope due to the decay of ^{187}Re (e.g., Koeberl and Shirey 1997; Shirey and Walker 1998, Rollinson and Pease 2021). Chondrites, on the other hand, which incorporated small amounts of Re at their formation, have only slightly radiogenic $^{187}Os/^{188}Os$ signatures (e.g., Morgan and Lovering 1976; Shirey and Walker 1998; Rollinson and Pease 2021). A

non-radiogenic, stable Os isotope (^{188}Os or less often ^{186}Os) is used as a reference isotope to normalize the abundance of the radiogenic ^{187}Os (and other Os and Re isotopes) during mass spectrometric analyses. Consequently, the ^{187}Os/^{188}Os ratio in chondrites is much lower than in crustal rocks on Earth.

The accumulation of radiogenic ^{187}Os can be described by the equation:

$$^{187}\mathrm{Os}/^{188}\mathrm{Os} = (^{187}\mathrm{Os}/^{188}\mathrm{Os})_i + (^{187}\mathrm{Re}/^{188}\mathrm{Os})(e^{\lambda t} - 1)$$

where ^{187}Os/^{188}Os and $^{187}\mathrm{Re}/^{188}\mathrm{Os}$ are the ratios that can be measured today, $(^{187}\mathrm{Os}/^{188}\mathrm{Os})_i$ is the initial isotopic ratio at system closure, $(e^{\lambda t} - 1)$ is the function of radioactive decay, with the decay constant λ for ^{187}Re, and t is the time since the system was closed with respect to Re and Os (e.g., Shirey and Walker 1998).

Meteorites have low ^{187}Os/^{188}Os ratios of about 0.11-0.18 (Luck et al. 1980; Walker and Morgan 1989; Horan et al. 1992; Morgan et al. 1992; Smoliar et al. 1996), which includes chondrites with ratios around 0.12-0.13 (e.g., Walker et al. 2002; Fischer-Gödde et al. 2010), whereas the UCC has a more radiogenic Os isotopic composition, with an average ^{187}Os/^{188}Os ratio of about 1.4 (Peuker-Ehrenbrink et al. 2001).

Earth's mantle rocks also have Os isotopic ratios that are similar to chondritic values. The primitive upper mantle (PUM) has ^{187}Os/^{188}Os ratio of 0.13 (e.g., Meisel et al. 1996, 2001; Sun et al. 1998; Day et al. 2017). Therefore, it is necessary to carefully study the target rocks of an impact structure, because admixture of mantle material (mafic rocks) could lower the Os isotopic composition of the impactites. The HSE content of mantle rocks is much lower than in chondrites; therefore, the source of the unradiogenic Os isotopic composition in an impactite can be distinguished by measuring the HSE concentrations. If their concentrations are distinctly elevated, compared to the target rocks, then the unradiogenic composition might be due to an admixture of meteoritic material (e.g., Turekian 1982; Koeberl et al. 1996; Koeberl and Shirey 1997; Koeberl et al. 2012). In addition, other chemical data (elemental and isotopic abundances) can or should be used to detect the possible admixture of significant amounts of terrestrial (ultra)mafic material (e.g., Koeberl 1998).

Therefore, an admixture of mantle material in the target rocks can be distinguished from an incorporation of a meteoritic component (see Koeberl et al. 2012). The mixing of meteoritic material and crustal target rock results in a distinct change in Os isotope composition and a change in Os abundance, which can be analytically measured. The sensibility of the Re-Os

isotope tool is very high, so that even minor proportions of a meteoritic component, on the order of >0.1%, can be identified (e.g., Koeberl 1998, 2014; Koeberl et al. 2012).

The isochron diagram of the Re-Os system allows for the dating of the formation age of rocks and minerals. As time passes, Re decays into Os, and the ratio of Re to Os changes accordingly. Therefore, the slope of the isochron line on the graph represents the rate of Re decay over time. However, it is essential to consider that some geological processes can lead to mixing of different Re/Os ratios over time, which results in the irregular distribution of data points on the graph (e.g., Reiners et al. 2018). Therefore, the Re-Os isochron diagram can be used as mixing diagram of target rock material and meteoritic components (see Figure 3.1) (e.g., Koeberl 2014; Reiners et al. 2018). The target rock, being terrestrial material from the upper continental crust, plots in the upper right corner with radiogenic Os isotopic composition, while chondrites plot in the bottom left corner of the diagram. In between are the impactites, with Os isotopic signatures that resulted from the mixing of target rock and meteoritic material.

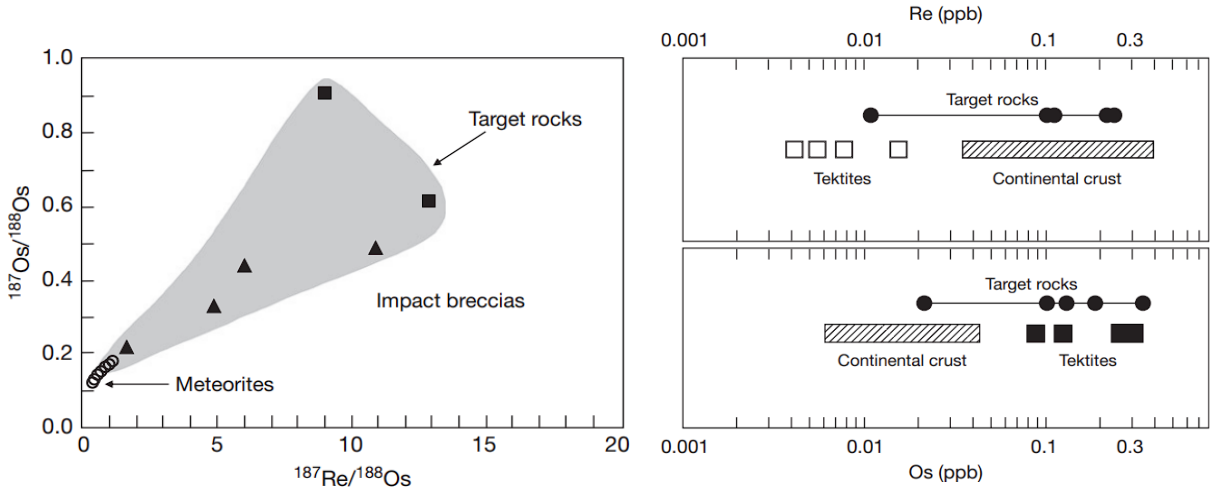

Figure 3.1. *Rhenium and Os isotope diagram for impact breccias and target rocks of the Kalkkop impact structure in South Africa, from Koeberl (2014). The squares represent target rock samples, while the triangles are different impact breccia samples. The circles display meteorite data. This diagram shows the mixing of meteorite and target rock material, resulting in impactites like impact breccias. The Os and Re isotope ratios of the impactites result from the different isotopic compositions of the target rocks and meteorites.*

Figure 3.2. *Osmium and Re concentrations of different terrestrial and extraterrestrial materials from Koeberl (2014). The continental crust has higher Re but lower Os concentrations. In comparison, tektites have low Re and high Os contents. In this case, the target rocks can be diverse in their Re and Os concentrations but tend to have Re concentrations similar to those of the continental crust, and Os concentrations of the tektites are somewhat higher.*

1.2.5.3. Chromium Isotopes

The radioactive nuclide ^{53}Mn decays with a half-life of only 3.7 Ma to the stable daughter nuclide ^{53}Cr (e.g., Honda and Imamura 1971). Although ^{53}Mn was present in the formation of the first solids in our solar system, it has now become extinct due to its short half-life (e.g., Lugmair and Shukolykov 1998). As the formation of Earth was a long time ago, terrestrial rocks do not now show any deviations in the ^{53}Cr/^{52}Cr ratio. In most meteorites, which formed very early in the solar system when ^{53}Mn was still present, the decay of ^{53}Mn led to an excess of ^{53}Cr and a higher ^{53}Cr/^{52}Cr ratio compared to terrestrial rocks (e.g., Shukolyukov and Lugmair 1998). The deviation to the terrestrial ^{53}Cr/^{52}Cr ratio is usually given in ε units, which corresponds to 1 part in 10^4 or 0.01 %. Determination of the Cr isotope composition in impactites can help to identify the type of meteorite involved in the impact. Elevated ^{53}Cr/^{52}Cr ratios, relative to terrestrial rocks, can be seen in carbonaceous, ordinary, and enstatite chondrites, and some differentiated meteorites (Lugmair and Shukolykov 1998 and references therein). Depending on the type of meteorite, the values correspond to around -0.1 to +0.3 ε (e.g., Lugmair and Shukolyukov 1998; Trinquier et al. 2008; Koeberl et al. 2012). Due to the different values of Cr isotopes in impactites, compared to terrestrial rocks, the presence of a meteoritic signature can be determined and, in some cases, even the nature of the impactor can be estimated.

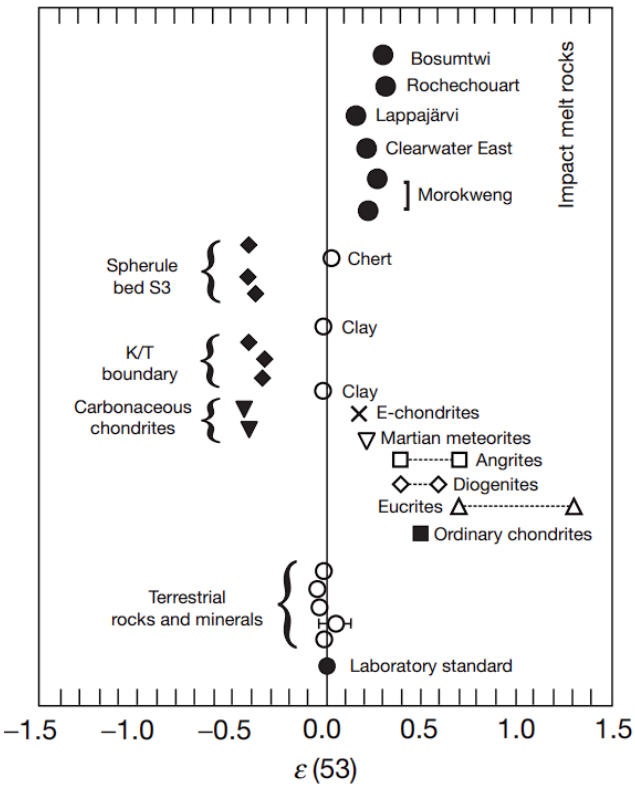

Figure 4. *Chromium isotopic composition of different terrestrial materials, various meteorites, K-Pg boundary sediments, Archean spherule samples from Barberton (South Africa), and melt rocks from several impact structures, from Koeberl (2014). The terrestrial rocks and minerals all plot at about 0.0 ε(53), whereas extraterrestrial material shows a clear positive or negative anomaly in ε(53). The Cr isotopic compositions of the impactites are different from terrestrial material, despite the small amount of meteoritic material incorporated in the melt rocks.*

CHAPTER 2

Geological Setting

2.1. The Boltysh Impact Structure

The Boltysh impact structure is located in the center of Ukraine (48° 45’ N; 32° 10’ E) near its eponymous village Bovtyshka. It is a complex impact structure with a central uplift of 550 m and an outer crater rim diameter of 24 km. The crater was formed in Precambrian basement rocks, mainly consisting of granites and gneisses. The Boltysh impact crater today is buried underneath more than 500 m of post-impact sediments, which have been deposited since the Cretaceous (Grieve et al. 1987).

As noted by Grieve et al. (1987), Boltysh was first described as a collapsed caldera (Bass et al. 1967) before it was recognized as an impact structure by Masaitis (1974). The discovery of shock metamorphism in the form of PDFs in some of the melt rocks of Boltysh was the first evidence, that the structure was impact-generated (Masaitis 1974; Grieve et al. 1987). The Boltysh impact structure gained further interest when age dating pointed to an association with the Cretaceous/Paleogene (K-Pg) boundary and, consequently, the Chicxulub impact event. $^{40}Ar/^{39}Ar$ dating by Renne et al. (2013) revealed an age of 66.04 ± 0.02/0.08 Ma for the K-Pg boundary; additionally, analyses of Sprain et al. (2018) yielded the most precise age yet for Chicxulub, 66.052 ± 0.0008/0.043 Ma. Similar ages have been reported by various authors for the Boltysh impact structure. Kelley and Gurov (2002) dated the impact melt rocks of Boltysh using $^{40}Ar/^{39}Ar$, yielding an impact age of 65.80 ± 0.64/0.68 Ma. Within errors, this value is indistinguishable from the age of the Chicxulub Crater. Two impact events of this size occurring in such a short amount of time is rather unlikely according to the impactor flux rate on Earth (Bland 2005). Recent studies from Pickersgill et al. (2021) show a new, more precise age for the impact melt rocks of the Boltysh impact structure. Their new $^{40}Ar/^{39}Ar$ age of 65.39 ± 0.14/0.16 Ma for Boltysh shows a distinct difference between the ages of the K-Pg boundary and the Boltysh event. According to this study, the Boltysh impact event post-dates the K-Pg boundary by around 0.65 Ma (Pickersgill et al. 2021).

2.1.1. Geology and Petrography of the Boltysh Impact Structure

The impact took place in the Ukrainian shield, which consists of Precambrian granites (Kirovograd porphyroblastic granites) and biotite gneisses in this area, whereas the granites appear to be five times more abundant than the gneisses (Masaitis 1974; Grieve et al. 1987).

As mentioned above, the Boltysh impact structure is a complex structure with a diameter of 24 km and a ~550 m high central uplift, forming a plateau in the center of the crater (Gurov et al. 2003). Around it, the crater forms a shallow depression before rising up again to form the inner rim of the crater (Grieve et al. 1987; Gurov et al. 2003). Both the central uplift and the area underneath the crater comprise blocky brecciated and cataclased autochthonous Precambrian basement, with diaplectic glasses and quartz crystals showing PDFs (Gurov and Gurova 1985; Gurov et al. 2003). The circular depression within the inner crater, which surrounds the central uplift, is characterized by a layer of melt rocks overlaying the fractured crystalline basement (Grieve et al. 1987).

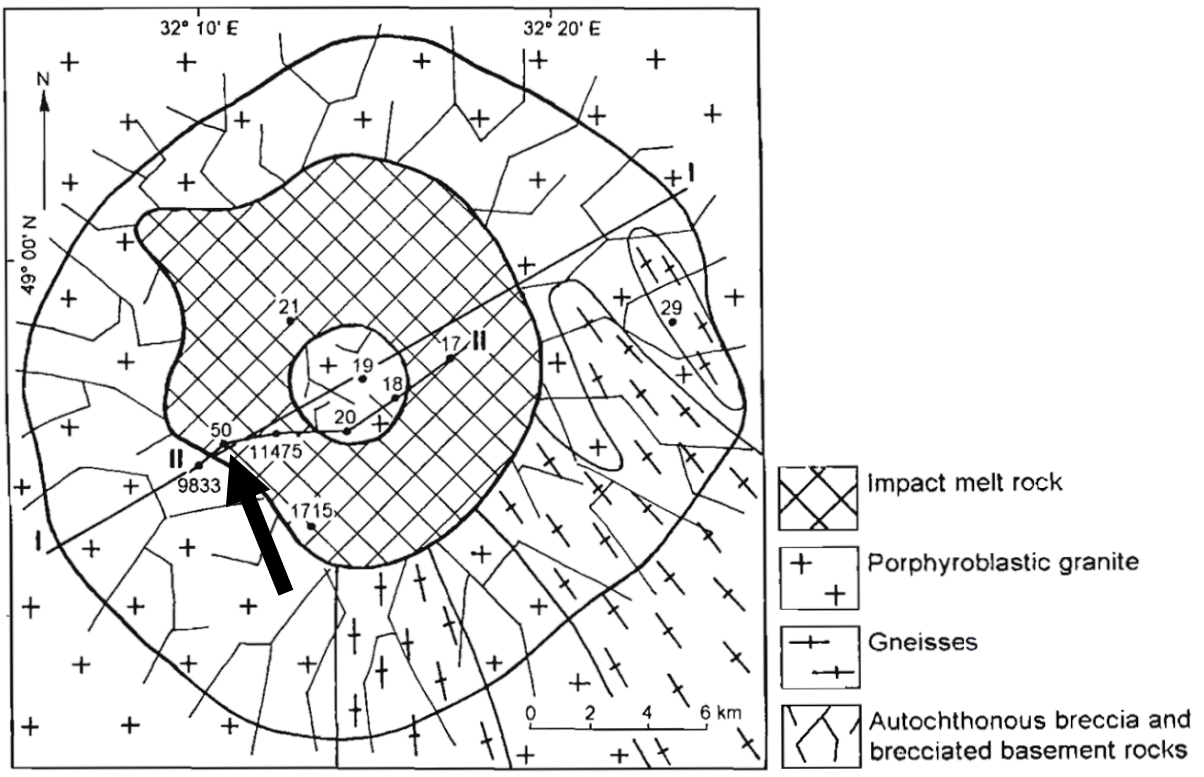

***Figure 5**. Schematic map of the Boltysh impact structure with omitted post-impact sediments (located 48° 45' N; 32° 10' E). The annular impact-melt sheet occupies the inner crater around the central uplift. The location of some drill cores, particularly B50 (see arrow), from which the samples of this study were taken, are indicated (from Gurov et al. 2003).*

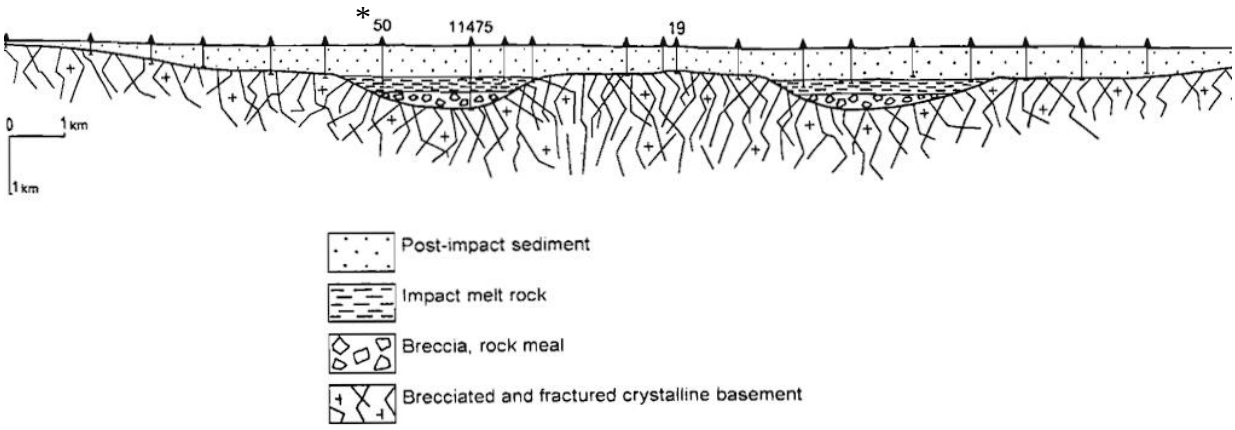

Figure 6. *Schematic cross-section through the Boltysh impact structure, crossing from southwest to northeast, showing the different lithologies of the structure. Several drill cores (B50, B11475, and B19) are marked with vertical lines (from Gurov et al. 2003).* *******Samples studied in this thesis were taken from core B50.*

2.1.1.1. Melt Rocks

The melt rocks in the Boltysh impact structure reach a thickness of up to 220 m (Gurov et al. 2003). According to Grieve et al. (1987), two main types of melt rock can be distinguished, based on their matrix texture in the melt sheet: microcrystalline and glassy melt rocks. The microcrystalline melt rocks appear at the top and the bottom of the melt sheet, confining the glassy matrix melt rocks in between. The glassy melt rocks show a thickness of approximately 130 m in the middle of the melt sheet; however, the depth varies in each borehole. They consist of 20 % feldspar phenocrysts, around 10 % pyroxene phenocrysts, less than 10 % pyroxene microlites, under 5 % monomineralic quartz, and feldspar clasts, as well as granitic clasts. Swallow-tail structures seem to be an uncommon feature in some of the feldspar crystals. Some parts of the glassy melt rocks show partly devitrified glass. On the other hand, the microcrystalline rocks show a higher content of skeletal feldspar phenocrysts (25%) and contain about 5% chlorite. Swallow-tail textures are more common in the feldspars, and some of the quartz clasts show PDFs (Grieve et al. 1987).

2.1.1.2. Suevites

Above the impact melt lies a suevite layer approximately 25 m thick. Suevite is an impact-generated breccia containing glass clasts and fragments of the target rock in a more or less homogeneous matrix. The suevites of the Boltysh impact structure contain glass, monomineralic fragments of quartz and feldspar, and granitic fragments reaching up to 15 mm in diameter (Grieve et al. 1987).

2.1.2. Chemistry and Geochemistry

The melt rocks from the Boltysh impact structure are characterized by their chemical homogeneity; this is a common feature of large impact melt sheets, even if the target rocks are diverse (Grieve et al. 1987). Generally, the Boltysh impact melts show only small deviations in the chemical composition compared to the average basement composition (Grieve et al. 1987). Grieve et al. (1987) analyzed major element and trace element compositions of melt and target rocks from the Boltysh impact structure from two drill cores B50 (580-595 m) and B11475 (793 m) (the major and trace element concentrations are given in the Appendix).

In contrast to the target rocks, the melt rocks show lower levels of K_2O, which might be explained by selective vaporization of alkali elements during the melt formation (Grieve et al. 1987). Additionally, there are small differences in the chemistry between the textural types of melt rocks. They reported a higher Fe_2O_3/FeO ratio and K_2O content in the microcrystalline melt rocks, compared to the fresh glassy and partly devitrified melt rocks (Grieve et al. 1987). The trace element data show that the melt rocks are depleted in Ba and Zn but slightly enriched in Cr and Ni, whereas the other trace elements show no significant difference from the target rocks (Grieve et al. 1987).

The first HSE abundances of Boltysh samples were reported by Schmidt (1997), who measured melt rock samples from borehole B-50 by neutron activation analysis (see Table 1). The melt rocks showed only slightly elevated levels of the HSE, which were barely above the background. The average Ir-content of ~0.2 ± 0.1 ppb (ng/g) (Schmidt 1997) agrees with the previously reported values of <1 ppb (Grieve et al. 1987) and ~0.1 ppb (Gurov et al. 1986). Rhenium, Ir, Rh, and Pd concentrations are elevated in comparison to UCC abundances, while Ru and Au show lower concentrations (Schmidt 1997). The Boltysh melt rocks have Os contents of <0.1 ppb (below the detection limit of the applied method), which are comparable to the UCC and do not show an admixture of meteoritic component. So far, no further measurements of Os concentrations, or Os isotopic compositions, have been made. However, the Rh/Os ratios of the melt rocks (Rh/Os > 15.7) indicate a non-chondritic signature ($Rh/Os_{chondr.}$ = 0.27; Tagle and Berlin 2008), although a loss of Os during the impact cannot be excluded (Schmidt 1997). Given the low HSE contents, the meteoritic signature in the melt rocks from the Boltysh impact structure would correspond to 0.0015-0.07 % nominal CI component; therefore, Schmidt (1997) suggested that the impactor could be of non-chondritic

nature. Nevertheless, the data also could indicate the possibility that no meteoritic material was incorporated into the melt rocks.

Table 1. Instrumental neutron activation analysis measurements of Os, Re, Ir, Ru, Rh, and Pd concentrations of melt rocks from the Boltysh impact structure; modified after Schmidt (1997). Concentrations are given in ppb.

Boltysh	**Os** [ng/g]	**Re** [ng/g]	**Ir** [ng/g]	**Ru** [ng/g]	**Rh** [ng/g]	**Pd** [ng/g]
50/580	<0.1	<0.02	0.07 ± 0.03	<0.2	1.48 ± 0.08	2.10 ± 0.12
50/658.5	<0.1	0.06 ± 0.01	0.25 ± 0.03	0.53 ± 0.1 1	1.49 ± 0.07	2.59 ± 0.12
50/574	<0.1	<0.07	0.26 ± 0.03	0.64 ± 0.07	1.74 ± 0.08	2.00 ± 0.18
50/627.8	<0.1	0.05 ± 0.01	0.07 ± 0.03	<0.2	1.56 ± 0.08	2.41 ± 0.15
50/600.3	<0.1	0.08 ± 0.01	0.24 ± 0.03	0.77 ± 0.08	1.97 ± 0.08	2.18 ± 0.16
50/734	<0.1	<0.01	0.33 ± 0.03	0.83 ± 0.05	1.72 ± 0.08	2.64 ± 0.34
50/696	<0.1	<0.01	0. 15 ± 0.03	<0.3	1 .00 ± 0.07	2.84 ± 0.21
Average		0.06	0.2	0.61	1.57	2.39
Std. Dev (?)		0.02	0.1	0.21	0.3	0.31
CI-Chondrite	495 ± 24.7	40 ± 2	469 ± 23.5	690 ± 34.5	132 ± 6.6	560 ± 22.4
Continental Crust	0.05 **(1)**	0.04-0.48 **(1,2)**	0.03**(2)**	1.1**(3)**	0.38**(3)**	2**(3)**

Ir and Au concentrations were corrected for blank values; 0.19 ng/g for Ir and 0.4 ng/g for Au. All other values are below the detection limit of 0.2 ng/g for Ru, Rh, and Pd, 10 pg/g for Os, and 20 pg/g for Re. The CI-chondrite data were taken from Palme and Beer (1993). Continental crust abundances were taken by various authors: ***(1)*** *Turekian and Luck (1984), Walker et al. (1991), and Esser and Turekian (1993);* ***(2)*** *Schmidt and Pernicka (1994);* ***(3)*** *Schmidt et al. (1997), Schmidt and Palme (1997).*

Further analyses of some siderophile and also chalcophile elements (Cr, Co, Ni, Cu, Au, Ag, Ir, and Pt) of the melt rocks have been reported by Lorenz (1999). These data yield an average Ir content of 0.05 ± 0.04 ppb, whereas one sample (B-11475/762) has a six times higher Ir concentration (~0.31 ppb) than the melt rocks. Furthermore, most melt rocks have elevated concentrations of Cr, Co, and Ni, compared to the basement rocks. Nevertheless, the measurements of the melt rocks were done via ICP-MS and yielded relatively high errors for Ir and Pt measurements; therefore, the data are difficult to interpret (Lorenz 1999).

Finally, McDonald et al. (2009) also reported PGE data of melt rocks and breccias from drill core B-50 (see Figures 5 and 6), which are summarized in Table 2. Three samples (B-734, B-682.2, and B-650) have distinctly higher Ir contents (0.31 ppb, 0.36 ppm, and 0.36 ppb, respectively) than the average UCC (0.022 ppb; Peucker-Ehrenbrink and Jahn 2001) and show also elevated levels of Ru, Rh, and Pt. These are considered good candidates for exhibiting a meteoritic component. The other melt rock samples on the other hand, are only

slightly enriched in PGEs and do not show a distinct admixture of meteoritic material (McDonald et al. 2009).

Table 2. Concentrations of Ir, Ru, Rh, Pt, Pd, and Au of Boltysh melt rock and suevite samples measured by ICP-MS; modified after McDonald et al. (2009). The concentrations are blank corrected and given in ppb.

Sample	Lithology	Ir	Ru	Rh	Pt	Pd	Au
BOL-734	Melt rock	0.31	0.72	0.15	1.70	1.71	0.19
BOL-682.2	Melt rock	0.31	0.77	0.16	2.52	1.60	0.17
BOL-717	Melt rock	0.07	0.22	0.06	0.29	1.36	0.30
BOL-684	Melt rock	0.08	0.23	0.09	0.82	1.22	1.33
BOL-650	Melt rock	0.36	0.80	0.17	1.97	1.25	0.11
BOL-580	Suevite	0.08	0.32	0.06	1.12	3.05	1.35
BOL-603	Melt rock	0.09	0.34	0.07	0.39	1.04	0.23
BOL-627.8	Melt rock	0.10	0.31	0.09	1.31	1.00	0.35
Blank-1		<0.03	0.16	<0.03	0.24	0.21	0.09
Blank-2		<0.03	0.13	<0.02	0.46	0.44	0.28

The samples highlighted in bold were also measured in this thesis.

Chromium isotopic compositions of three samples of impact melt rocks from the Boltysh impact structure were published by Koeberl et al. (2017). They measured $^{53}Cr/^{52}Cr$ ($\varepsilon^{53}Cr$) and $^{54}Cr/^{52}Cr$ ($\varepsilon^{54}Cr$) isotope ratios using thermal ionization mass spectrometry. Two of the samples (B-721 and B-717) showed negative Cr isotopic compositions, which are clearly non-terrestrial, while one of the samples shows a terrestrial composition (see Table 3). The negative $\varepsilon^{53}Cr$ and $\varepsilon^{54}Cr$ values indicate a meteoritic signature characteristic only for volatile-depleted iron meteorites and/or ordinary chondrites. According to these results, a carbonaceous chondrite projectile can be excluded (Koeberl et al. 2017).

Table 3. Chromium isotopic compositions of three Boltysh melt rock samples from core B50, measured with TIMS (n= number of replicates, 2 s.e = 2sd/√n); modified after Koeberl et al. (2017).

	n	$\varepsilon^{53}Cr$	2 s.e	$\varepsilon^{54}Cr$	2 s.e
B-721	5	-0.05	0.04	-0.17	0.07
B-717	7	-0.13	0.02	-0.31	0.06
B-627.8	5	0.03	0.03	0.03	0.04

Samples from the same depths in drill core B50 were also analyzed in this thesis.

2.2. The Italian Sections

Located in the Umbria-Marche basin in Italy, there is a continuous succession of pelagic carbonates, spanning a time period from the early Jurassic to the late Miocene (Sinnesael et al. 2018). This succession is well-known for containing a well-preserved impact record (cf. Montanari and Koeberl 2000), including the Cretaceous/Paleogene boundary, which was first defined by Luterbacher and Premoli Silva (1964) using biostratigraphy in the Bottaccione Section (Italy). With the discovery of an iridium anomaly in some of the end-Cretaceous Umbrian-Marche sections (along with some other sections worldwide), this led to the idea that the mass extinction event, which occurred at the end of the Cretaceous, was caused by an impact event (Alvarez et al. 1980). Today it is widely accepted that the Chicxulub impact event caused, or at least was the main cause, of the mass extinction at the K-Pg (see Schulte et al. 2010).

The Scaglia Rossa Formation, spanning in age from the early Turonian to the late Ypresian, is one of the main units in the Umbrian-Marche section (cf. Montanari and Koeberl 2000; Sinnesael et al. 2016). Its pelagic carbonates are characterized by red biomicritic limestone, which consists of mainly foraminiferal shells embedded in a coccolith matrix and terrigenous silt and clay (Arthur and Fischer 1977; Johnsson and Reynolds 1986; Sinnesael et al. 2016). Some of the shale beds are interbedded in these limestones (Arthur and Fischer 1977). At the lower member R1 (Turonian to Santonian) and upper part R4 (upper Ypresian) of this formation, radiolarian chert layers are present. The R2 member (Campanian to Maastrichtian) consists mainly of the typical pink limestones with the exception of a short marly interval at the lower part. In the Danian to Thanetian (R3), several marly horizons in between the limestone beds can be found.

2.2.1. Bottaccione, Contessa Highway, and Morello

The Scaglia Rossa unit can be found in many sections and outcrops in the Umbrian-Marche basin (cf. Montanari and Koeberl 2000). In this study, the focus is on three outcrops: the Bottaccione section (BOT), the Contessa Highway section (COH), and the Morello Section (MRL) (Sinnesael et al. 2018, 2019). The sections of Bottaccione and Contessa Highway are located near Gubbio, while the Morello section is situated about 25 km northeast (see Figure 7) (Sinnesael et al. 2019). According to paleogeographic reconstruction, the three sections have been deposited in a deep marine basin, more than several hundred kilometers away from continental landmasses (Sinnesael et al. 2016). All three of these sections contain the K-Pg

boundary, possibly some evidence of exhalations from the Deccan Traps' large volcanic eruptions in India, the aftermath and recovery of the mass extinction, as well as hypothermal events and thermal maxima throughout the Paleocene and Eocene (Sinnesael et al. 2016).

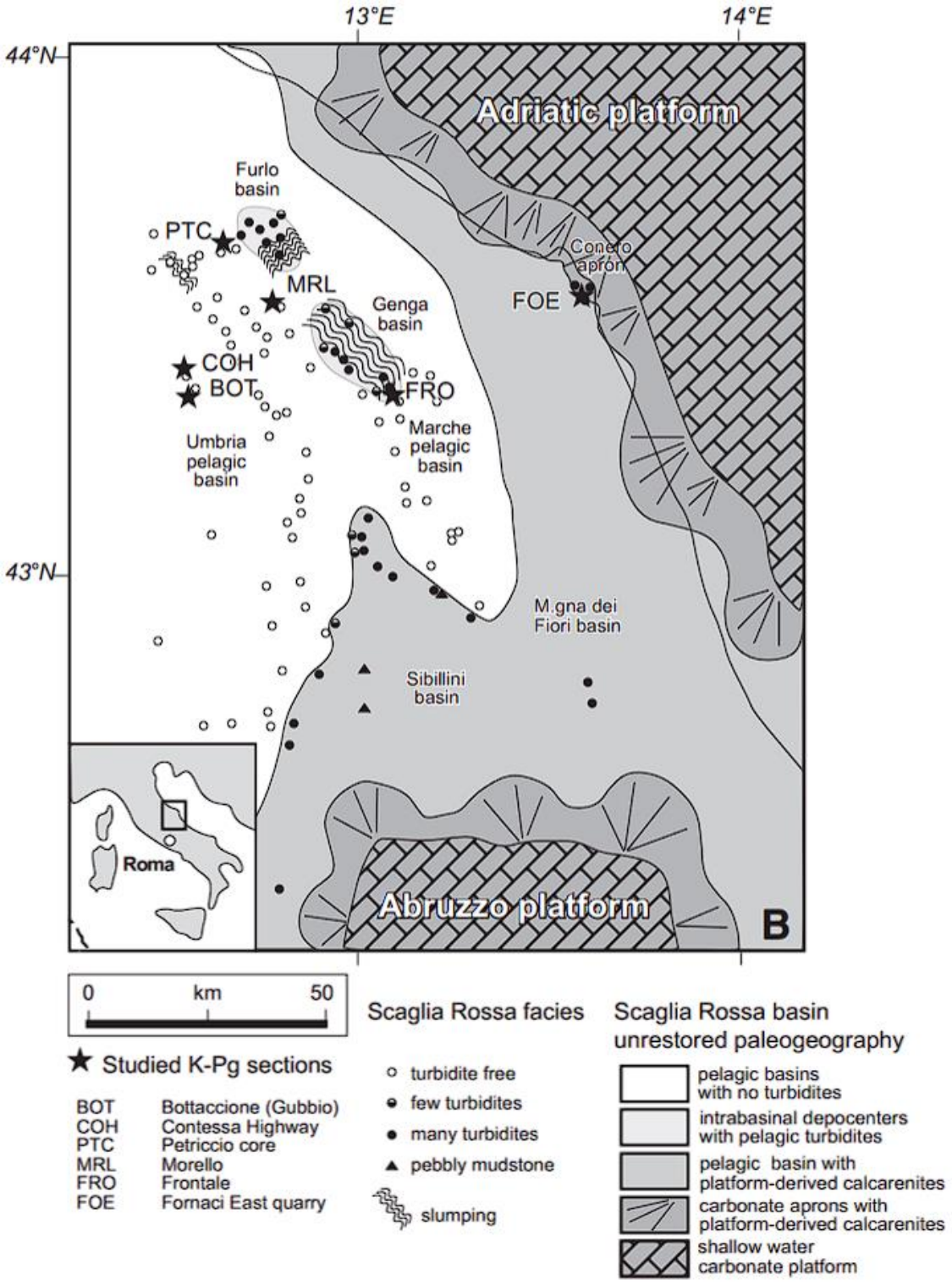

Figure 7. *Simplified paleogeographic map of the late Cretaceous Umbria-Marche basin with the location of various stratigraphic sections, from Sinnesael et al. (2019). The locations studied in this thesis are BOT - Bottaccione section (43°21'58.0"N, 12°34'57.5"E), COH - Contessa Highway section (43°21'46.9"N, 12°33'44.1"E), and MRL - Morello Section (43°29'50.5"N, 12°48'38.2"E).*

2.2.2. ALE Ash

Within the limestones of the Scaglia Rossa, a thin red biotite-rich ash layer, called “ALE ash” (short for “Livello Alessandro”, an informal designation), is present (Sinnesael et al. 2016). The ALE ash occurs about two meters above the K-Pg boundary, depending on the outcrop (+2.45 m in MRL, +1.9 m in BOT, and +2.0 m in COH) (Sinnesael et al. 2019). Twenty million years before and after the K-Pg boundary, nothing similar to the ALE ash layer appears in the Scaglia Rossa succession; therefore, the ALE ash seems to indicate an unusual event in the Scaglia Rossa deposit. The origin of this layer is not yet fully understood, and a volcanic origin was suggested by Sinnesael et al. (2019). In the Contessa Highway section, the ALE layer shows a significant local drop of Ca in the section, as well as a peak in the Fe and Mn concentrations (Sinnesael et al. 2019).

$^{40}Ar/^{39}Ar$ age dating of the ALE-biotite grains yielded a mean age of 64.8 ± 1.6 Ma, a result, indistinguishable from the age of the K-Pg boundary (66.04 ± 0.02/0.08 Ma, Renne et al. 2013, Sprain et al. 2018). Interestingly, Sinnesael et al. (2016) determined an astronomical age of 65.440 ± 0.005 Ma for the ALE ash layer, which is, within analytical uncertainty, consistent with the recent age determination for the Boltysh impact event of 65.39 ± 0.14/0.16 Ma (Pickersgill et al. 2021).

Due to the recently published age of the Boltysh crater (65.39 ± 0.14/0.16 Ma, Pickersgill et al. 2021), which indicates a similar age (within analytical error) of the Boltysh impact event and the ALE ash layer (65.440 ± 0.005 Ma; Sinnesael et al. 2016), the possibility that these two events could be correlated can be investigated. This age consistency makes a search for a meteoritic component within the ALE ash layer a promising attempt to correlate the Boltysh impact event with the ALE ash. Aside from the overlap in age, the stratigraphic position of the ALE ash in the Scaglia Rossa formation, 1.9-2.45 m above the K-Pg boundary, is fitting, considering the Boltysh impact happened ~0.65 Ma after the K-Pg. Up until now, no search for a meteoritic signature has been attempted in the ALE ash layer. In fact, in contrast to the K-Pg boundary, only a few studies have been done on the ALE ash so far. This thesis attempts to search for a possible meteoritic signature in the ALE ash samples of Morello, Bottaccione, and Contessa Highway, specifically by determining its Re-Os isotopic composition and HSE concentrations.

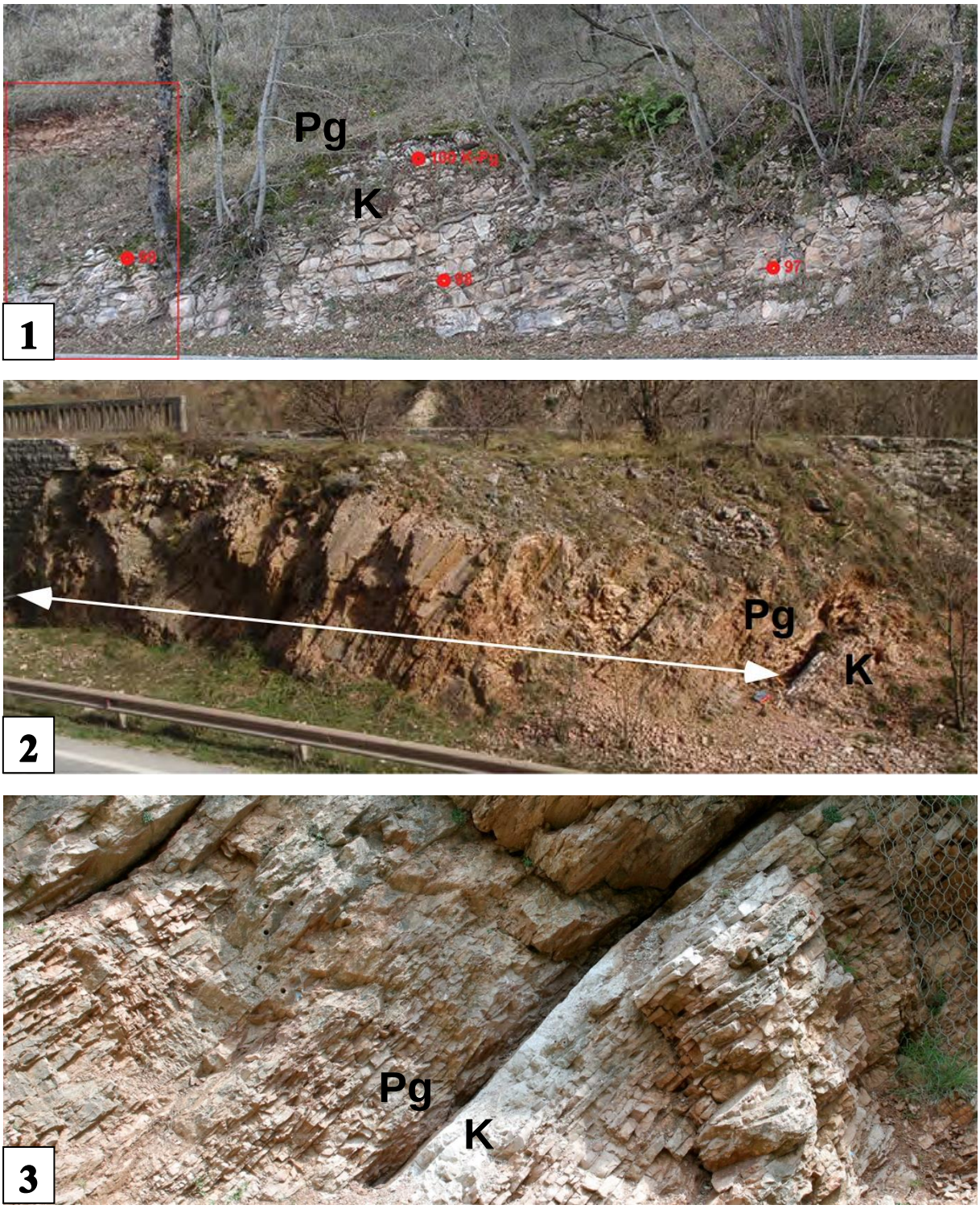

Figure 8. *Photos of the (**1**) Morello, (**2**) Contessa Highway, and (**3**) Bottaccione section, taken from Sinnesael et al. (2016, 2019). The K-Pg boundary is present in all three sections, a few meters above, the ALE ash layer appears. The red rectangle in (**1**) represents the location of the ALE ash and is magnified in Chapter **3.1.1**.*

CHAPTER 3

Samples and Methods

3.1. Samples

3.1.1. Samples of Morello, Bottaccione, and Contessa Highway

The samples were taken from the pelagic sediments (red biomicritic limestone and marl) and the ALE ash layer of the Scaglia Rossa formation, which is exposed in the Morello, Bottaccione, and Contessa Highway sections. The ALE Ash occurs at different heights above the K-Pg boundary in each outcrop, above 2.45 m in Morello (MRL 21-2.45, MRL 22-2.45), 1.90 m in Bottaccione (BOT 22-101.90), and 2.00 m in Contessa Highway (COH-22-102.00). Five samples each from the Contessa Highway and Bottaccione section and ten samples from the Morello section were taken by Alessandro Montanari, partly together with C. Koeberl. The Morello outcrop was sampled twice, each time five samples were obtained from the same stratigraphic layers but approximately one meter apart (see Figure 8). In each section, the ALE ash layer, together with the carbonate layers directly above and underneath the ALE ash was targeted. From each section a total of 10 cm, in 1-5 cm intervals, was sampled, with details shown in Figure 10. A list of all samples is given in Table 4, where the sample name was chosen after the year (e.g., 22 for the year 2022) and the position in the outcrop (in meters), with the K-Pg boundary at 100 m (for the COH and BOT samples), or 0 m (for the MRL samples). The samples were taken to determine the contents of the trace element concentrations, including HSE contents, and Os isotopic compositions.

Table 4. Sample list of the Italian sections Morello (MRL), Bottaccione (BOT), and Contessa Highway (COH). The samples were obtained in 2021 and 2022 by A. Montanari and C. Koeberl.

MRL21	MRL22	BOT	COH
21-2.40	22-2.40	22-101.95	22-101.85
21-2.45	**22-2.45**	**22-102.00**	**22-101.90**
21-2.46	22-2.46	22-102.01	22-101.91
21-2.48	22-2.48	22-102.03	22-101.93
21-2.50	22-2.50	22-102.05	22-101.95

The outlined samples represent the appearance of the ALE ash layer in each section.

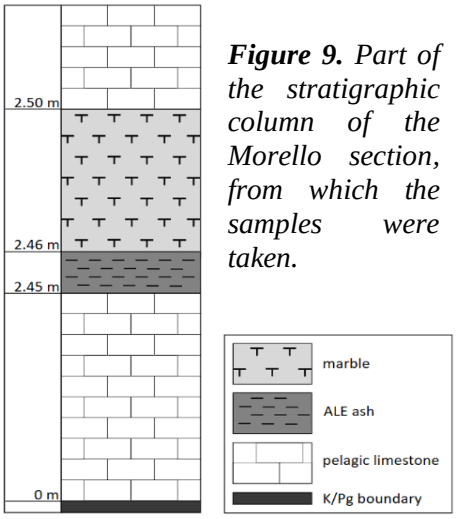

Figure 9. *Part of the stratigraphic column of the Morello section, from which the samples were taken.*

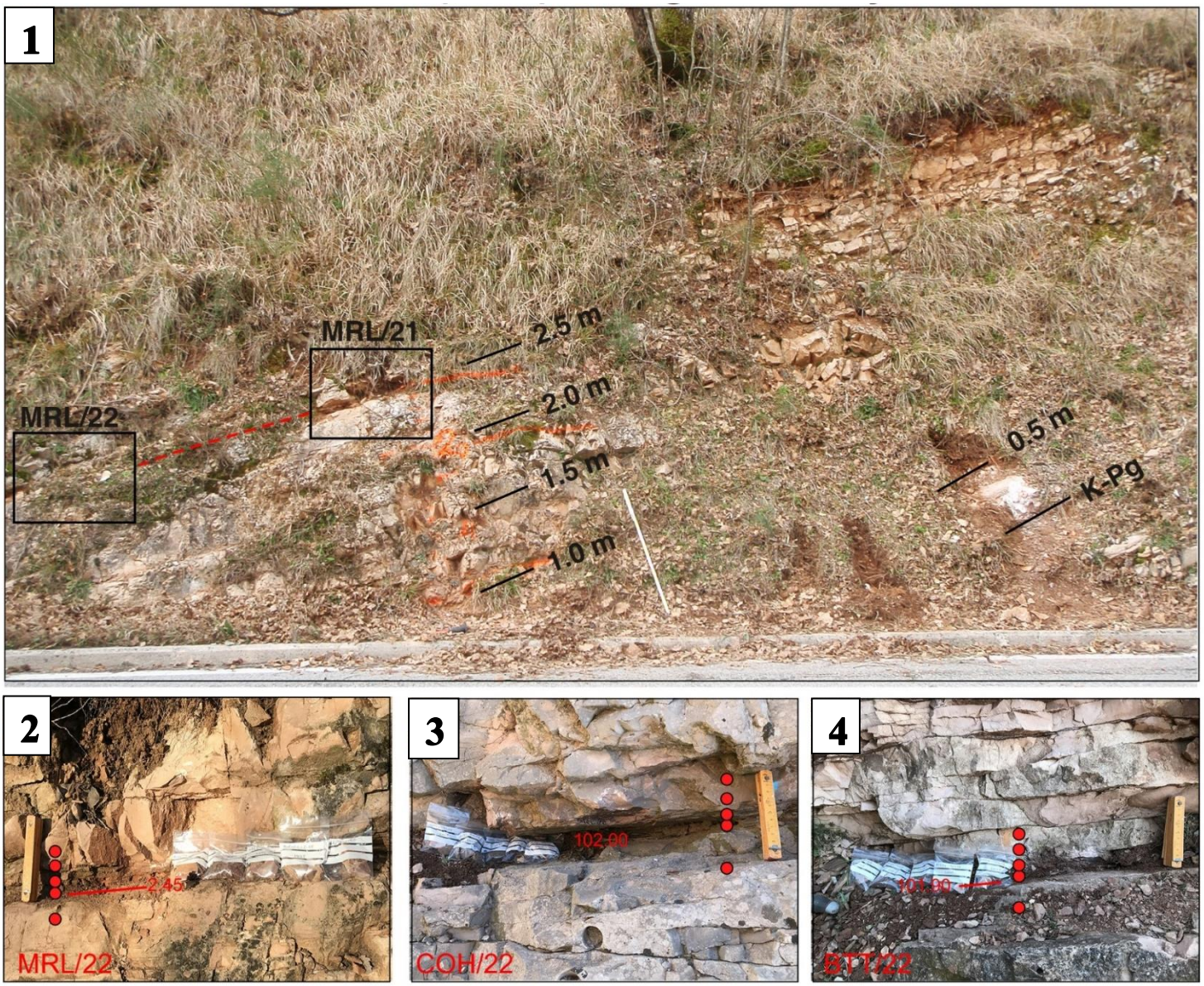

Figure 10. *Location of the ALE ash in the Morello section (**1**), 2.45 m above the K-Pg boundary. Samples were taken of two different places, once in 2021 and once in 2022. Underneath, close-up images of the ALE ash in the Morello (**2**), Contessa Highway (**3**), and Bottaccione (**4**) sections are displayed. The red dots represent the location where the samples were taken. Figure courtesy of Alessandro Montanari.*

3.1.2. Samples of the Boltysh Impact Melt Rocks and Suevites

To gain further insight into the geochemistry of the Boltysh impactites, four impact rocks and two suevites of the Boltysh impact structure were analyzed. The melt rocks and suevites were taken from different depths in drill core B50, whereas the depth of each sample is given in the sample name. The samples of the Boltysh impactites were provided by the University of Vienna. For this study the already prepared same bulk powder, that was used for INAA measurements of Boltysh impactites by C. Koeberl and D. Mader, was used.

The Cr isotopic compositions of three of the chosen melt rocks have already been analyzed by Koeberl et al. (2017) and are also given in Table 5. The samples selected for this study were analyzed by C. Koeberl and D. Mader for their geochemistry via INAA (unpublished data from C. Koeberl and D. Mader (2009)). These data will be presented and discussed in this study together with newly obtained HSE and Re-Os isotopic data via ICP-MS (inductively coupled mass spectrometry) and TIMS (thermal ionization mass spectrometry).

Table 5. Sample list of melt rocks and suevites of the Boltysh impact structure together with Cr isotopic compositions from Koeberl et al. (2017).

Sample No.	**Lithology**	**ε^{53}Cr**	2 s.e	**ε^{54}Cr**	2 s.e
B-50/576.5	Suevite with porous glass inclusions	-	-	-	-
B-50/588	Suevite with dark grey glasses	-	-	-	-
B-50/627.8	Crystalline impact melt rock	0.03	0.03	0.06	0.07
B-50/710	Impact melt rock with fresh glass	-	-	-	-
B-50/717	Impact melt rock with glassy matrix and rare quartz inclusions	-0.13	0.02	-0.31	0.06
B-50/721	Impact melt rock with intensively devitrified glassy matrix	-0.05	0.04	-0.17	0.07

3.2 Methods

3.2.1. Instrumental Neutron Activation Analysis (INAA)

Instrumental neutron activation analysis is an analytical, non-destructive technique used to determine qualitative and quantitative element contents in materials. While it can only detect some major elements (Na, K, Fe), it can detect numerous minor and trace element concentrations comprising Sc, Cr, Co, Ni, Zn, As, Se, Br, Rb, Sr, Zr, Sb, Cs, Ba, Hf, Ta, W, Ir, Au, Th, and U; also the rare-earth elements La, Ce, Nd, Sm, Eu, Gd, Tb, Tm, Yb, and Lu can be measured. Instrumental neutron activation analysis can detect abundances down to 10^{-6} -10^{-9} g (ppm-ppb) and less, depending on the element (e.g., Bode et al. 2009; Mader and Koeberl 2009).

3.2.1.1. Sample Preparation

The samples were first crushed and then placed into an agate mill for several minutes. Instrumental neutron activation analysis does not necessarily require pulverized samples, but using them ensures that a representative and homogeneous part of the sample is measured. About 120 mg of each sample was taken, precisely weighed, and transferred into small polyethylene capsules. After the capsules are sealed airtight, the samples are ready for irradiation. Three high-purity synthetic multi-element standards were used for calibration: the carbonaceous chondrite Allende standard (Smithsonian Institution, Washington DC, USA; Jarosewich et al. 1987), the Ailsa Craig granite AC-E standard (Centre de Recherche Petrographique et Geochimique, Nancy, France; Govindaraju 1989), and the Devonian Ohio shale SDO-1 standard (United States Geological Survey; Govindaraju 1989) (Mader and Koeberl 2009).

3.2.1.2. INAA Principle

The principle of this method is to irradiate the samples with neutrons in a nuclear reactor under specific conditions. In this study, the 250 kW Triga Mark II reactor from the Atomic Institute of the Technical University Vienna was used. Fifteen samples, together with the three standards, were irradiated for 6-8 h with a thermal neutron flux of 1.7×10^{12} n cm^{-2} s^{-1}. The atoms are bombarded with thermal neutrons (neutrons that are in thermal equilibrium with the atoms of the moderator, with energies around 0.025 eV), causing the atomic nucleus to capture the neutrons (mostly single neutron capture reactions under these conditions) (e.g., Greenberg et al. 2011). Shortly after the neutron is absorbed, the nucleus emits prompt γ-rays,

which can be measured with a different kind of neutron activation analysis (prompt y-ray NAA) (e.g., Stosch 2016)). After the capture of an additional neutron, the resulting atomic nucleus becomes unstable (radioactive isotope) and tries to reach its stable state via radioactive decay (mostly β-decay) (e.g., Greenberg et al. 2011). During the decay, the nucleus emits γ-rays, called delayed γ-rays, which are characteristic of each isotope. The distinct γ-rays can be measured, whereas the intensity of the γ-radiation is proportional to the concentration of each element in the sample (e.g., Greenberg et al. 2011).

3.2.1.3. Detection

A semiconductor detector (in this study a high-purity germanium (HpGe) detector) was used to detect the different energies by the emitted γ-rays. The samples and the detector are shielded from the environment via lead walls, to minimize additional γ-rays from the surroundings. If γ-rays reach the semiconductor, electrons from the valence band are elevated into the conduction band, leaving holes in the valence band (e.g., Greenberg et al. 2011). Applying a high-voltage electric field forces the free charge carriers to move to the electrodes, which results in an electric signal, that is proportional to the energy of the emitted γ-rays (e.g., Greenberg et al. 2011). This signal is then amplified (first in a preamplifier and then in a main amplifier), processed by a digital signal processor (Canberra DSP Model 2060), and stored in a multichannel analyzer. There they are combined into a γ-spectrum (c.f. Koeberl 1993; Mader and Koeberl 2009).

Not every element has appropriate decays, so the method is limited to certain elements, including the elements listed above. Each element that forms radioactive isotopes has a unique half-live, therefore the samples have to be measured in different counting cycles (Mader and Koeberl 2009). The short-lived radioactive isotopes, which have half-lives around 0,5-3 days (^{24}Na, ^{42}K, ^{76}As, ^{82}Br, ^{122}Sb, ^{140}La, ^{153}Sm, ^{169}Yb, ^{175}Yb, ^{177}Lu, ^{187}W, ^{198}Au, ^{239}Np), are measured in a first cycle (for 30-60 min approximately five days after the radiation). Elements with a longer half-life (^{46}Sc, ^{51}Cr, ^{59}Fe, ^{58}Co (Ni), ^{86}Rb, ^{85}Sr, ^{95}Zr, ^{131}Ba, ^{140}La, ^{141}Ce, ^{147}Nd, ^{153}Sm, ^{152}Eu, ^{160}Tb, ^{170}Tm, ^{169}Yb, ^{175}Yb, ^{177}Lu, ^{181}Hf, ^{182}Ta, ^{233}Pa (Th)) are typically measured 2-8 days after the first measurement cycle (for 2-4 hours per sample). After five weeks, the majority of the short-lived isotopes have already decayed and the elements with the longest half-lives (^{46}Sc, ^{51}Cr, ^{59}Fe, ^{58}Co (Ni), ^{60}Co, ^{65}Zn, ^{75}Se, ^{86}Rb, ^{85}Sr, ^{95}Zr, ^{134}Cs, ^{131}Ba, ^{141}Ce, ^{152}Eu, ^{153}Gd, ^{160}Tb, ^{170}Tm, ^{181}Hf, ^{182}Ta, ^{192}Ir, ^{233}Pa (Th)) can be measured for typically 24 h per sample (Mader and Koeberl 2009).

3.2.1.4. Corrections

The neutron flux itself may not be homogeneous at all places in the reactor. Therefore, a flux monitor is needed, for example, an Au-doped aluminum wire, or -as this study- the Na content of the standards can be used (e.g., Koeberl 1993). Sodium (Na) is present in all three standards, which are deliberately placed among the samples, so the neutron flux can be calculated at different places. Because the samples are all measured individually and at different times, a decay correction and a normative time correction are done by a software (Genie2000). Each detector has a certain dead time, which is the time a detector cannot process any further impulses after it received a signal. If two pulses reach the detector in a short time span, shorter than the dead time of the detector, then the second pulse would be unperceived (e.g., Greenberg et al. 2011). Therefore, a dead-time correction is needed, which is also done by the software. To quantify the output, a standard analysis needs to be done. Every sample is calculated against the standards, yielding the content of each element in ppm, ppb, or wt% (e.g., Koeberl 1993).

3.2.2. Highly Siderophile Element and Re-Os Isotope Analysis

3.2.2.1. Wet Chemistry

For the HSE and Re-Os isotopic analyses, wet chemical dissolution of the samples and separation of the elements are required. The sample material was crushed into smaller pieces with a jaw crusher before it was put into an agate disc mill for a few minutes, to achieve a finer grain size and homogeneity. About 100-400 mg of each sample powder were weighed into quartz vials and a tracer solution (spike), containing ^{99}Ru-^{105}Pd-^{185}Re-^{190}Os-^{191}Ir-^{194}Pt, was added for isotope dilution generated HSE concentration determinations. After adding ~2 ml of hydrochloric acid (HCl) (to drive off CO_2 from the carbonate samples) and ~3 ml of nitric acid (HNO_3), all quartz vials were sealed using Teflon foil and put into an Anton-Paar high-pressure Asher (HPA-S) for about three hours at 100-130 bars and 270 °C. During this process, the spike equilibrates with the sample and the elements of interest (HSEs) are leached from the undissolved sediment into the acid (e.g., Cohen and Waters 1996).

Directly after the HPA treatment chloroform ($CHCl_3$) was sequentially added to the acid and the mixture was equilibrated on a sample mixer for a few minutes. This causes the osmium to partition into the chloroform, while the other HSE stay in the aqua regia. The chloroform, now containing Os, was separated from the aqua regia using pipettes and mixed with 4 ml of hydrobromic acid (HBr) in a Teflon© beaker. After this solvent extraction procedure (see Cohen and Waters 1996) Os partitions from the chloroform into the HBr on a sample mixer overnight. The HBr was then back-extracted from the chloroform using micropipettes and evaporated at 60 °C on a hot plate for 24 hours. Finally, Os was further purified using conventional microdistillation techniques (see Birck et al. 1997), using sulfuric acid (H_2SO_4) and Cr(VI) as oxidant.

The aqua regia, containing the remaining HSEs (except Os), as well as the undissolved sample sediment, was dried down and treated with hydrofluoric acid (HF) to fully extract Re from the silicate minerals. After further sample treatment using concentrated HNO_3 and HCl the sample was redissolved in 1M HCL and Re, Ru, Ir, and Pt were separated from Pd using a two-step exchange chromatography, as described by Pearson and Woodland (2000) (summarized in the appendix).

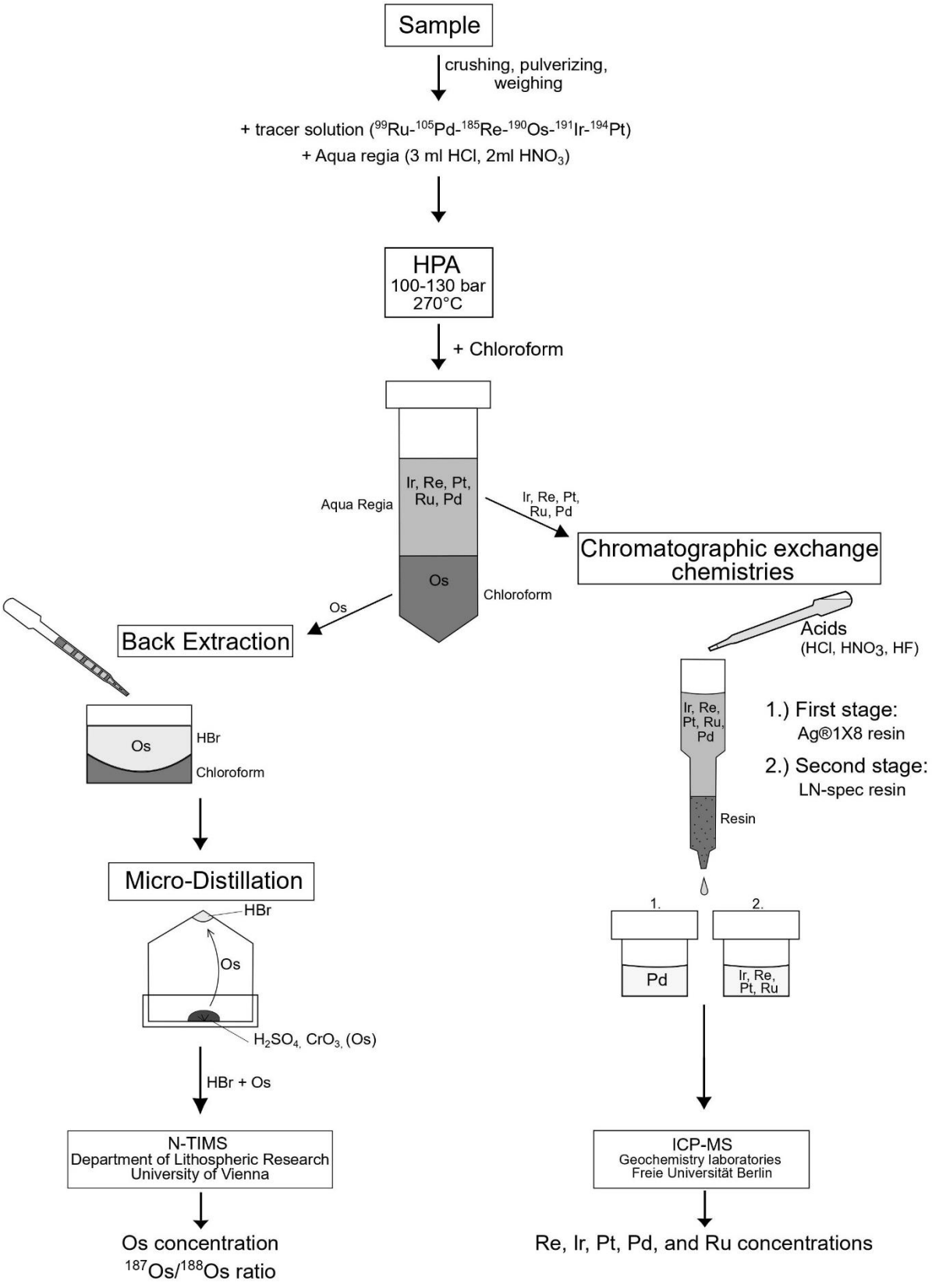

Figure 11. *Schematic diagram of the major steps of chemical preparation for isotope dilution mass spectrometry. Recipes for the chromatographic exchange chemistries are given in the Appendix.*

3.2.2.2. Mass Spectrometry

Mass spectrometry is a method for measuring isotopic ratios of elements in, for example, any geological samples. Depending on the element(s) of interest and the aggregate state of the sample to be analyzed (solid-, liquid-, or gaseous state), different kinds of mass spectrometers can be used (e.g., Makishima 2016). The principle of a mass spectrometer is the same for all types. It comprises four main units: the vacuum equipment, the ion source, the mass separator, and the detector (e.g., Makishima 2016). The ion source is responsible for the ionization of the molecules or atoms of the sample. This can happen in different ways, depending on the type of mass spectrometer. There are a number of different mass spectrometers used in the geosciences, which are named either by their technique of ionization (e.g., thermal ionization mass spectrometry, TIMS, or inductively coupled plasma mass spectrometry, ICP-MS) or by the technique applied for mass separation (e.g., time of flight-, quadrupole-, or magnetic sector mass spectrometry, where the latter term can include both, TIMS and ICP-MS). Only the two types of mass spectrometry applied in this study are explained here in more detail. These techniques comprise thermal ionization mass spectrometry (TIMS) and inductively coupled plasma mass spectrometry (ICP-MS).

In the case of TIMS, the sample is loaded onto a metal filament, which is then heated to a certain temperature (usually ranging from ~600 to ~2500 °C, depending on the element to be ionized and the filament material used) by applying an electric current. This causes the molecules to evaporate and ionize (e.g., Makishima 2016). In addition to the usually produced positively charged ions, it is necessary for some elements with a high ionization potential to produce negatively charged molecule-ions (such as OsO_3^- in case of Os) in order to be able to measure these elements using TIMS (see Chapter 3.2.2.2.1. for more details). In contrast, in ICP-MS the sample is introduced as a solution into a plasma flame, leading to instantaneous dissolution and breakdown of molecules into individual atoms and their ionization irrespective of their different ionization potentials (cf. Vanhaecke and Degryse 2012).

After acceleration of the ions, they are, in case of TIMS, introduced into a magnetic sector field which deflects the ions based on their mass-to-charge ratio (m/z) (e.g., Vanhaecke and Degryse 2012; Makishima 2016). The higher the charge and the lighter the mass, the more strongly the ions get deflected from their original path, and therefore, different masses are spatially divided (i.e., fractionated). Another way to separate the molecules/atoms (used in this study for ICP-MS analysis) is via a quadrupole mass filter. It comprises four symmetric electric poles that can only be passed by ions with a certain m/z of choice (e.g., Makishima

2016). Subsequently, the ions reach the detector in both TIMS and ICP-MS, where the ion beam for specific isotopes are converted into measurable electric signals, whose ratios can be used to calculate the isotopic composition of the element (e.g., Vanhaecke and Degryse 2012). There are various kinds of ion detectors with different sensitivities, ranging from Faraday Cups (equipped with different resistors) to secondary electron multipliers (SEM) (e.g., Makishima 2016). Whereas the former is commonly used to simultaneously measure different isotopes of an element at the same time (multi-collector mode measurements). The SEM-technique applied in this study for Os measurements (see Chapter 3.2.2.2.1.) is performed in static mode, where the isotopes are measured sequentially within the same electron multiplier (peak-hopping mode), leading to the disadvantage of a lower precision (compared to multi-collector measurements), but allowing higher sensibility compared to conventional Faraday Cups.

In this study, thermal ionization mass spectrometry (TIMS) was used to determine isotope compositions of Os and the concentration of Os via the isotope dilution technique. Contrary, isotope dilution generated Re, Ir, Pt, Ru, and Pd concentrations were obtained using inductively coupled plasma mass spectrometry (ICP-MS).

3.2.2.2.1. Osmium Mass Spectrometric Analyses

The Os concentrations and isotope composition were measured using a Finnigan TRITON-TIMS at the Department of Lithospheric Research at the University of Vienna (Austria). The sample-osmium was loaded as 1 µl of an Os-bromide solution onto single platinum filaments that were then slightly heated with a 600 µA current to evaporate the excess HBr (see also Völkening et al. 1991). The dried sample-Os was then covered with 1 µl of $NaOH/Ba(OH)_2$ activator and dried (e.g., Luguet et al. 2008). Osmium was measured in negative mode in the form of osmium oxides (OsO_3^-, OsO_4^{2-}) in a peak hopping sequence (static mode) using a SEM detector. Isobaric interferences, caused by W- or Pt-oxides, were not observed. The $^{187}Re^{16}O_3^-$ (m=235) mass interference on $^{187}Os^{16}O_3^-$ (m=235) was corrected by measuring the $^{185}Re^{16}O_3^-$ (m=233) molecule as reference. The ^{187}Re interference was calculated with the isotope ratio $^{185}Re/^{187}Re$= 0.59744, using the Re isotope abundances from Kondev et al. (2021). After oxygen correction, mass fractionation of the Os isotopes was corrected using $^{192}Os/^{188}Os$ = 3.083 (e.g., Luguet et al. 2008). The average Os total procedural blank was 0.7 ± 0.4 pg, contributing up to 60% to the total Os concentration in some of the most Os-depleted samples. All sample data were blank-corrected.

A standard reference material (OKUM komatiite, IAG-certified ultrabasic rock reference material; Meisel et al. 2001, 2013; Meisel and Moser 2004) was dissolved and measured along with the samples to test fractionation during wet chemical sample treatment, leading to Os isotope ratios identical to literature values (e.g., Meisel et al. 2001, 2013; Schulz et al. 2016) within analytical uncertainty (see Appendix for details). Daily machine performance was further tested by measuring the 10 pg of DROsS (Durham Romil Osmium Standard) solution, yielding literature values in all cases. The DROsS measurements were performed using the electron multiplier at signal intensities, that were typically achieved during the sample measurements (10,000-100,000 counts on $^{192}Os^{16}O_3$, m=240).

3.2.2.2.2. HSE Mass Spectrometric Analyses

The HSE samples (without Os) were measured using the isotope dilution technique by adding a mixed ^{99}Ru-^{105}Pd-^{185}Re-^{190}Os-^{191}Ir-^{194}Pt tracer solution (spike). The isotope dilution method is a technique for high-accuracy measurements of isotopes using a tracer solution, of which the quantity of spike isotopes is precisely known. It is added directly to the sample and equilibrated before further isolation processes. By adding the tracer solution, the isotopic composition of the element(s) of interest changes, which is then measured via mass spectrometry. The original isotopic composition can then be calculated by subtracting the known isotopic composition of the tracer solution (e.g., Mark 1954; Heumann 1992; Alonso and Rodríguez-González 2013).

Measurements were performed using a Thermo Element XR ICP mass spectrometer in single collector mode at the geochemistry laboratories at Freie Universität Berlin (Germany). HSE sample solutions were introduced using an Aridus I desolvation system and signals were detected in low-resolution mode with an SEM. Oxide formation fractions (CeO/Ce) typically ranged between 0.25 and 0.5 %. Cadmium, Hg, and Os isotopes were analyzed to monitor isobaric interferences, which were then corrected if necessary. Isobaric interferences were negligible. The internal precision of measured isotope ratios ranges from 0.1% to 1% (2σ). Instrumental mass discrimination was determined and corrected by comparison of isotope ratios with standard solutions measured in the same sequence. Isotopic ratios of ^{99}Ru/^{101}Ru, ^{105}Pd/^{108}Pd, ^{185}Re/^{187}Re, ^{191}Ir/^{193}Ir, and ^{194}Pt/^{195}Pt were used for isotope dilution calculations. Analytical blanks determined during the course of this study were on average (1 SD): 14 ± 2 pg Re, 0.9 ± 0.2 pg Ir, 3 ± 0.7 pg Ru, 70 ± 16 pg Pt, and 51 ± 22 pg Pd (n=3). All concentrations were corrected for average blank contributions, which generally accounted for <0.5 % for all samples.

Measurements of the OKUM standard reference material (komatiite, IAG-certified ultrabasic rock reference material; Meisel and Moser 2004; Meisel et al. 2001, 2013) were repeatedly performed to monitor the analytical quality of the measurements. All concentrations for OKUM yielded values within the ranges reported in the literature (see Appendix).

CHAPTER 4

Results

4.1. Boltysh Samples

4.1.1. Major, Minor-, and Trace Elements

In this study, no complete major element analysis of the four Boltysh impact melt rocks and two suevites was conducted, but the INAA measurements yielded concentrations of 2.0-2.9 wt% Na, 3.0-4.7 wt% K, and 2.0-3.6 wt% for Fe, within the range of concentrations obtained by earlier studies on impactites from the Boltysh impact structure (Grieve et al. 1987; Hölker and Deutsch 1996; Kashkarov et al. 1998).

Trace element data of the six samples from Boltysh impact melt rocks and suevites are also within the range obtained by earlier studies (Grieve et al. 1987; Hölker and Deutsch 1996; Lorenz et al. 1999), as reported in Table 6. Generally, the samples are relatively homogeneous relating to trace element concentrations and there are no major deviations among the samples. Average concentrations in the impactites are 6.5 ppm Sc, 53.7 ppm Cr, 7.5 ppm Co, 34 ppm Ni, 0.5 ppm Br, 173 ppm Rb, 166 ppm Sr, and 270 ppm Zr. The occurrence of some elements tends to vary between samples, such as that of Zn (52-163 ppm), Cs (0.4-2.2 ppm), and Ba (398-543 ppm). Concentrations of As, Se, Sb, Ir, and Au were below the detection limit. Cobalt and Ni are homogeneously distributed between samples, whereas the concentration of W is higher in B-50/576.5 (~4 ppm).

Chondrite-normalized rare-earth element patterns of the Boltysh samples are plotted in Figure 12. All samples show uniform steeply negative REE patterns and enrichments of LREE. In addition, they have a negative Eu anomaly and a positive Gd peak. The Gd anomaly is more pronounced in B-50/710 and B-50/627.8, and these samples also show a slight depletion in Yb and Lu. The suevites seem to have a minor enrichment of the REEs compared to the melt rocks. No REE analyses of Boltysh target rocks have been conducted so far, therefore, basement rocks from the Ilynets crater were used as a reference for comparison in Figure 12 (data from Gurov et al. 1998). The Ilynets basement, as part of the Ukrainian shield, also comprises mostly granites (Gurov et al. 1998) and is expected to closely resemble the Boltysh

target rocks. As demonstrated in Figure 12, the Ilynets basement rocks show chondrite-normalized REE patterns almost identical to those of the Boltysh melt rocks.

Table 6. Major, minor, and trace element data of Boltysh impact melt rocks and suevites measured by INAA. Analytical results are given in ppm (except as noted). (Unpublished data by C. Koeberl and D. Mader 2009).

(ppm)	(suevite) B-50/576.5	(suevite) B-50/588	(melt rock) B-50/627.8	(melt rock) B-50/710	(melt rock) B-50/721	(melt rock) B-50/717
Na (wt%)	1.98	2.05	2.43	2.55	2.52	2.92
K (wt%)	4.67	4.30	4.35	3.93	4.34	3.4
Sc	6.94	7.00	6.22	6.38	6.46	6.17
Cr	44.9	97.0	45.3	50.3	42.6	41.9
Fe (wt%)	2.00	3.61	2.25	2.41	2.13	2.36
Co	8.28	7.52	7.15	7.36	7.73	7.05
Ni	36	24	34	35	37	38
Zn	76	86	56	163	124	52
As	<1.1	<0.9	<1.9	0.73	<1.7	<1.6
Se	1.35	<1.5	<1.3	<1.2	<1.1	<1.2
Br	0.5	0.6	<0.4	<0.3	0.5	0.6
Rb	136	188	179	172	179	185
Sr	191	151	142	172	168	174
Zr	322	304	239	251	251	249
Sb	<0.2	<0.2	<0.1	<0.1	<0.2	<0.1
Cs	0.39	0.93	1.73	2.09	1.95	2.22
Ba	543	507	398	392	418	422
La	66.4	60.7	43.6	44.5	47.3	46.2
Ce	132	118	83.8	86.4	90.6	87.4
Nd	50.8	44.8	32.9	32.3	34.1	32.7
Sm	9.03	8.10	6.12	5.75	6.31	6.37
Eu	1.36	1.27	0.88	0.97	0.96	0.99
Gd	5.79	5.17	7.54	4.77	7.06	4.52
Tb	0.72	0.68	0.55	0.54	0.56	0.58
Tm	0.27	0.26	0.19	0.17	0.19	0.19
Yb	1.16	1.09	1.28	1.19	1.22	1.17
Lu	0.15	0.16	0.19	0.20	0.20	0.20
Hf	7.60	7.63	4.96	5.08	5.16	5.14
Ta	0.92	0.99	0.69	0.70	0.69	0.78
W	4.06	2.99	0.00	0.00	0.00	0.00
Ir (ppb)	<1.4	<1.5	<1.6	<1.4	<1.3	<1.4
Au (ppb)	<2.0	<1.8	<2.6	<2.3	<3.2	<3.0
Th	32.95	26.73	26.73	27.69	28.51	30.11
U	6.57	3.45	6.71	5.48	5.49	6.10

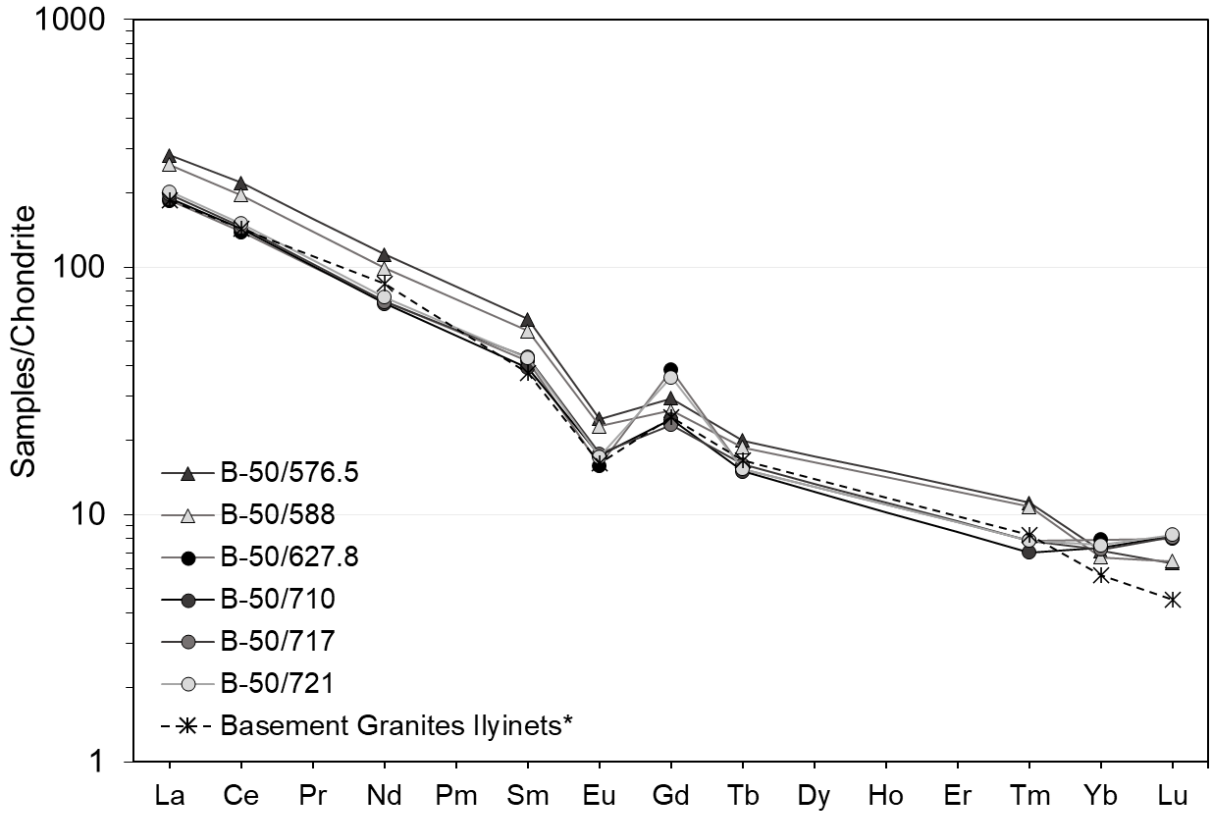

Figure 12. *Chondrite-normalized rare-earth element patterns of impact suevites (represented by a triangle) and impact melt rocks (represented by a circle) from the Boltysh impact structure. CI-normalization factors were taken from Anders and Grevesse (1989). Values of Pr, Pm, Dy, Ho, and Er contents were not measured with INAA and are interpolated. *REE concentrations of basement rocks from the Ilyinets crater (data from Gurov et al. 1998), which are also part of the Ukrainian shield, were taken for comparison.*

4.1.2. Siderophile Elements

4.1.2.1. Moderately Siderophile Elements (Cr, Co, and Ni)

The concentrations of Cr, Co, and Ni are relatively uniform throughout all samples. The Cr contents vary between 42 and 97 ppm, Co contents between 7 and 8 ppm, and Ni contents between 24 and 37 ppm. Interelement ratios of MSE are similar in all samples and shown in Figure 16. The average Cr/Co ratio of 6.0 of the Boltysh impactites roughly mirrors the Cr/Co ratios of CI-chondrites (5.4; Tagle and Berlin 2008). However, Ni/Co and Ni/Cr ratios of 4.5 and 0.7, respectively, are distinctly non-chondritic ($Ni/Co_{chondr.}$ = 20.8 and $Ni/Cr_{chondr.}$ = 3.7; Tagle and Berlin 2008).

4.1.2.2. Highly Siderophile Elements

The six melt rock and suevite samples from the Boltysh impact structure generally show low concentrations of HSEs (displayed in Table 7). The HSE contents vary between 0.06 and 0.18 ppb Re, 0.03 and 3.4 ppb Os, 0.05 and 0.36 ppb Ir, and 1.16 and 2.99 ppb Pt. Ruthenium and Pd concentrations range between 0.30 and 1.44 ppb as well as 1.27 and 4.80 ppb, respectively. Whilst most of the samples are enriched in Os, Ir, Pt, Ru, and Pd relative to the UCC, one suevite sample, B-50/576.5, has the highest HSE concentrations of all Boltysh impactites measured in this study. With an Os content of 3.4 ppb, an Ir content of 0.36 ppb, a Pt content of 2.99 ppb, and high Ru, Pd, and Re concentrations, this sample has a distinct enrichment in HSE in comparison to UCC values and even some other Boltysh impactites. Melt rock sample B-50/710 also has slightly higher HSE concentrations (0.79 ppb Os, 0.13 ppb Ir, and 4.70 ppb Pd) than the other samples. All four melt rocks have slightly higher Ir contents (0.11-0.17 ppb Ir) compared to average UCC values (0.02 ppb Ir; Peucker-Ehrenbrink and Jahn 2001), whereas suevite sample B-50/576.5 has the highest Ir concentration (0.36 ppb) of the current sample set.

Interelement variation diagrams of the Boltysh impactites, plotting the HSE abundances analyzed in this study, together with UCC values and chondrite trends, are shown in Figure 13. Most interelement variations roughly follow linear trends, which are most apparent in the Os vs. Ir and Pt vs. Ir diagrams. Except for some Os/Ir ratios, the Boltysh impactites do not show chondritic HSE interelement variations. The two samples with the highest Os concentrations (B-50/576.5 and B-50/710) plot distinctly off the chondritic Os-Ir trend, and in most cases also different from the other impactites. The measured Ir/Pt and Ru/Pd ratios of the Boltysh impactites are similar to literature data from McDonald et al. (2009) (plotted in Figure 13). Osmium concentrations (above analytical detection level) of Boltysh impactites have not been measured by any study yet; therefore, no literature data could be included in the first four interelement plots.

Table 7. Highly siderophile element concentrations of Boltysh impactites (Os was measured with TIMS and Re, Ir, Pt, Ru, and Pd were measured with ICP-MS). Literature data of Boltysh impactites, upper continental crust (UCC), and CI chondrites (CI) are given for comparison.

Boltysh	**Re [ppb]**	2σ	**Os [ppb]**	2σ	**Ir [ppb]**	2σ	**Pt [ppb]**	2σ	**Ru [ppb]**	2σ	**Pd [ppb]**	2σ
B-50/576.5	0.184	0.005	3.480	0.096	0.361	0.014	2.988	0.155	1.443	0.046	4.596	0.089
B-50/588	0.063	0.007	0.027	0.001	0.054	0.003	2.587	0.258	0.295	0.006	2.549	0.047
B-50/627.8	0.055	0.004	0.046	0.002	0.113	0.005	1.164	0.079	0.409	0.012	4.795	0.096
B-50/710	0.066	0.006	0.793	0.003	0.132	0.008	1.401	0.118	0.462	0.016	4.697	0.176
B-50/717	0.075	0.007	0.087	0.001	0.165	0.010	1.736	0.160	0.627	0.038	1.338	0.076
B-50/721	0.075	0.005	0.059	0.001	0.147	0.006	1.770	0.152	0.538	0.015	1.274	0.035
Lit. Boltysh												
B-50/627.8[(1)]	0.05	0.01	<0.1		0.07	0.03	-		<0.2		2.41	0.15
B-50/627.8[(2)]					0.10		1.31		0.10		1.00	
B-50/717[(2)]					0.07		0.29		0.07		1.36	
UCC (lit.) [(3)]	0.198		0.031		0.022		0.510		0.210		0.520	
CC (lit.) [(4)]	35-60		430-790		410-710		840-1450		610-1090		560-750	

(1) *Schmidt (1997),* ***(2)*** *McDonald et al. (2009),* ***(3)*** *Peucker-Ehrenbrink and Jahn (2001).* ***(4)*** *Fischer-Gödde et al. (2010) and Horan et al. (2013). The samples represent melt rocks, except for the samples B-50/576.5 and B-50/588, which are suevites.*

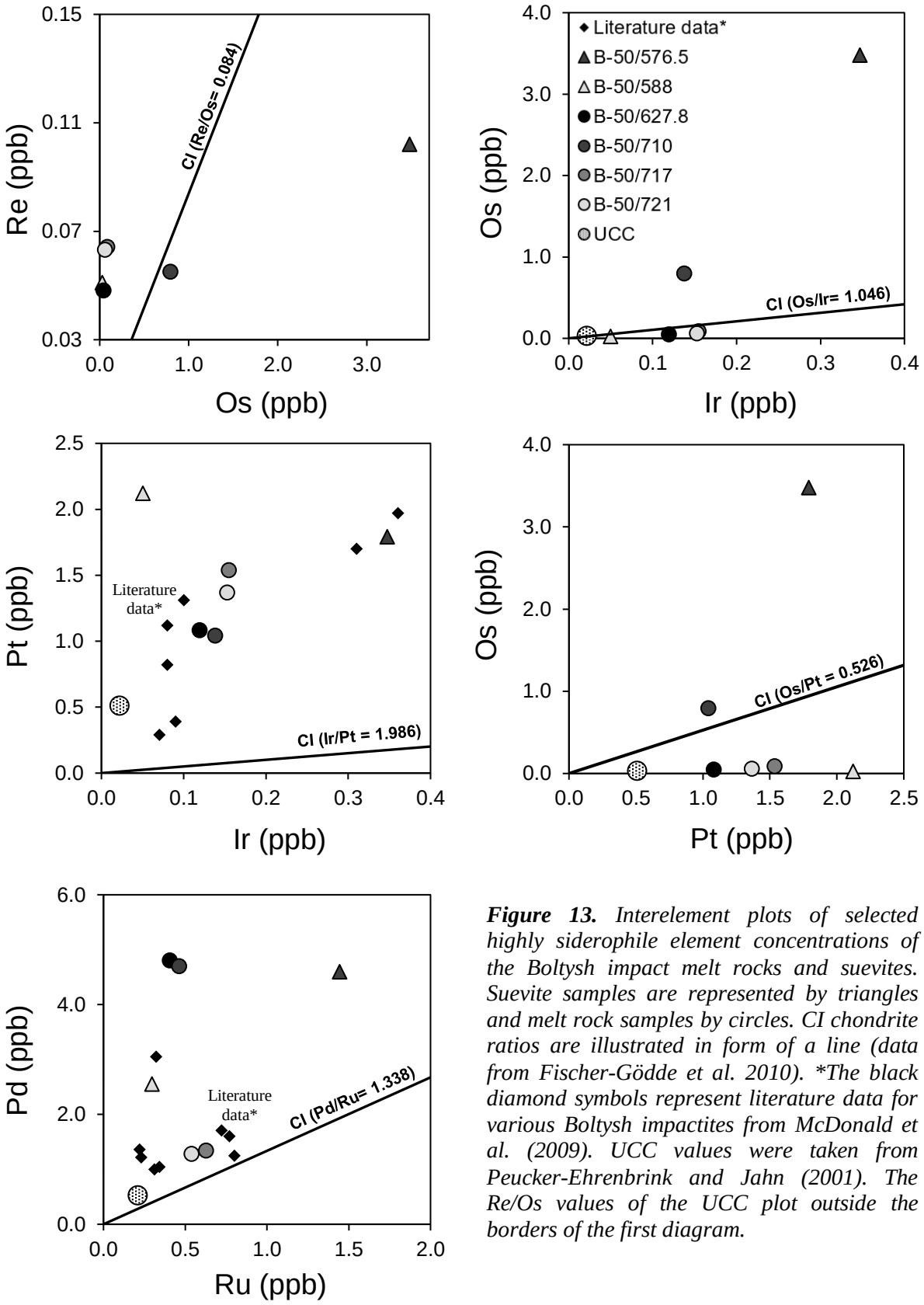

Figure 13. *Interelement plots of selected highly siderophile element concentrations of the Boltysh impact melt rocks and suevites. Suevite samples are represented by triangles and melt rock samples by circles. CI chondrite ratios are illustrated in form of a line (data from Fischer-Gödde et al. 2010). *The black diamond symbols represent literature data for various Boltysh impactites from McDonald et al. (2009). UCC values were taken from Peucker-Ehrenbrink and Jahn (2001). The Re/Os values of the UCC plot outside the borders of the first diagram.*

4.1.3. Re-Os Isotopic Composition

The Os isotope compositions of the six measured Boltysh impactites are given in Table 8. The Boltysh melt rocks and suevites generally have radiogenic (crust-like) Os isotopic compositions with $^{187}Os/^{188}Os$ ratios between 0.47 and 2.02 (the present UCC has an average composition of 1.4; Peucker-Ehrenbrink and Jahn 2001). Notably, sample B-50/576.5 has a near-chondritic ratio of 0.13 (chondrites have a $^{187}Os/^{188}Os$ of around 0.13; Walker et al. 2002). Also, this sample has the lowest $^{187}Re/^{188}Os$ ratio of ~0.14. Slightly less radiogenic ratios compared to the other impactites can also be observed in sample B-50/710 in comparison to the other impactites, but they are not as evident as in B-50/576.5. The other Boltysh samples show terrestrial crust-like $^{187}Re/^{188}Os$ ratios ranging from 4.6 to 13.9 and $^{187}Os/^{188}Os$ ratios ranging from 0.9 to 2.0.

All values are summarized in the Re-Os isotope diagram (Figure 14.1.), showing a roughly linear relationship between $^{187}Os/^{188}Os$ and $^{187}Re/^{188}Os$. Due to their comparably low Re/Os ratios, all analyzed Boltysh impactites show initial $^{187}Os/^{188}Os$ ratios (back-calculated to 66.05 ± 2.44 Ma) that are indistinguishable within analytical uncertainty from the measured $^{187}Os/^{188}Os$ ratios.

Table 8. Osmium isotopic compositions of samples from the Boltysh impact structure, measured using TIMS, along with Re and Os concentrations. For comparison, literature data of the UCC and carbonaceous chondrites (CC) are given.

	Re [ppb]	**Os [ppb]**	**$^{187}Os/^{188}Os$**	2σ	**$^{187}Re/^{188}Os$**	2σ	**($^{187}Os/^{188}Os$) initial**
Boltysh							
B-50/576.5 (Sv)	0.184	3.480	0.1341	0.0007	0.252	0.014	0.1338
B-50/588 (Sv)	0.063	0.027	2.0233	0.0099	13.93	1.960	2.0081
B-50/627.8 (Mr)	0.055	0.046	0.9399	0.0098	6.266	0.704	0.9331
B-50/710 (Mr)	0.066	0.793	0.4790	0.0004	0.415	0.039	0.4786
B-50/717 (Mr)	0.075	0.087	1.0747	0.0070	4.628	0.486	1.0697
B-50/721 (Mr)	0.075	0.059	1.1064	0.0062	6.794	0.558	1.0990
UCC (lit.) [(1)]	0.198	0.031	1.4	-	34.5	-	
CC (lit.) [(2)]	35-60	430-790	0.1262	0.0006	0.392	0.015	

(1) *Peucker-Ehrenbrink and Jahn (2001),* ***(2)*** *Walker et al. (2002) and Fischer-Gödde et al. (2010). Sv=Suevite and Mr=melt rock.*

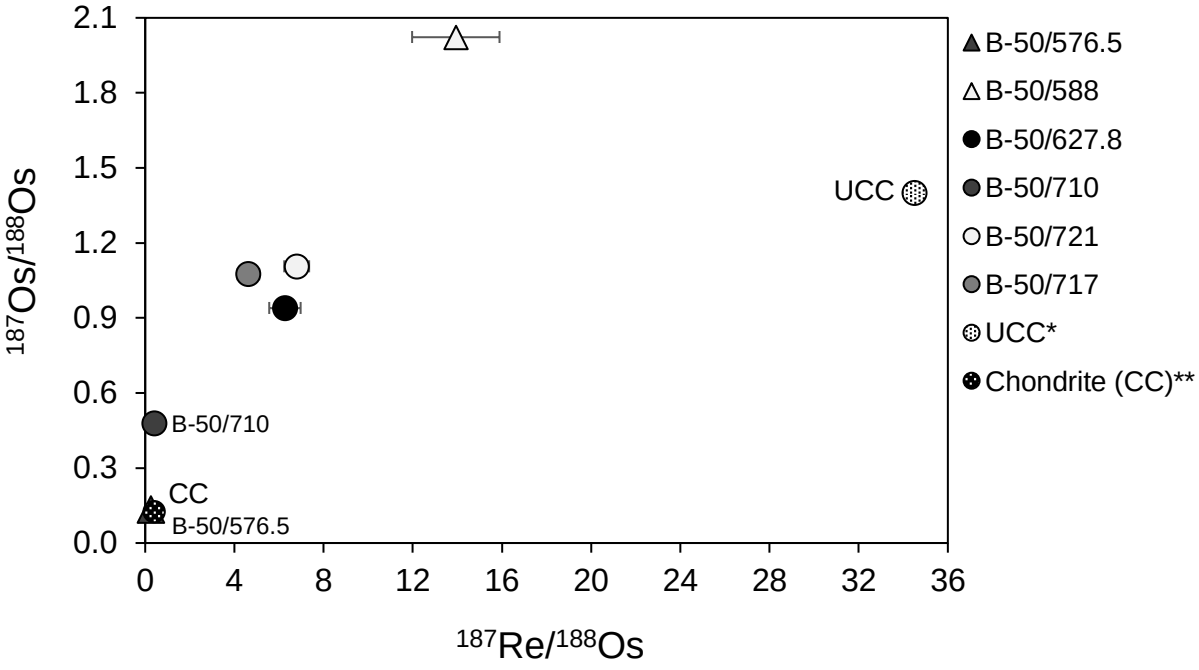

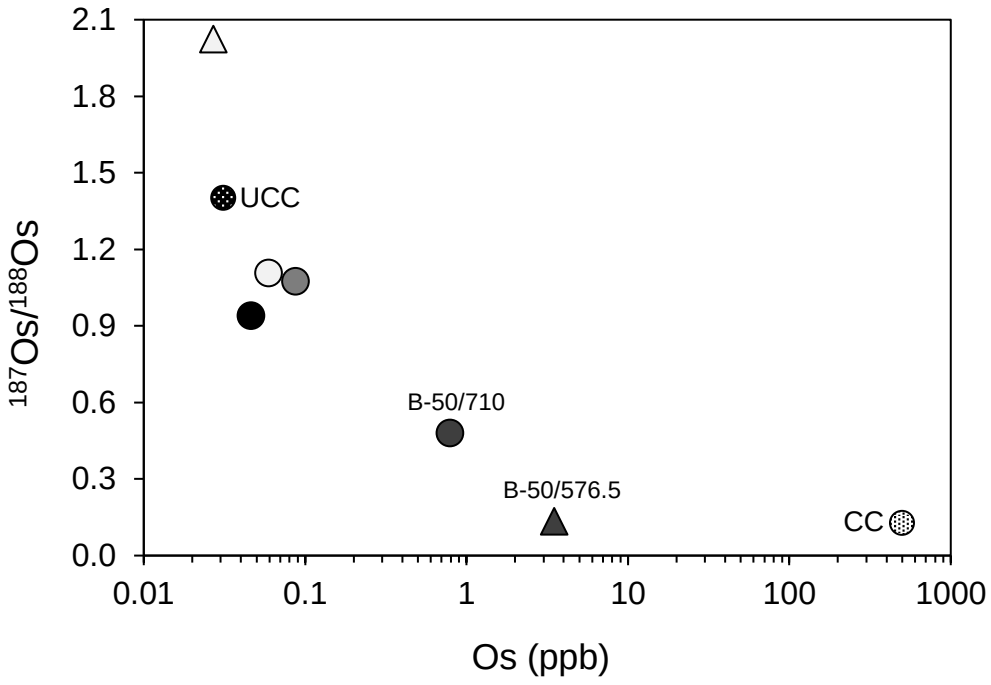

Figure 14.1. *Osmium isotopic compositions of Boltysh impactites. The impact melt rocks are symbolized by a circle and the suevites are represented by triangles. If no error bars are visible, then errors are smaller than the symbol size. Carbonaceous chondrite data (CC) from **Walker et al. (2002) and UCC values from *Peucker-Ehrenbrink and Jahn (2001) are plotted for comparison.*

Figure 14.2. *Osmium isotopic composition plotted against Os concentration (ppb) of the Boltysh samples. Note that the Os concentrations on the horizontal axis are plotted on a logarithmic scale.*

4.2. Geochemistry of the Italian Sections

4.2.1. Major-, Minor-, and Trace Elements

The INAA results of Morello, Bottaccione, and Contessa Highway samples are shown in Table 7, providing some major-, minor-, and trace element concentrations. Major element compositions of the Italian samples were not measured directly in this study; however, Na, K, and Fe concentrations have been obtained with INAA. These elements are elevated in the ALE ash samples compared to the carbonate samples (the pelagic sediments in which the ALE ash occurs). The highest iron contents were detected in the ALE ash samples (~3 wt% Fe in Bottaccione, ~2.5 wt% Fe in Morello, and ~2.2 wt% Fe in Contessa Highway), where they are about five times higher compared to the carbonates. Potassium concentrations vary between ~1.5-2.5 wt% within the ALE ash samples, relative to an average of 0.4 wt% K in the carbonates.

The ALE ash samples (MRL22-2.45, BOT-101.90, and COH-102.00) are enriched in all measured trace elements relative to the carbonates above and below the ALE ash layer. The only exception seems to be strontium, which is depleted in the ALE ash samples.

Chondrite-normalized rare-earth element patterns of the Italian samples are shown in Figure 15. All samples follow a similar trend. They show enrichment in light rare-earth elements (LREE) and exhibit a negative Eu anomaly. The rare-earth elements appear to be distinctly elevated in the ALE ash samples MRL-22-2.45, BOT-101.90, and COH-102.00 as compared to the carbonate samples. However, the REE concentrations of the ALE ash samples exhibit REE concentrations typical of marine volcanic ash layers. Deep-water volcanic ashes from Hong et al. (2019) (and references therein) were taken for reference. The marine volcanic ash beds show an overall similar REE trend to the ALE ash samples, but differences can be seen in Eu and Ce concentrations. The marine volcanic ash beds have a much stronger Eu anomaly along with a positive Ce peak compared to the ALE ash.

4.2.2. Siderophile Elements

4.2.2.1. Moderately Siderophile Elements (Cr, Co, and Ni)

Enrichments of the moderately siderophile elements (MSEs), such as Cr, Co, and Ni, can be seen in the ALE ash samples of all sections compared to carbonate samples. The Ni content of the ALE ash samples varies from 106 to 126 ppm compared to a range from 18 to 54 ppm in

the carbonate samples. Cobalt and Cr concentrations are also about five times higher in the ALE ash samples (28-38 ppm Co and 50-65 ppm Cr) than in the carbonate samples (5-10 ppm Co 9-18 and ppb Cr). In sample MRL22-2.46, obtained from the layer above the ALE ash, the MSE content is also slightly elevated. Element correlation diagrams of Cr, Co, and Ni are shown in Figure 16 (1-3). Average MSE abundances from deep-sea carbonates (Turekian and Wedepohl 1961) were plotted for comparison, roughly mirroring the compositions defined by the carbonates measured in this study. While the pelagic sediments show a nearly linear correlation in all diagrams with Cr/Co~1.6, Ni/Co~3.2, and Ni/Cr~2, the ALE ash samples, although scattered, always plot in continuation of this trend at higher concentrations.

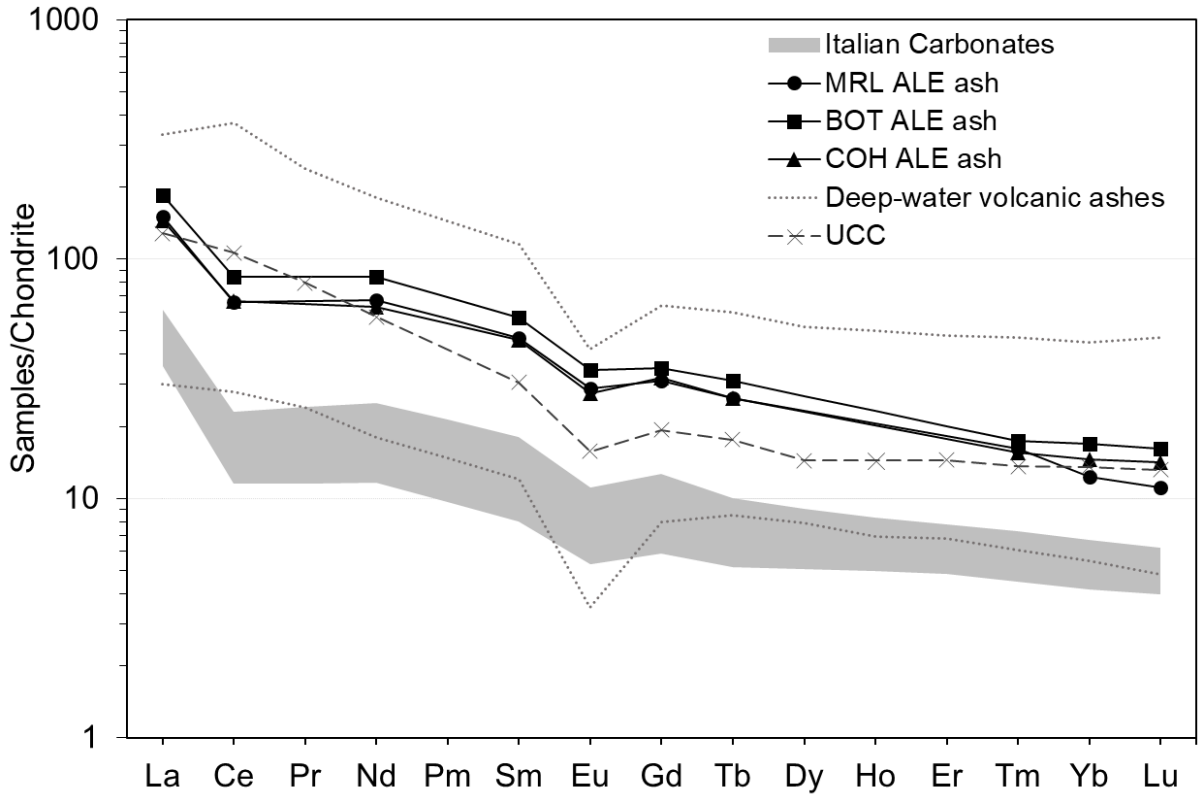

Figure 15. *Chondrite-normalized rare-earth element patterns of samples from the Italian sections, measured with INAA. The carbonates of the Italian sections are shown as grey area and the ALE ash samples (MRL-22-2.45, BOT-101.90, and COH-102.00) are plotted individually. The UCC data from Taylor and McLennan (1995) were taken for comparison. The range of REE patterns of marine volcanic ash beds in deep-water environments from Hong et al. (2019) and references therein is displayed as area between the two lines. CI-normalization factors from Anders and Grevesse (1989) were used. Values of Pr, Pm, Dy, Ho, and Er contents were not measured with INAA and are interpolated based on other REE concentrations.*

Table 9. Major, minor, and trace element data of samples from the Italian sections Morello (MRL22), Bottaccione (BOT22), and Contessa Highway (COH22) measured by INAA. Analyses are given in ppm (except as noted).

	MRL 22					BOT 22					COH 22				
(ppm)	**2.40**	**2.45**	**2.46**	**2.49**	**2.50**	**101.85**	**101.90**	**101.91**	**101.93**	**101.95**	**101.95**	**102.00**	**102.01**	**102.03**	**102.05**
Na	508	2585	981	461	335	379	1457	426	303	348	402	1326	536	387	335
K (wt%)	0.46	2.51	1.04	0.44	0.28	0.24	2.13	0.37	0.23	0.19	0.23	1.47	0.46	0.21	0.20
Sc	3.33	7.12	5.19	2.93	2.03	2.27	9.07	3.48	2.13	2.31	2.22	7.39	4.46	2.36	2.01
Cr	18.1	50.3	28.4	14.5	11.3	12.4	65.0	14.1	8.90	9.48	11.8	50.6	18.4	11.5	8.50
Fe (wt%)	0.68	2.53	1.18	0.56	0.38	0.44	2.97	0.62	0.39	0.41	0.44	2.24	0.85	0.47	0.35
Co	8.51	38.1	15.4	8.69	7.49	5.27	32.7	7.91	5.26	5.31	5.34	27.6	9.55	5.80	4.54
Ni	34	106	54	32	25	28	129	34	21	23	25	106	46	28	18
Zn	36	104	54	28	24	29	148	41	27	30	28	138	45	30	25
Ga	1.15	8.41	4.31	2.61	<2.1	0.94	22.7	1.26	<1.9	1.43	0.99	6.02	1.37	3.49	0.55
As	2.72	12.8	5.79	2.60	1.94	1.68	9.12	1.89	1.37	1.20	1.40	6.71	2.47	1.50	1.17
Se	<1.1	<1.0	<1.1	<1.0	<0.7	<1.0	<1.6	<1.1	<0.6	<1.0	<0.9	<1.6	<1.3	<1.0	<1.0
Br	0.9	1.5	0.8	0.6	0.7	0.5	1.8	0.7	0.6	0.7	0.7	1.7	0.7	0.5	0.7
Rb	17.5	65.5	30.7	15.6	11.4	10.9	67.5	15.4	9.00	9.50	10.5	58.9	20.5	12.6	8.88
Sr	305	197	231	296	302	401	257	385	394	425	429	352	424	424	361
Zr	36	124	44	28	26	27	121	43	26	26	32	116	51	31	26
Sb	0.24	0.76	0.34	0.20	0.14	0.16	0.95	0.19	0.17	0.13	0.20	1.17	0.27	0.20	0.13
Cs	1.22	3.50	1.93	0.99	0.82	0.80	4.42	1.01	0.64	0.71	0.74	3.85	1.49	0.85	0.59
Ba	27	166	45	28	21	19	185	31	20	22	19	151	38	26	21
La	18.9	35.3	22.6	16.3	13.7	16.8	43.3	18.6	13.9	14.3	15.3	34.1	21.1	15.8	13.1
Ce	15.9	40.1	22.1	14.2	11.3	14.1	50.8	17.5	12.5	12.3	12.3	40.3	20.6	13.6	11.1
Nd	13.3	30.4	17.9	12.6	9.34	11.2	38.2	12.7	8.84	9.27	9.72	28.5	14.9	10.6	8.25
Sm	3.37	6.91	4.17	2.82	2.26	2.55	8.35	2.93	2.00	2.14	2.24	6.76	3.64	2.46	1.86
Eu	0.77	1.61	0.97	0.63	0.52	0.59	1.92	0.70	0.53	0.52	0.54	1.54	0.84	0.56	0.46
Gd	3.20	6.10	3.89	2.22	2.10	2.37	6.87	2.52	2.01	1.83	2.22	6.27	3.37	2.61	1.80
Tb	0.50	0.95	0.58	0.41	0.37	0.42	1.12	0.45	0.35	0.35	0.37	0.95	0.55	0.40	0.30
Tm	0.21	0.39	0.24	0.20	0.16	0.20	0.42	0.23	0.19	0.16	0.20	0.38	0.26	0.19	0.17
Yb	1.38	1.99	1.47	1.25	1.06	1.29	2.76	1.38	1.13	1.13	1.25	2.37	1.67	1.29	1.03
Lu	0.20	0.27	0.21	0.18	0.15	0.19	0.39	0.21	0.17	0.17	0.19	0.34	0.24	0.18	0.16
Hf	0.59	3.43	1.36	0.50	0.33	0.40	3.72	0.60	0.35	0.36	0.39	2.86	0.91	0.43	0.32
Ta	0.19	2.08	0.55	0.20	0.13	0.13	1.90	0.25	0.11	0.13	0.14	1.34	0.38	0.18	0.11
W	1.6	3.8	2.0	1.3	0.6	0.7	5.6	1.4	0.4	<2	0.8	4.0	1.3	<3	0.3
Os (ppb)	<458	<598	<432	<88	<324	<408	<514	<436	<342	<369	<98	<570	<475	<348	<382
Ir (ppb)	<1.0	<1.0	<1.1	<0.9	<0.6	<0.8	<1.6	<1.0	<0.5	<0.8	<0.9	<1.6	<1.2	<0.9	<0.9
Au (ppb)	<1	<1	<1	0.3	0.3	<1	0.8	<1	<1	<1	0.3	<1	<1	<1	<1
Th	2.10	14.8	5.09	2.04	1.47	1.32	14.6	2.30	1.25	1.32	1.42	10.5	3.38	1.72	1.13
U	<0.2	0.91	0.35	0.26	0.16	0.18	0.53	0.24	<0.2	0.19	0.18	0.64	<0.2	0.20	0.13

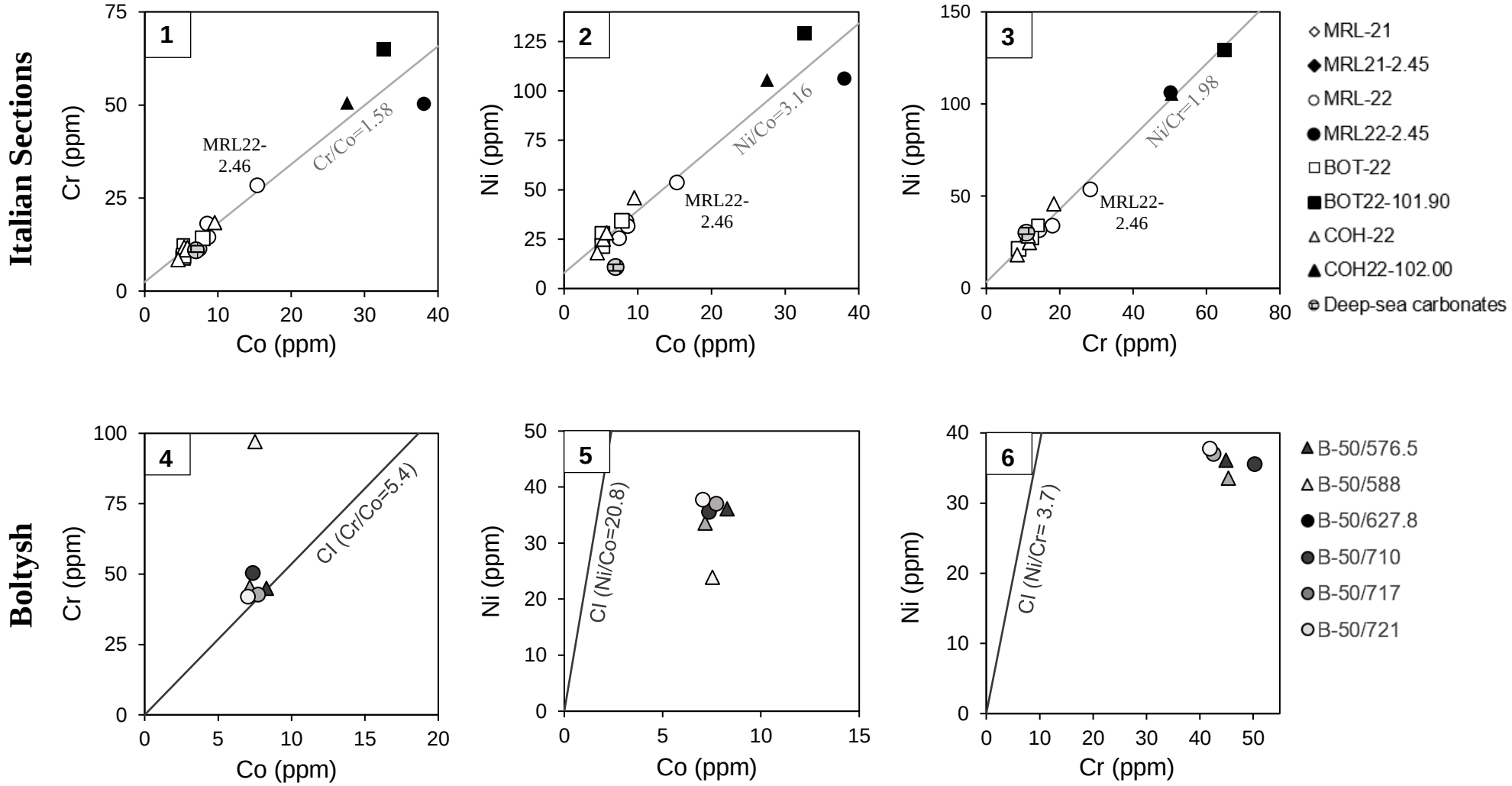

Figure 16. *Element variation diagrams of Cr, Co, and Ni of the Italian sections (1-3) and the Boltysh impactites (4-6). The average interelement ratio of the Italian samples is plotted as a grey line. The ALE ash samples show distinctly higher concentrations of Cr, Co, and Ni, than other samples of the sections. The data for the deep-sea carbonate concentrations were taken from Turekian and Wedepohl (1961) and CI interelement ratios were taken from Tagle and Berlin (2008).*

4.2.2.2. Highly Siderophile Elements

The concentrations of highly siderophile elements (HSEs) of samples from the Morello (MRL), Bottaccione (BOT), and Contessa Highway (COH) sections are reported in Table 10. Rhenium contents vary between 0.02 and 0.78 ppb in the pelagic carbonates, while they vary from 0.05 to 0.47 ppb in the ALE ash samples. Osmium concentrations in the carbonates vary from 0.02 to 0.16 ppb and are mostly comparable to typical upper terrestrial crust values of around 0.03 ppb Os (Peucker-Ehrenbrink and Jahn 2001). The ALE ash samples of both Morello sections (MRL21-2.45 and MRL22-2.45) have distinctly higher Os concentrations of up to 0.83 and 0.62 ppb, respectively. The Bottaccione ALE ash sample shows a slightly lower Os concentration of 0.15 ppb (although still elevated, compared to most pelagic sediments). Notably, the carbonate sample, obtained from five centimeters above the ALE ash in Bottaccione (BOT22-101.95), has the highest Os concentration of all samples measured in this study with a value of 1.28 ppb Os. In the Contessa Highway section, almost all samples show a similar Os concentration varying around 0.10 ppb, which is distinctly elevated relative to most pelagic sediments. The carbonate sample that shows a stratigraphic proximity to the Contessa Highway ALE ash horizon (sample COH22-101.95, taken from the layer beneath the ALE ash) exhibits the highest Os concentration of 0.85 ppb -even higher than in the Contessa ALE ash itself.

Most of the samples have Ir concentrations that agree with the average upper continental crust value of ~0.02 ppb (Peucker-Ehrenbrink and Jahn 2001). Slightly higher Ir contents (of 0.10 ppb in Morello-22, 0.09 in Bottaccione, and 0.08 in Contessa Highway) were measured in the ALE ash samples relative to the carbonate samples. However, the ALE ash in Morello-21 exhibits an UCC-like Ir concentration of 0.02 ppb, but a higher value of 0.06 ppb Os was measured for the carbonate layer directly above the ash layer of Morello-21 (sample MRL21-2.46).

Platinum contents vary from 0.5 to 2.6 ppb in the carbonate samples from all sections, and are generally higher compared to the average UCC content of 0.5 ppb Pt (Peucker-Ehrenbrink and Jahn 2001). ALE ash samples have a value of 0.9 ppb in Morello-21, 3.3 ppb in Morello-22, 3.5 ppb in Bottaccione, and 4.3 ppb in Contessa Highway. Again, one sample of Morello-21 shows an enrichment of HSEs (in this case Pt) in the stratigraphically overlying layer of the ALE ash (sample MRL21-2.46) with a Pt content of 4.1 ppb.

Ruthenium and palladium concentrations in the pelagic carbonates of all sections vary from 0.11 to 0.70 ppb and 0.57 to 2.56 ppb, respectively (for comparison, values of the UCC average around 0.21 ppb Ru and 0.52 ppb Pd; Peucker-Ehrenbrink and Jahn 2001). Palladium contents are elevated in the ALE ash samples relative to all carbonates, with concentrations of 8.2 ppb in Morello-22, 6.0 ppb in Bottaccione, and 6.6 ppb in Contessa Highway. This trend also holds for Ru, varying from 0.73 ppb in Morello-22, 0.90 ppb in Bottaccione, and 0.88 ppb in Contessa Highway. A slight enrichment of Ru and Pd can be seen in the carbonate samples, which again, are stratigraphically located directly above the ALE ash layer (MRL21-2.46 and MRL22-2.46).

Figure 17 shows element variation diagrams for all measured HSEs. The HSE interelement ratios among the carbonate samples are similar and consistent with values from the UCC. Interelement ratios of the ALE ash samples vary from 0.06 to 1.20 for Re/Os, from 1.6 to 37.6 for Os/Ir, from 32 to 52 for Pt/Ir, from 0.03 to 0.90 for Os/Pt, and from 6.8 to 11.2 for Pd/Ru. The ALE ash samples of the Morello section show slightly different Re/Os, Os/Ir, Os/Pt, and Pd/Os ratios as the carbonates, whereas the Bottaccione and Contessa Highway ALE ashes have similar HSE ratios. However, the carbonate sample from the layer beneath the Contessa Highway ALE ash, along with MRL21-21.46, also has interelement ratios that differ from those of the other carbonates.

Table 10. Highly siderophile element concentrations of the Italian sections (Os concentrations were measured with TIMS and Re, Ir, Pt, Ru, and Pd with ICP-MS). For comparative purposes, literature data of the upper continental crust (UCC) are given. The ALE ash samples are highlighted in bold.

Italian Sections	**Re [ppb]**	2σ	**Os [ppb]**	2σ	**Ir [ppb]**	2σ	**Pt [ppb]**	2σ	**Ru [ppb]**	2σ	**Pd [ppb]**	2σ
MRL21-2.40	0.067	0.007	0.051	0.002	0.022	0.003	1.836	0.183	0.106	0.005	0.618	0.043
MRL21-2.45	0.046	0.002	0.825	0.069	0.022	0.002	0.912	0.032	-	-	-	-
MRL21-2.46	0.045	0.007	0.101	0.002	0.064	0.008	4.063	0.350	0.159	0.008	3.872	0.225
MRL21-2.48	0.032	0.002	0.156	0.002	0.042	0.003	2.004	0.152	0.665	0.025	1.214	0.041
MRL21-2.50	0.027	0.002	0.037	0.001	0.017	0.001	0.496	0.015	-	-	-	-
MRL22-2.40	0.080	0.007	0.094	0.005	0.029	0.002	1.747	0.144	0.654	0.026	0.792	0.020
MRL22-2.45	0.473	0.023	0.621	0.014	0.102	0.005	3.279	0.134	0.729	0.024	8.182	0.177
MRL22-2.46	0.779	0.046	0.082	0.001	0.058	0.004	2.546	0.172	1.367	0.147	4.957	0.106
MRL22-2.48	0.055	0.005	0.108	0.002	0.047	0.004	1.235	0.072	1.128	0.064	4.769	0.164
MRL22-2.50	0.113	0.007	0.046	0.002	0.016	0.002	1.441	0.109	0.596	0.019	2.560	0.060
BOT22-101.85	0.057	0.008	0.043	0.002	0.022	0.002	0.709	0.054	0.397	0.023	1.253	0.049
BOT22-101.90	0.056	0.005	0.151	0.001	0.088	0.007	3.518	0.182	0.890	0.034	6.026	0.169
BOT22-101.91	0.037	0.004	0.020	0.001	0.026	0.002	0.669	0.055	0.577	0.024	2.041	0.052
BOT22-101.93	0.023	0.002	0.060	0.001	0.013	0.001	1.110	0.097	0.699	0.031	0.717	0.018
BOT22-101.95	0.037	0.004	1.282	0.061	0.018	0.001	1.599	0.131	0.658	0.026	0.728	0.020
COH22-101.95	0.029	0.003	0.847	0.043	0.022	0.001	3.530	0.189	0.632	0.023	0.567	0.017
COH22-102.00	0.156	0.008	0.131	0.005	0.081	0.007	4.247	0.319	0.873	0.051	6.638	0.311
COH22-102.01	0.039	0.004	0.116	0.003	0.029	0.002	1.522	0.121	0.647	0.032	1.373	0.042
COH22-102.03	0.025	0.003	0.093	0.001	0.017	0.002	2.016	0.161	0.689	0.037	0.831	0.032
COH22-102.05	0.030	0.003	0.112	0.005	0.013	0.001	1.415	0.109	0.625	0.023	1.357	0.028
UCC (lit.) [(1)]	0.198		0.031		0.022		0.510		0.210		0.520	

(1) *Peucker-Ehrenbrink and Jahn (2001)*

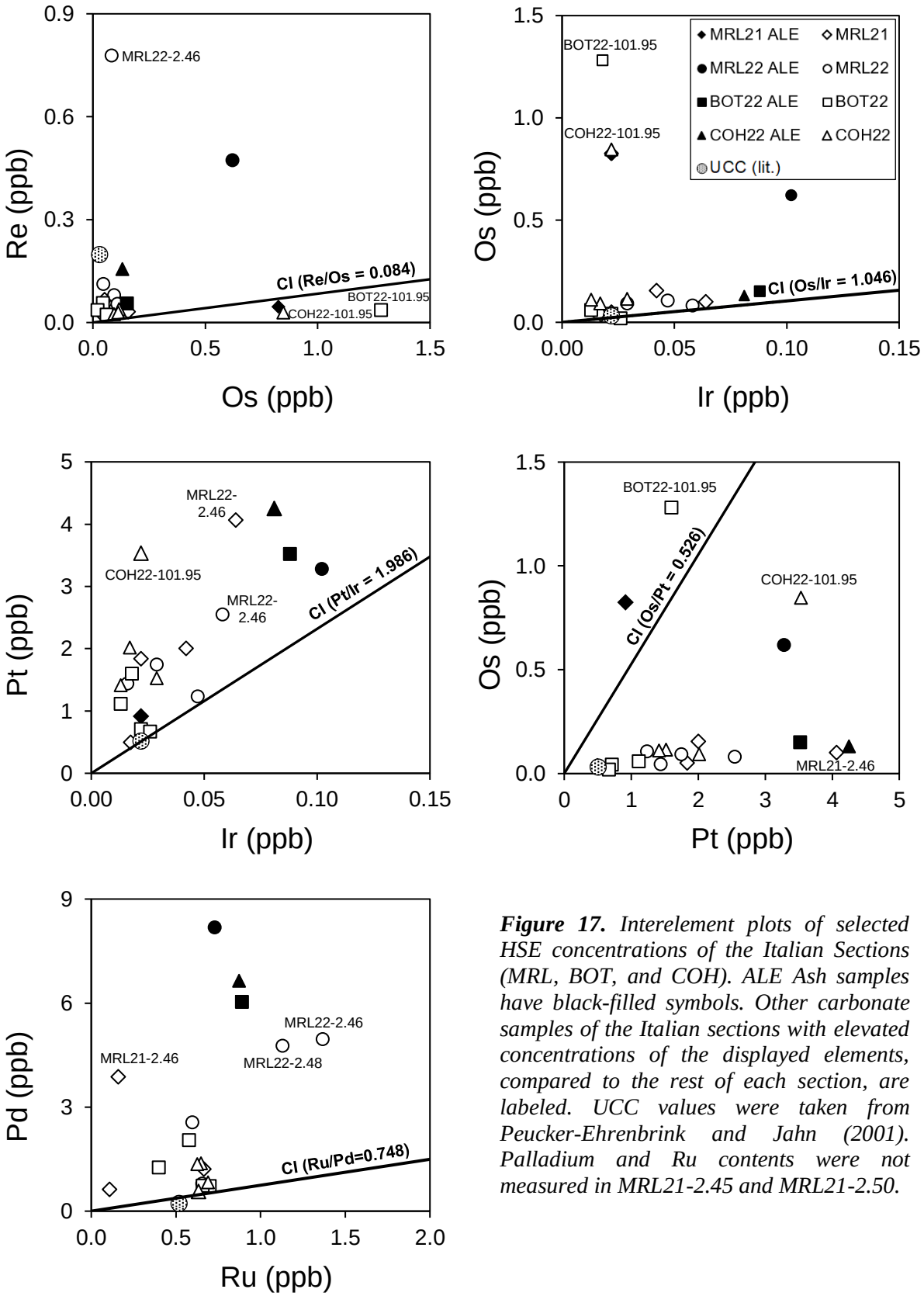

Figure 17. *Interelement plots of selected HSE concentrations of the Italian Sections (MRL, BOT, and COH). ALE Ash samples have black-filled symbols. Other carbonate samples of the Italian sections with elevated concentrations of the displayed elements, compared to the rest of each section, are labeled. UCC values were taken from Peucker-Ehrenbrink and Jahn (2001). Palladium and Ru contents were not measured in MRL21-2.45 and MRL21-2.50.*

4.2.3. Re-Os Isotopic Composition

The $^{187}Os/^{188}Os$ ratios, together with $^{187}Re/^{188}Os$ ratios and the initial $^{187}Os/^{188}Os$ ratios of samples from the Morello, Bottaccione, and Contessa Highway sections are listed in Table 11. The $^{187}Os/^{188}Os$ ratios in all measured samples vary from 0.16 to 0.70. Apart from one HSE-enriched carbonate sample (COH22-101.95) that is located stratigraphically directly underneath the Contessa Highway ALE ash horizon (see above), the $^{187}Os/^{188}Os$ ratios in the pelagic sediments vary from 0.41 to 0.70. Using their $^{187}Re/^{188}Os$ ratios (see Table 9), all of these carbonates exhibit positive and geologically meaningful initial $^{187}Os/^{188}Os$ signatures (back-calculated to 65.8 ± 1.9 Ma), ranging between 0.17 and 0.69 and averaging at 0.45 ± 0.12, most likely reflecting the typical seawater Os isotope composition in the early Danian of $^{187}Os/^{188}O$~0.4 (Peucker-Ehrenbrink et al. 1995; Peucker-Ehrenbrink and Ravizza 2000). Carbonate sample COH22-101.95, which also has the highest Os concentration of the Contessa Highway section, has a chondrite-like $^{187}Os/^{188}Os$ ratio of 0.16 (in conjunction with a similarly chondrite-like $^{187}Re/^{188}Os$ and $^{187}Os/^{188}Os$ initial ratio; see Table 9). Notably, the ALE ash sample of the Contessa Highway section (sample COH22-102.00) shows a carbonate-like (i.e., seawater-like) $^{187}Os/^{188}Os$ composition, while in the Bottaccione section, no sample (neither carbonates nor the ALE horizon) has a radiogenic $^{187}Os/^{188}Os$ composition lower than the seawater. The two other ALE ash samples of both Morello sections show the least radiogenic values (ranging from 0.22 to 0.24) compared to the adjacent carbonate samples.

An isochron diagram for the Re-Os isotopic compositions of the Italian sections is shown in Figure 18.1. The terrestrial crust (UCC) shows an $^{187}Re/^{188}Os$ ~34.5 in conjunction with a radiogenic $^{187}Os/^{188}Os$ ratio ~1.4 (Peucker-Ehrenbrink and Jahn 2001), whereas chondrites have low $^{187}Re/^{188}Os$ ratios ~0.4 together with low $^{187}Os/^{188}Os$ ratios ~0.12-0.13 (e.g., Walker et al. 2002). Both values, UCC and carbonaceous chondrites (CC), are plotted in Figure 18, together with all analyzed samples from the Italian sections. Notably, all analyzed samples plot in between the UCC and chondritic values, with three samples plotting distinctly near chondrite-like values: the two ALE ash samples from Morello (MRL21-2.45, MRL22-2.45) and COH22-101.95.

Table 11: Osmium isotopic composition of Morello, Bottaccione, and Contessa Highway, measured using TIMS. Literature data of the upper continental crust and carbonaceous chondrites are given. The ALE ash samples are highlighted in bold.

Italian Sections	**$^{187}Os/^{188}Os$**	2σ	**$^{187}Re/^{188}Os$**	2σ	**$(^{187}Os/^{188}Os)$ initial**
MRL21-2.40	0.4522	0.0065	6.496	0.920	0.4451
MRL21-2.45	0.2368	0.0030	1.508	0.109	0.2352
MRL21-2.46	0.4701	0.0006	2.212	0.406	0.4677
MRL21-2.48	0.4389	0.0032	1.017	0.078	0.4378
MRL21-2.50	0.4527	0.0045	3.621	0.418	0.4488
MRL22-2.40	0.5544	0.0150	4.294	0.611	0.5498
MRL22-2.45	0.2251	0.0026	3.673	0.267	0.2211
MRL22-2.46	0.5469	0.0032	47.75	3.444	0.4948
MRL22-2.48	0.4107	0.0048	2.516	0.280	0.4080
MRL22-2.50	0.4754	0.0072	12.24	1.349	0.4621
BOT22-101.85	0.7011	0.0098	6.765	1.264	0.6937
BOT22-101.90	0.5008	0.0028	1.854	0.182	0.4987
BOT22-101.91	0.5124	0.0058	9.258	1.541	0.5023
BOT22-101.93	0.4734	0.0064	1.904	0.216	0.4713
BOT22-101.95	0.4254	0.0065	0.143	0.023	0.4252
COH22-101.95	0.1665	0.0051	0.164	0.027	0.1663
COH22-102.00	0.4976	0.0084	5.951	0.557	0.4911
COH22-102.01	0.5262	0.0140	1.687	0.223	0.5243
COH22-102.03	0.5161	0.0054	1.341	0.182	0.5147
COH22-102.05	0.4698	0.0066	1.333	0.202	0.4683
UCC (lit.) [(1)]	1.4	-	34.5	-	
CC (lit.) [(2)]	0.1262	0.0006	0.392	0.015	

(1) *Peucker-Ehrenbrink and Jahn (2001),* ***(2)*** *Walker et al. (2002).*

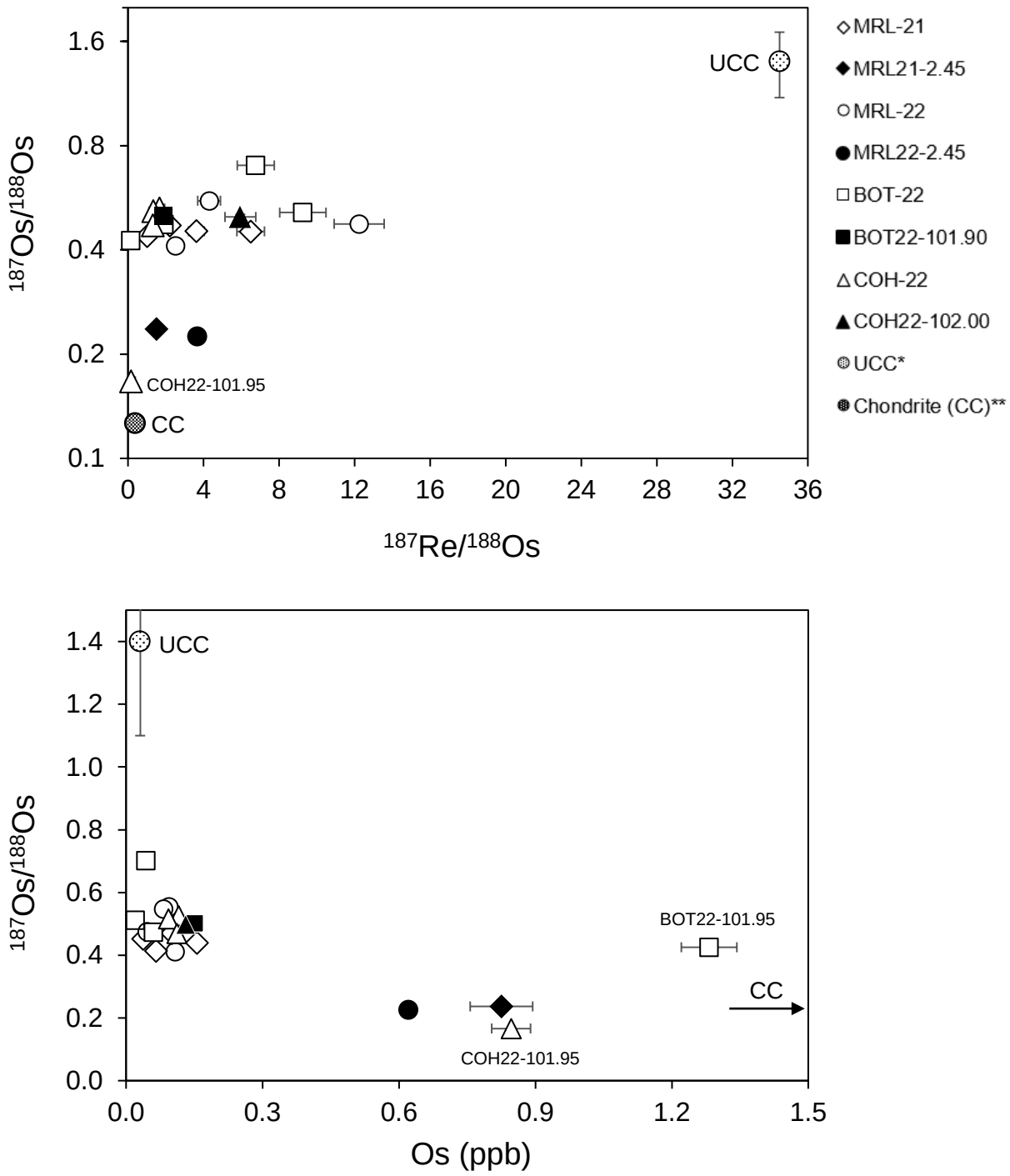

Figure 18.1. *Rhenium-osmium isotope diagram of the samples from Morello (MRL), Bottaccione (BOT), and Contessa Highway (COH) sections. The ALE ash samples are represented by black-filled symbols. If no error bars are visible, then errors are smaller than the symbol size. Values for the upper continental crust (UCC) are from *Peucker-Ehrenbrink and Jahn (2001) and carbonaceous chondrite (CC) values are from **Walker et al. (2002). Note that the $^{187}Os/^{188}Os$ ratio is plotted on a logarithmic scale.*

Figure 18.2. *Osmium isotopic composition versus Os concentration (ppb) for samples from the Italian sections. The three samples with the lowest $^{187}Os/^{188}Os$ ratio and relatively high Os concentrations plot in between the UCC and CC the lower middle of the diagram (MRL21-2.45, MRL22-2.45, and COH22-101.95); the sample with the highest Os content is BOT-101.95.*

Table 12. Overview of MSE and HSE concentrations and Os isotopic compositions of the samples from the Italian sections and Boltysh impactites. Osmium concentrations and the Os isotopic compositions were measured with TIMS; Re, Ir, Pt, Ru, and Pd concentrations were measured with ICP-MS. The ALE ash samples are highlighted in bold. MSE concentrations are given in ppm, HSE contents in ppb.

	Cr	Co	Ni	Re	Os	Ir	Pt	Ru	Pd	$^{187}Os/^{188}Os$	$^{187}Re/^{188}Os$
MRL21-2.40	-	-	-	0.067	0.051	0.022	1.836	0.106	0.618	0.4133	6.496
MRL21-2.45	-	-	-	0.046	0.825	0.022	0.912	-	-	0.2368	1.508
MRL21-2.46	-	-	-	0.045	0.101	0.064	4.063	0.159	3.872	0.4701	2.212
MRL21-2.48	-	-	-	0.032	0.156	0.042	2.004	0.665	1.214	0.4389	1.017
MRL21-2.50	-	-	-	0.027	0.037	0.017	0.496	-	-	0.4527	3.621
MRL22-2.40	18.1	8.51	34	0.080	0.094	0.029	1.747	0.654	0.792	0.5544	4.294
MRL22-2.45	50.3	38.1	106	0.473	0.621	0.102	3.279	0.729	8.182	0.2251	3.673
MRL22-2.46	28.4	15.4	54	0.779	0.082	0.058	2.546	1.367	4.957	0.5469	47.749
MRL22-2.48	14.5	8.69	32	0.055	0.108	0.047	1.235	1.128	4.769	0.4107	2.516
MRL22-2.50	11.3	7.49	25	0.113	0.046	0.016	1.441	0.596	2.560	0.4754	12.236
BOT22-101.85	12.4	5.27	28	0.057	0.043	0.022	0.709	0.397	1.253	0.7011	6.765
BOT22-101.90	65	32.7	129	0.056	0.151	0.088	3.518	0.890	6.026	0.5008	1.854
BOT22-101.91	14.1	7.91	34	0.037	0.020	0.026	0.669	0.577	2.041	0.5124	9.258
BOT22-101.93	8.9	5.26	21	0.023	0.060	0.013	1.110	0.699	0.717	0.4734	1.904
BOT22-101.95	9.48	5.31	23	0.037	1.282	0.018	1.599	0.658	0.728	0.4254	0.143
COH22-101.95	11.8	5.34	25	0.029	0.847	0.022	3.530	0.632	0.567	0.1665	0.164
COH22-102.00	50.6	27.6	106	0.156	0.131	0.081	4.247	0.873	6.638	0.4976	5.951
COH22-102.01	18.4	9.55	46	0.039	0.116	0.029	1.522	0.647	1.373	0.5262	1.687
COH22-102.03	11.5	5.8	28	0.025	0.093	0.017	2.016	0.689	0.831	0.5161	1.341
COH22-102.05	8.5	4.54	18	0.030	0.112	0.013	1.415	0.625	1.357	0.4698	1.333
B-50/576.5 (Sv)	44.9	8.28	36	0.184	3.480	0.361	2.988	1.443	4.596	0.1341	0.252
B-50/588 (Sv)	97	7.52	24	0.063	0.027	0.054	2.587	0.295	2.549	2.0233	13.925
B-50/627.8 (Mr)	45.3	7.15	34	0.055	0.046	0.113	1.164	0.409	4.795	0.9399	6.266
B-50/710 (Mr)	50.3	7.36	35	0.066	0.793	0.132	1.401	0.462	4.697	0.4790	0.415
B-50/717 (Mr)	42.6	7.73	37	0.075	0.087	0.165	1.736	0.627	1.338	1.0747	4.628
B-50/721 (Mr)	41.9	7.05	38	0.075	0.059	0.147	1.770	0.538	1.274	1.1064	6.794

Sv=Suevite and Mr= melt rock.

CHAPTER 5

Discussion

5.1. Evaluation of Extraterrestrial Components in Boltysh Impactites

Generally, the trace element content of the Boltysh impactites is similar to that of the target rock composition. According to the basement concentrations of Grieve et al. (1987) and Gurov et al. (1986) (see Table 1), the Cr and Ni contents are slightly higher in the melt rocks and suevites than in the target rocks. Overall, the Boltysh samples measured in this thesis have similar MSE compositions, which barely differ between suevites and melt rocks. Some studies (Grieve et al. 1987, Gurov et al. 1986, Grieve and Shoemaker 1994, Lorenz et al. 1999) suggested a chondritic impactor for the Boltysh impact structure, based on the elevated Cr concentrations in the melt rocks relative to the target rocks, but these contents might be too low to support assumptions regarding the nature of the projectile (c.f. Schmidt 1997). This is consistent with the Cr data obtained in this thesis, where Cr concentrations average around 54 ppm. According to MSE concentrations of Boltysh target rocks from Lorenz et al. (1999), the impactites have a higher Ni/Co and Cr/Co ratio, along with a lower Ni/Cr ratio relative to the target rocks, which suggests a significant gain of Cr. There is no evidence in the target rocks of a mafic contribution to the impactites; therefore, the additional MSE concentrations and the change in their interelement ratios are best explained by the incorporation of a meteoritic component. However, it is questionable that the meteoritic contribution is >0.1% in the Boltysh impactites and the siderophile element concentrations are generally low. Therefore, the nature of the impactor is difficult to determine.

Interelement ratios of Ni, Co, and Cr can be used to help with the identification of meteoritic signatures. The meteoritic contribution has to exceed >0.1% to allow a distinction between certain types of impactors (e.g., Koeberl 1998; Tagle and Hecht 2006). Chondrites have higher abundances of Cr (~0.2-0.3 wt%; Mason 1979; Tagle and Berlin 2008) and unique MSE interelement ratios (Ni/Cr ~3.9, Cr/Co~ 5.2, and Ni/Co~21.6; Tagle and Berlin 2008). The Boltysh impactites, except for sample B-50/588, show a near chondritic Cr/Co ratio of ~6.0. However, the Ni content is relatively low and the Ni/Co and Ni/Cr ratios of ~4.5 and

~0.7, respectively, are far too low for chondritic values. Achondrites have a much wider range of MSE concentrations and could be responsible for the non-chondritic interelement ratios in the Boltysh melt rocks and suevites (e.g., Mason 1979; Weisberg et al. 2006; Tagle and Berlin 2008; Fischer-Gödde et al. 2010; Archer et al. 2019). Achondritic meteorites generally have lower siderophile element abundances and could explain the overall low concentrations of HSEs and MSEs in the Boltysh melt rocks. However, achondrites are much less abundant in the solar system than chondrites (Grady 2000). An iron meteorite projectile is unlikely due to the overall low HSE and Ni concentrations and the high Cr abundances in the impactites (e.g., Tagle and Hecht 2006).

The CI-normalized REE patterns of the Boltysh impactites show a strong enrichment of the LREE and a small positive Eu anomaly. Slightly higher REE concentrations were measured in the suevite samples compared to the melt rock samples. Since no REE data of Boltysh target rocks were published yet, analyses from Gurov et al. (1998) of basement rocks from the Ilynets Crater, Ukraine, were taken as a reference (the target rocks of the Ilynets impact structure also consist of granites and gneisses of the Ukrainian shield and have a geochemistry similar to the Boltysh target rocks). The CI-normalized REE patterns of the Boltysh melt rock samples hardly deviate from those of the basement rocks of the Ilynets crater. Assuming the Boltysh target rocks have a geochemical composition similar to the Ilynets basement, this would suggest no significant change of REE contents caused by the impact.

With some exceptions, HSE concentrations of the Boltysh melt rocks and suevites are relatively uniform. A positive Ir anomaly (>0.1 ppb Ir) is present throughout almost all samples relative to average terrestrial crust values (UCC), while one sample (B-50/576.5) has a distinctly higher Ir content of ~0.36 ppb. These results agree with previously published Ir concentrations for Boltysh impactites of 0.07-0.36 ppb (Schmidt 1997; McDonald et al. 2009). Iridium concentrations this high are not characteristic of terrestrial crustal values and can be explained by the incorporation of meteoritic material, ultramafic or other mantle-derived material (e.g., Koeberl 1998). The other HSE concentrations are also slightly elevated in the impactites compared to average UCC values. A distinct enrichment in HSEs can be seen, again in sample B-50/576.5; it has the highest Re, Os, Ir, Pt, and Ru concentrations of all measured samples. Notably, sample B-50/710 also exhibits higher Os, Pt, Pd, and Ir contents compared to most Boltysh samples. While most impactite samples roughly follow UCC-like HSE interelement ratios, sample B-50/576.5 and, to a minor extent, B-50/710, distinctively plot off the UCC and CI trends. Pt/Ir and Pd/Ru ratios are consistent with data

from McDonald et al. (2009) (no Os concentrations of the Boltysh impactites have been published so far, therefore, interelement ratios of Re/Os, Os/Ir, and Os/Pt cannot be compared to literature data).

Impact melt rocks are a mixture of the target host rocks and meteoritic material from the impactor, therefore, they have a Re-Os isotopic composition in between the terrestrial host rocks and the projectile material. As displayed in Figure 14.1, the Boltysh impactites plot between UCC and chondritic values. This suggests mixing of radiogenic target rock material and meteoritic matter (chondrites?). The two samples with the highest HSE concentrations, discussed above, B-50/710 and B-50/576.5, plot near chondritic ratios. These two samples have distinctly lower $^{187}Os/^{188}Os$ and $^{187}Re/^{188}Os$ ratios than the other Boltysh impactites and the average UCC, B-50/576.5 even has a chondritic $^{187}Os/^{188}Os$ ratio of ~0.13. The $^{187}Os/^{188}Os$ vs. Os diagram also shows a linear correlation between the $^{187}Os/^{188}Os$ ratio and the Os concentrations of target rocks and meteorite as a result of mixing during the impact. As shown in Figure 14.2., the Boltysh impactites plot between UCC and CC values, with B-50/710 and B-50/576.5 plotting further towards chondritic trends. Osmium isotopic compositions this unradiogenic are only characteristic of meteorites, as well as mantle and mantle-derived rocks ($^{187}Os/^{188}Os_{mantle} \leq 0.13$; Meisel et al. 1993). Nevertheless, the (ultra-) mafic contribution would have to be relatively high to generate comparable $^{187}Os/^{188}Os$ signatures in the melt rocks (e.g., Koeberl 1998). The target rocks of Boltysh mainly consist of granites and gneisses and no indication of any ultramafic or mantle component has been obtained by petrographical investigations and major and trace element studies (Gurov and Gurova 1985; Grieve et al. 1987; Hölker and Deutsch 1996 Lorenz et al. 1999; Gurov et al. 2003). HSE abundances of mantle-derived rocks are commonly about 100-1000 times lower than in chondrites; distinctly elevated HSE concentrations in the melt rock would, therefore, be more indicative of a meteoritic component (e.g., Koeberl 1998, Tagle and Hecht 2006). HSE and MSE patterns of Boltysh impactites in comparison to the UCC and the PUM (primitive upper mantle) are shown in Figure 19. Incorporation of chondritic matter would yield flat CI-normalized patterns. The impactites show similar HSE and MSE patterns to the UCC, which suggests that the impactite geochemistry is strongly influenced by the target rock composition (e.g., Tagle and Hecht 2006). However, the siderophile element abundances are slightly higher in the impactites and the HSEs are less fractionated relative to UCC values. The MSE patterns of the impactites correlate with the UCC pattern, but they are significantly different from the PUM pattern. Therefore, it is highly unlikely that a significant amount of

mantle material was incorporated in the impactites. The patterns of the impactites plot between the UCC pattern and CI-chondritic values, which suggests that a small amount of meteoritic material (e.g., chondritic matter) was incorporated in the Boltysh melt rocks and suevites .

Interelement ratios of Cr, Co, and Ni are generally uniform for the Boltysh impactites, including the two B-50/710 and B-50/576.5 samples. The Ni/Cr and Ni/Co ratios are not chondritic for any of the samples. However, most samples exhibit chondrite-like Cr/Co ratios. The HSE interelement ratios of the Boltysh impactites generally do not follow chondritic trends. Achondrite meteorites can be strongly enriched in Cr compared to chondrites and due to partial melting processes in their parent body, the siderophile element ratios are disturbed and non-chondritic (e.g., Tagle and Hecht 2006). This may explain the ambiguous geochemistry of HSEs and MSEs in the Boltysh impactites, but, as achondritic meteorites are significantly less abundant than chondrites (which make up around 85 % of all meteorites; e.g. Grady 2000), it is less likely that the Boltysh impact structure was formed by an achondritic projectile.

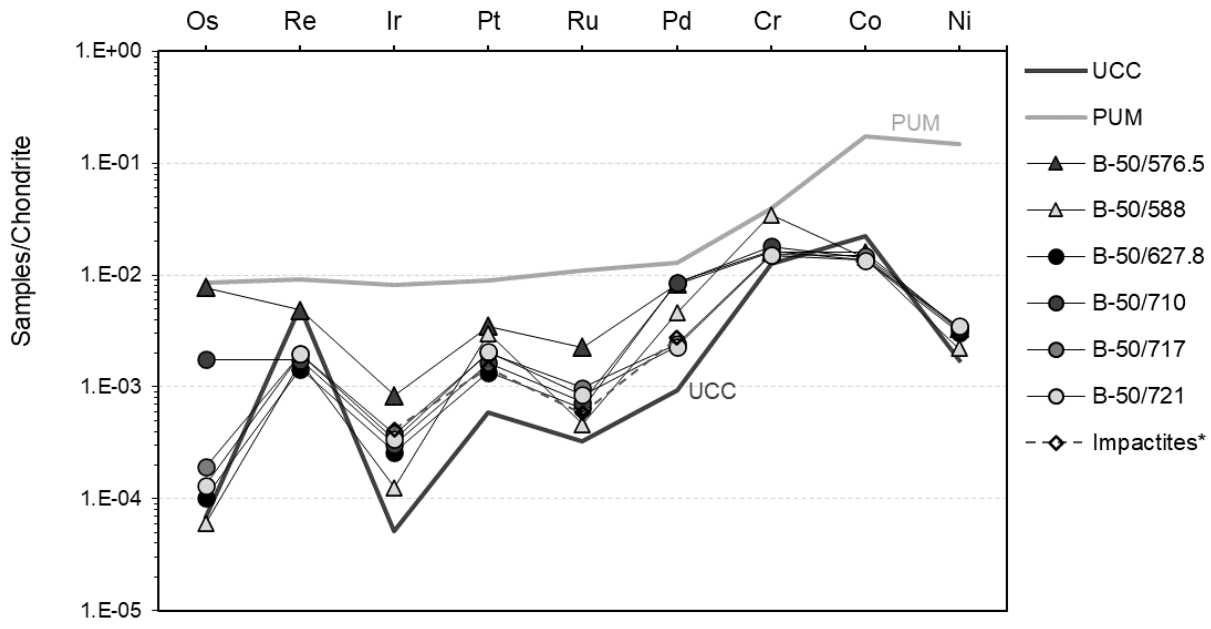

Figure 19. *CI-normalized HSE and MSE patterns of four impact melt rocks (circles) and suevites (triangles), along with element patterns from the UCC (values from Peuker-Ehrenbrink and Jahn 2001) and the primitive upper mantle (PUM) (values from Becker et al. 2006). Average HSE abundances of Boltysh impactites from *McDonald et al. (2009) were plotted for comparison.*

The non-chondritic HSE and MSE ratios of the impactites may be explained by post-impact remobilization of siderophile elements during weathering (e.g., Oberthür et al. 2003; Bowles 1986; Mountain and Wood 1988; Xiong and Wood 1999; Jaffe et al. 2002). Assuming interelement ratios were chondritic at the formation of the melt sheet and the suevites, weathering, and maybe even hydrothermal alteration, could have corrupted the chondritic signature. Another explanation could be that the impactor of the Boltysh impact structure was not of chondritic nature. As mentioned above, achondrites, have different siderophile element abundances and interelement ratios than chondrites and could be responsible for the unambiguous geochemical signature in the Boltysh impactites.

The combination of higher levels of HSE with unradiogenic Os signatures in the impactites is more characteristic of a meteoritic admixture than of a mantle component. While most samples have only slightly elevated HSE concentrations and radiogenic $^{187}Os/^{188}Os$ ratios, one sample is considered a good candidate for possibly containing a meteoritic signature. The high HSE concentrations of 3.5 ppb Os and 0.36 ppb Ir in sample B-50/576.5, along with a chondrite-like Os isotope composition, strongly suggest the presence of meteoritic material. Sample B-50/710 also shows a relatively unradiogenic ^{187}Os isotopic composition along with some elevated HSE contents (Os, Ir, Pd) relative to terrestrial crust (UCC) values. As a mantle contribution can be excluded, this sample likely indicates a meteoritic signature as well.

Interestingly, the samples B-50/717 and B-50/721 do not show elevated HSE concentrations or meteoritic ^{187}Os isotopic compositions, but they do have negative $\varepsilon^{53}Cr$ (and $\varepsilon^{54}Cr$) compositions, which are clearly outside terrestrial values and suggest the presence of meteoritic material (Koeberl et al. 2017). The negative $\varepsilon^{53}Cr$ and $\varepsilon^{54}Cr$ compositions of the two melt rocks do not suggest a carbonaceous chondritic impactor (as they have positive $\varepsilon^{53}Cr$ and $\varepsilon^{54}Cr$ values; Shukolyukov and Lugmair 2006), but rather an iron meteorite or ordinary chondrite, depleted of volatiles (Koeberl et al. 2017).

Due to the high siderophile character of Re, Os, Ir, Pt, Ru, and Pd and their extreme affinity to metallic and sulfide phases, they tend to form alloy nuggets. This so-called “nugget effect” can be observed in various impact melt rocks and leads to an inhomogeneous distribution of HSE in impact melt sheets (e.g., Palme et al. 1979; Koeberl et al. 1998; Koeberl et al. 2007; Van Acken 2012; Goderis et al. 2013; Harvey and Day 2017; Malavergne et al. 2016). Due to the different geochemical behavior of Cr, it partitions into other phases, not accommodated by the HSEs, in the impact melt sheet. Therefore, Cr and the HSEs are not necessarily associated

with each other and may occur in different phases in the melt rocks (e.g., Mittlefehldt 1992; Shiraki 1997; Koeberl et al. 2007). Different outcomes of the measurements of the same sample might be due to this inhomogeneous participation of Cr and HSEs in the melt or the nugget effect during the sample preparation (e.g., during weighing). This could be the reason why the two impact melt rocks (B-50/717 and B-50/721) have a meteoritic ε^{53}Cr composition but terrestrial HSE concentrations and ^{187}Os isotope ratios.

Even though using the most sensitive tool available for detecting meteoritic signatures, some of the Boltysh impactites still do not reveal any meteoritic signatures. This may be explained by melt sheet heterogeneity or hydrothermal alteration. Although two samples show elevated HSE concentrations and one of them has a clear unradiogenic ^{187}Os/^{188}Os isotopic composition, four Boltysh impactites lack an impactor signature. The reason for this might be a heterogeneous distribution of meteoritic component, although many impact melt sheets are overall chemically homogeneous (e.g., Palme et al. 1979). This is true for the trace element concentrations measured, especially Cr, Co, and Ni, but the HSEs and also the Os isotopic compositions are somewhat variable among the impactite samples, and they are best explained by nugget effects in the melt sheet. Other causes of an inconsistent HSE distribution can be hydrothermal alteration and other post-impact processes. Remobilization processes can leach certain elements during alteration and possibly dilute or concentrate HSE abundances. Rhenium and also Os are known to be slightly mobile during redox processes (cf. Colodner et al. 1992; Jaffe et al. 2002; Wimpenny et al. 2007; Aiglsperger et al. 2021). However, looking at the ages derived from the Re-Os isotopic system of the Boltysh impactites (except for B-50/576.5) they generally seem to agree with the ^{40}Ar/^{39}Ar age of Pickersgill et al. (2021) and do not indicate major Re loss or Os gain.

Osmium isotopic compositions that are distinctly lower than non-crustal values unambiguously indicate a presence of meteoritic material or a mantle component. In case of the Boltysh impactites, an admixture of mantle material can be excluded with fairly high probability as there is no evidence for the presence of mafic or any other mantle-derived components in the target rocks or impact rocks of the Boltysh impact structure. Therefore, the elevated HSE concentrations and a nearly chondritic ^{187}Os/^{188}Os ratio of 0.13 and ^{187}Re/^{188}Os of 0.25 in sample B-50/576.5 most likely indicate admixture of meteoritic material, although the quantity of meteoritic component cannot be determined without knowing the specific Re-Os isotopic compositions of the Boltysh target rock. The overall low HSE concentrations make it relatively difficult to determine the nature of the impactor that caused the impact

event and it is questionable if the meteoritic contribution in the impactites is high enough to derive meaningful projectile assessments. However, HSE and MSE interelement ratios and the Cr isotopic composition (Koeberl et al. 2017) are distinctly not those of a carbonaceous chondrite.

5.2. Search for a Meteoritic Component in the ALE Ash of Morello, Bottaccione, and Contessa Highway

The carbonate samples (comprising the pelagic sediments without the ALE ash and possibly geochemically affected layers by the ALE ash) of the three Italian sections have relatively homogenous trace element concentrations. The MSE concentrations of the measured carbonate samples are consistent with literature data for deep-sea carbonates (e.g., Turekian and Wedepohl 1961; Bábek et al. 2018). HSE concentrations are only slightly elevated in the carbonate samples compared to average UCC abundances and still within the terrestrial range. The average back-calculated initial $^{187}Os/^{188}Os$ of 0.45 ± 0.12 most likely reflects the seawater Os isotope composition of the early Danian, which averages around 0.4 (Peucker-Ehrenbrink et al. 1995; Peucker-Ehrenbrink and Ravizza 2000; Robinson et al. 2009).

However, a distinct $^{187}Os/^{188}Os$ excursion can be observed within the sections of Morello and Contessa Highway in the ALE ash. Both ALE ash samples of Morello (21 and 22) and the carbonate sample COH22-101.95, which stratigraphically underlies the ALE ash in the Contessa Highway section, exhibit low -in the case of the Contessa Highway sample even chondritic- $^{187}Os/^{188}Os$ and $^{187}Re/^{188}Os$ ratios. The Morello ALE ash samples have unradiogenic ratios of 0.22-0.23, which are clearly lower than terrestrial crust values ($^{187}Os/^{188}Os$ ratios of the UCC average around 1.4; Peucker-Ehrenbrink and Jahn 2001) and the values for the carbonate samples. In the Bottaccione section, no excursion in Os isotopic composition was detected in either the carbonates or the ALE ash samples. The Re-Os isochron diagram (Figure 18.1) shows that all samples plot somewhere between the upper continental crust and CI-chondrite values, with the ALE ash samples of Morello and sample COH22-101.95 plotting distinctly near chondritic values. These unradiogenic signatures can only be explained by the presence of a meteorite or a mantle component in the ALE ash layer. Chondrites have $^{187}Os/^{188}Os$ ratios of around 0.12 (e.g., Walker et al. 2002), but mantle material also has low ratios of 0.13 (Meisel et al. 1993; Sun et al. 1998; Meisel et al. 2001). Therefore, a significant mantle component in the ALE ash layer could mirror the Os isotope signatures of meteorites, but it may not necessarily be evident in the overall composition.

Apparent enrichments of HSEs in the ALE ash samples, when compared to UCC values, along with nearly chondritic Os isotopic compositions, potentially indicate a meteoritic signature. The HSE contents of the ALE ash layer are elevated in comparison to the carbonates and UCC abundances. The ALE ash samples of Morello-22, Bottaccione, and

Contessa Highway have the highest Ir, Pt, and Pd concentrations of each section. The only exception is carbonate sample MRL21-2.46 (obtained from the layer directly above the ALE ash in Morello-21), which has higher Ir and Pt concentrations than the ALE ash layer itself. Similar trends can be observed in the Contessa Highway section, where sample COH22-101.95 (directly underneath the ALE ash) has the highest Os concentration of the whole section. Nevertheless, the HSE contents of the ALE ash samples and some of the layers adjacent to the ALE ash, are elevated relative to the UCC composition and the carbonate samples. No distinct Ir anomaly can be seen in the samples of the Italian sections. Other than the K-Pg boundary layers in Gubbio, where reports of Ir concentrations yielded up to 6.3 ppb Ir (Alvarez et al. 1980), the ALE ash is merely slightly enriched in Ir, with a maximum of ~0.1 ppb. Even though the ALE ash samples have generally low Ir contents, they are elevated relative to the carbonates of the sections and UCC abundances (~0.02; Peucker-Ehrenbrink and Jahn 2001).

While the HSE interelement ratios among the carbonate samples are more or less uniform and consistent with UCC values, the ALE ash samples of Morello, along with the samples MRL21-2.46 and COH22-101.95, have distinctly different ratios. These interelement ratios are not typical for average terrestrial crustal values (UCC), but also not chondritic. The interelement ratios of Cr, Co, and Ni are clearly not chondritic in the Italian samples as well, but they seem to be constant -in the carbonates and the ALE ashes- and follow a linear trend. Although the ALE ash samples have higher MSE concentrations, their interelement ratios are similar to those in the carbonites and average UCC values.

Some minor alteration and, possibly, associated diffusion of certain elements has likely occurred in the Danian pelagic sediments of the Italian sections. During diagenesis and weathering of marine sediments redox processes can lead to post-depositional mobilization and diffusion of HSEs and other metals, consequently altering elemental concentrations and interelement ratios in the rocks (e.g., Pingitore 1982; Colodner et al. 1992; Xiong and Wood 1999; Peucker-Ehrenbrink and Hannigan 2000; Loroch et al. 2016). Furthermore, weathering can cause loss of Re, Os, Ir, Pt, and Pd, especially in organic-rich sediments (Peucker-Ehrenbrink and Hannigan 2000). Ir and Pt can be relatively mobile during redox processes within the sediment and chemical weathering (e.g., Colodner et al. 1992; Peucker-Ehrenbrink and Hannigan 2000). The element Re can be mobilized during high-temperature hydrothermal overprints, which can, in some cases, even result in a disturbance of the Re-Os isotope system (e.g., Xiong and Wood 1999; Peucker-Ehrenbrink and Hannigan 2000; Jaffe et al. 2002;

Wimpenny et al. 2007; Aiglsperger et al. 2021). It is possible that some degree of mobilization has occurred in the pelagic sediments around the ALE ash layer, as is evident by partly elevated HSEs (and MSEs) concentrations in the layers directly above or underneath the ALE ash, which can be seen in the samples MRL21-2.46, MRL22.46, and COH22-101.95. It might be plausible from the stratigraphic proximity between carbonate sample COH22-101.95 and the Contessa Highway ALE ash, that possible post-depositional alteration is responsible for the inheritance of the chondritic ^{187}Os signatures in the carbonate sample. In the Morello section, mobilization of HSE elements out of the ALE ash and into the layer above (samples MRL21-2.46 and MRL22-2.46) has likely occurred during these alteration processes.

The HSE and MSE patterns (see Figure 20) of the ALE ash samples roughly follow the fractionation pattern of the UCC and are similar to the carbonate patterns. However, the ALE ash samples have higher HSE and distinctly higher MSE concentrations than the carbonates. This enrichment in HSEs and MSEs can be explained by the incorporation of a HSE and MSE-rich component, such as meteoritic material or mantle rocks. As discussed above, mantle rocks also can also exhibit chondrite-like $^{187}Os/^{188}Os$ ratios, therefore, it is necessary to distinguish between a mantle and meteoritic signature.

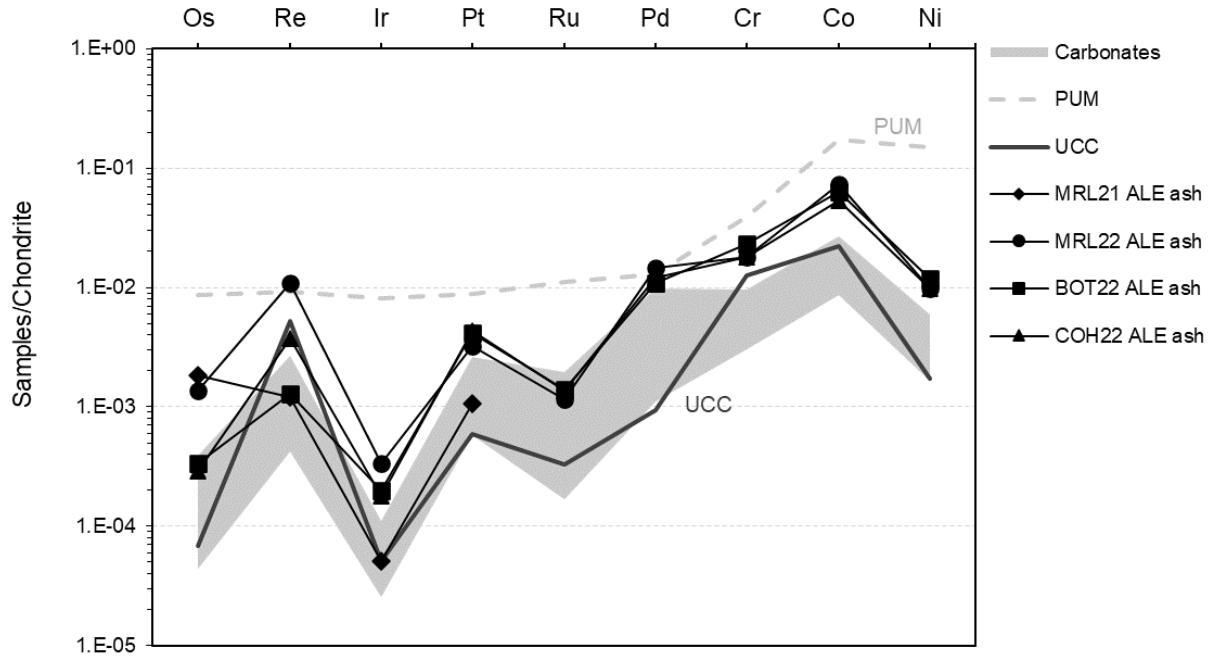

Figure 20. *CI-normalized HSE and MSE patterns of the carbonates and the ALE ash samples of the Morello, Bottaccione, and Contessa Highway sections, along with element patterns from the UCC (values from Peuker-Ehrenbrink and Jahn 2001) and the primitive upper mantle (PUM) (values from Becker et al. 2006).*

As clarified in Chapter 3.1.1, the ALE ash layer was first assumed to be a volcanic ash layer, raising the question if the elevated levels of moderately and highly siderophile elements, along with the unradiogenic Os isotopic composition, can be explained by the fact of the ALE ash being a volcanic ash layer. Basaltic ash layers, deposited in marine environments, have relatively high Cr and Co contents, comparable to the ALE ash samples (e.g., Schmitz and Asaro 1996). Furthermore, some basaltic ash beds have elevated Ir concentrations of 0.07-0.45 ppb, which is even higher than the Ir content in the ALE ash samples (e.g., Schmitz and Asaro 1996). Differences are to be observed in the lower Ni, Cs, and Th concentrations, along with higher Sc, Hf, Ce, and Ta concentrations in the basaltic ashes (e.g., Schmitz and Asaro 1996, Huber et al. 2003). A study from Schmitz et al. (2004) analyzed basaltic ash layers at the Paleocene-Eocene boundary and detected a small decrease in $^{187}Os/^{188}Os$ compared to the carbonates and clays of the rest of the section. This change in Os isotopic composition, however, is relatively small and does not compare to the significant $^{187}Os/^{188}Os$ changes observed in the ALE ash samples and in sample COH22-101.9. Furthermore, the CI-normalized REE patterns from basaltic ashes (e.g., Huber et al. 2003) differ from the ALE ash pattern in Ce and Eu, as they show a positive Ce anomaly and almost no Eu anomaly. Salic to rhyolitic ash beds have significantly lower concentrations of trace elements (especially Cr, Co, and Ni) and Ir concentrations (e.g., <0.5 ppb Ir) than the measured ALE ash abundances (e.g., Schmitz and Asaro 1996; Ruggieri et al. 2010). As the ALE ash has much higher trace and highly siderophile element concentrations than rhyolitic and salic ash beds, it is very unlikely the ALE ash layer originated from this type of volcanism. The fact of the ALE ash being a basalt-volcanic ash layer may explain elevated levels of Cr, Co, and Ir, but not the high content of Ni and, along with slightly different REE pattern (e.g., Ce and Eu) and especially the near chondritic $^{187}Os/^{188}Os$ ratio.

As the low $^{187}Os/^{188}Os$ ratios, along with high HSE and MSE concentrations in the ALE ash are not sufficiently explained by a basaltic contribution (mantle contribution), the geochemical signatures in the ALE ash layer likely reflect the presence of meteoritic material. In particular, the two Morello ALE ash samples and the COH22-101.95 sample (directly underneath the ALE ash) are considered good candidates for hosting meteoritic signatures. As opposed to this, the ALE ash of Contessa Highway probably had the unradiogenic Os isotopic signature of COH22-101.95, but due to alteration processes, this signature appears to have migrated into the layer underneath, where sample COH22-101.95 was taken from. The ALE ash of Bottaccione and Contessa Highway show inconspicuous results in terms of their Os

isotopic compositions, but they are still enriched in HSE and MSE elements compared to the carbonates. The unradiogenic Os isotopic compositions of the ALE ash layer are evident in the two Morello ALE ashes and possibly the Contessa ALE ash. This indicates that the ALE ash in Bottaccione also exhibited a lower $^{187}Os/^{188}Os$ ratio at the time of deposition, but the signature was leached out of the layer, probably during post-depositional alteration processes (as described above). Due to the sampling spacing of several centimeters, the migrated signature might have been "missed" during sampling.

While Os isotopic compositions of the Morello ALE ashes and sample COH22-101.95 are nearly chondritic, the HSE interelement ratios are distinctly not chondritic. Therefore, either leaching of HSE elements during post-impact processes led to a change in interelement ratios (see above), a background component with different compositions is involved, or the ratios have never been chondritic from the start. Either way, mobilization of HSEs likely has occurred in the Italian sections as is evident by the shift of siderophile elements from the ALE ash layer into the adjacent layers.

5.3. Evaluation of a Possible Connection between the ALE ash in Italy and the Boltysh Impact

As discussed in detail above, the unradiogenic $^{187}Os/^{188}Os$ isotope ratios and high concentrations of HSE and moderately siderophile elements (Cr, Co, and Ni) in most of the ALE ash samples and sample COH22-101.95 (from the layer stratigraphically immediately underlying the ALE ash in Contessa Highway) suggest the presence of a meteoritic component. If the geochemical signatures are indeed meteoritic, it might be due to the deposition of distal ejecta, derived from an impact event.

A new study of the Boltysh crater in Ukraine yielded a $^{40}Ar/^{39}Ar$ age of 65.39 ± 0.14/0.16 Ma (Pickersgill et al. 2021), which coincides, within errors, with the astronomical age determined for the ALE ash layer in the Italian sections of 65.440 ± 0.005 Ma (Sinnesael et al. 2016). During impact events, large volumes of gas, dust, and rock components are ejected and can travel thousands of kilometers from the impact crater before being deposited as distal impact ejecta (e.g., Melosh 1989, Koeberl 1994). Therefore, it might be possible that distal ejecta, derived from the Boltysh impact event, was deposited within the Scaglia Rossa formation in Gubbio, Italy. As the age of the ALE ash coincides with the impact age of Boltysh, it may be possible that this ash layer includes distal Boltysh impact ejecta.

As discussed above, the Boltysh impactites show only slightly elevated HSE concentrations; therefore, distal ejecta deposits probably have low concentrations of these elements as well, which would agree with the results of the measured ALE ash samples. HSE interelement ratios of the Boltysh impactites and the ALE ash samples show a significant variation but are mostly not congruent. The Cr/Co and Ni/Cr interelement ratios of the ALE ash samples are not consistent with those of the Boltysh impactites. This may be attributed to element fractionation processes during the impact (e.g., Mittlefehldt et al. 1992; Glikson and Allen 2004) and/or mobilization of siderophile elements during diagenesis and weathering (Shaw et al. 1990; Lafuente et al. 2008). However, the supposed meteoritic component might as well be too small (<0.1%) for a meaningful correlation of the MSE interelement ratios of Boltysh and the ALE ash.

As the Boltysh impact structure has a relatively small crater diameter of 24 km and the (present) distance to the Italian sections is rather far, about 1600 km, the distal ejecta layer is

expected to be thin. With equations from (1) McGetchin and Settle (1973) and (2) Glass and Pizzuto (1994), the thickness of distal impact ejecta can be estimated:

$$(1)\ \ t = 0.14\ R^{0.74}(r/R)^{-3.5}$$

$$(2)\ \ t = 0.02\ R\ (r/R)^{-4.4}$$

where t equals the ejecta thickness, R is the crater radius, and r is the distance from the crater center to the supposed ejecta layer (*-3.5* in (1) is based on data from nuclear craters with atmospheric effects). According to these calculations, a distal ejecta layer from the Boltysh impact structure would have an estimated thickness of (2) 0.1- (1) 5.3µm in Gubbio. However, such values are based on continuous deposition; it is known that in many cases, for example, related to tektites, heterogenous ejecta with millimeter- to centimeter-sized bodies can be deposited hundreds to thousands of kilometers from the impact site (e.g., Koeberl 1994). The possibility of sampling an ejecta layer that is only a few micrometers thick is very low, especially with a sampling interval of a few centimeters such as in this study. Nevertheless, a possible meteoritic signature can be found in the ALE ash layers (or in the layers directly above or underneath) from the Italian sections. This suggests that the supposed ejecta layer might have been deposited as the ALE ash layer or within the ALE ash layer in the Italian sections.

The presence of a meteoritic component in the ALE ash layer, along with the overlapping age of the Boltysh impact event and the ALE ash deposition age, suggests (but does no prove) that the two are correlated with each other. Nevertheless, it also cannot be ruled out (but it is very unlikely), that the meteoritic component in the ALE ash could have been caused by another as-yet-unknown (coeval) impact event at that time. Further investigations into the geochemistry of the ALE ash might help establish a stronger correlation between the Boltysh impact structure and the ALE ash. Analyses of the Cr isotopic composition might help with the identification of the type of the supposed meteoritic component in the ALE ash and the correlation with the Boltysh impactor. However, the meteoritic contribution in the ALE ash has to exceed 1% to better constrain the type of meteorite with Cr isotopes (c.f. Koeberl 1998). This might not be the case in the ALE ash, as the MSE and HSE concentrations are generally low. Furthermore, the sampling intervals of the Italian sections were relatively wide; closer sampling spaces near the ALE ash layer could lead to additional and more precise information.

CHAPTER 6

Conclusions

The highly and moderately siderophile element concentrations of the six Boltysh impactites agree with published literature data of Boltysh melt rocks (Grieve et al. 1987; Schmidt 1997; Lorenz et al. 1999; McDonald et al. 2009). The Boltysh impactites generally have slightly elevated HSE concentrations compared to average terrestrial crust values (UCC). A small positive Ir anomaly was observed in most Boltysh impactites. However, only two of the impactites show less radiogenic Os isotopic compositions compared to the UCC and the other impactites. Suevite sample B-50/576.5 shows particularly high HSE concentrations and a chondritic $^{187}Os/^{188}Os$ ratio of 0.13, furthermore melt rock sample B-50/710 also has elevated HSE abundances and a slightly less radiogenic $^{187}Os/^{188}Os$ ratio. A mantle distribution can be excluded with high probability in the impactites of Boltysh; therefore, the unradiogenic Os signatures, along with the elevated HSE abundances, are best explained by the presence of a meteoritic component. The Os isotopic compositions of impactites with near-chondritic values and the high Cr contents of all samples suggest a chondritic impact projectile for the Boltysh impact structure. The Boltysh impactites show near chondritic Cr/Co ratios, but the Ni content and Ni/Co, Ni/Cr ratios are too low for chondritic values. Most interelement ratios of the HSEs vary between the impactites but are distinctly non-chondritic in all samples. This

The presence of unradiogenic $^{187}Os/^{188}Os$ isotope ratios, along with elevated concentrations of HSEs and MSEs in the ALE ash samples in Morello (21 and 22) and in the layer directly underneath the ALE ash in Contessa Highway relative to the carbonates of the sections, suggests the potential existence of a meteoritic component. However, siderophile element mobility likely has occurred during post-depositional alteration processes in the pelagic sections to some degree and leading to a minor shift in HSE (and MSE) concentrations. These ambiguous results make it difficult to estimate the nature of the Boltysh projectile.

Due to the overlapping age of the ALE ash and the Boltysh impact event, the deposition of distal ejecta derived from the Boltysh impact event within the Scaglia Rossa formation in Gubbio, Italy, is a plausible explanation for the observed geochemical signatures in the ALE ash. The unradiogenic Os isotope composition, along with elevated HSE concentrations in the

ash layer compared to the carbonates of the sections, suggest the incorporation of meteoritic matter. The estimated thickness of the distal ejecta layer from Boltysh suggests that specifically sampling such a thin layer in the Italian sections is unlikely, given the sampling interval of a few centimeters, but of course any ejecta deposited on the seafloor would be mixed in with local sediments. Nevertheless, the presence of a potential meteoritic signature within the ALE ash layers, along with the overlapping age of the Boltysh impact event and the ALE ash deposition, supports the suggestion that Boltysh impact ejecta were deposited in the ALE ash layer. Further investigation, such as analyses of Cr isotopic compositions of the ALE ash, may help to identify the nature of the impactor involved with the supposed ejecta layer. A stronger correlation may be established if the impactor is consistent with the Boltysh impact projectile. Narrower sampling intervals around the ALE ash and its adjacent layers, are suggested to gain further insight into the geochemistry and its potential meteoritic component.

References

Aiglsperger T., González-Jiménez J. M., Proenza J. A., Galí S., Lono F., Griffin W. L., and O'Reilly S. Y. 2021.Open system Re-Os isotope behavior in platinum-group minerals during laterization? *Minerals* **11**(10):1083.

Alonso J. I. G., and Rodrígez-González P. 2013. Isotope dilution mass spectrometry. Cambridge: Royal Society of Chemistry. 472 p.

Alvarez L. W., Alvarez W., Asaro F., and Michel H. V. 1980. Extraterrestrial cause for the Cretaceous-Tertiary extinction. *Science* **208**:1095–1108.

Anders E., and Grevesse N. 1989. Abundances of the elements: Meteoritic and solar. *Geochimica et Cosmochimica Acta* **53**(1):197-214.

Archer G. J., Walker R. J., and Irving A. J. 2019. Highly siderophile element and ^{187}Re-^{187}Os isotopic systematics of ungrouped achondrite Northwest Africa 7325: Evidence for complex planetary processes. *Meteoritics and Planetary Science* **54**(5):1042-1050.

Arthur M. A., and Fischer A. G. 1977. Upper Cretaceous–Paleocene magnetic stratigraphy at Gubbio, Italy I. Lithostratigraphy and sedimentology. *Geological Society of America Bulletin* **88**:367–371.

Bábek O., Faměra M., Hladil J., Kapusta J., Weinerová H., Šimíček D., Slavík L., and Ďurišová J. 2018. Origin of red pelagic carbonates as an interplay of global climate and local basin factors: Insight from the Lower Devonian of the Prague Basin, Czech Republic. *Sedimentary Geology* **364**:71-88.

Bass Y. B., Galaka A. I., and Grabovskiy V. I. 1967. The Boltysh oil shales (in Russian). *Razvedka i Okhrana Nedr* **9**:11-15.

Barrat J. A., Zanda B., Moynier F., Bollinger C., Liorzou C., and Bayon G. 2012. Geochemistry of CI chondrites: Major and trace elements and Cu and Zn isotopes. *Geochimica et Cosmochimica* Acta **83**:79-92.

Birck J. L., Barman M. R., and Capmas F. 1997. Re-Os Isotopic measurements at the femtomole level in natural samples. *Geostandards and Geoanalytical Research* **21**:19–27.

Bland P. A. 2005. The impact rate on Earth. *Philosophical Transactions of the Royal Society A (2005)* **363**:2793-2810.

Bode P., Greenberg R. R., and De Nadai Fernandes E. 2009. Neutron activation analysis: A primary (Ratio) method to determine SI-traceable values of element content in complex samples. *Chimia* **63**(10):678-680.

Bowles J. F. W. 1986. The development of platinum-group minerals in laterites. *Economic Geology* **81**(5):1278-1285.

Cohen A. S., and Waters F. G. 1996. Separation of osmium from geological materials by solvent extraction for analysis by thermal ionization mass spectrometry. *Analytica Chimica Acta* **332**:269–275.

Colodner D. C., Boyle E. A., Edmond J. M., and Thomson J. 1992. Post-depositional mobility of platinum, iridium and rhenium in marine sediments. *Nature* **358**:402-404.

Creaser R., Papanastassiou D., and Wasserburg G. 1992. Isotopic analysis of Os and Re with negative thermal ion mass spectrometry and application to the age and evolution of iron meteorites. *Meteoritics* **27**:397–401.

Dabek J., and Halas S. 2007. Physical foundations of rhenium-osmium method – a review. *Geochronometria* **27**(1):23-26.

Daly R. T., Schultz P. H., Lassiter J. C., Loewy S. W., Thompson L. M., and Spray J. G. 2018. Contrasting meteoritic signatures within the Clearwater East and Clearwater West impact structures: The view from osmium isotopes. *Geochimica et Cosmochimica Acta* **235**:262-284.

Earth impact database. 2023. http://www.passc.net/EarthImpactDatabase/New%20website_05-2018/Index.html [accessed 10.06.2023].

Esser B. K., and Turekian K. K. 1993. The osmium isotope composition of the continental crust. *Geochimica et Cosmochimica Acta* **57**(13):3093-3104.

Fischer-Gödde M., Becker H., and Wombacher F. 2010. Rhodium, gold and other highly siderophile element abundances in chondritic meteorites. *Geochimica et Cosmochimica Acta* **74**:356–379.

Frei R., and Frei K. M. 2002. A multi-isotopic and trace element investigation of the Cretaceous–Tertiary boundary layer at Stevns Klint, Denmark – inferences for the origin and nature of siderophile and lithophile element geochemical anomalies. *Earth and Planetary Science Letters* **203**(2):691-708.

French B. M., and Koeberl C. 2010. The convincing identification of terrestrial meteorite impact structures: What works, what doesn't, and why. *Earth-Science Reviews* **98**:123–170.

Geo Lab. 2001. OKUM (Ontario komatiite ultramafic) Geo Lab's in-house reference material. Ontario Geological Survey (Sudbury, ON, Canada). 2p.

Glass B. P., and Pizzuto J. E. 1994. Geographic variation in Australasian microtektite concentrations: Implications concerning the location and size of the source crater. *Journal of Geophysical Research* **99**(E9):19075-19081.

Glikson A., and Allen C. 2004. Iridium anomalies and fractionated siderophile element patterns in impact ejecta, Brockman Iron Formation, Hamersley Basin, Western Australia: evidence for a major asteroid impact in simatic crustal regions of the early Proterozoic earth. *Earth and Planetary Science Letters* **220**(3-4):247-264.

Goderis S., Tagle R., Belza J., Smit J., Montanari A., Vanhaecke F., Erzinger J., and Claeys P. 2013. Reevaluation of siderophile element abundances and ratios across the

Cretaceous–Paleogene (K–Pg) boundary: Implications for the nature of the projectile. *Geochimica et Cosmochimica Acta* **120**:417-446.

Govindaraju K. 1989. Compilation of working values and sample descriptions for 272 geostandards. *Geostandards Newsletter* **13**(s1):1-113.

Grady M. M. 2000. Catalogue of meteorites, 5th edition. Cambridge: Cambridge University Press. 696 p.

Greenberg R. R., Bode P., and De Nadai Fernandes E. A. 2011. Neutron activation analysis: A primary method of measurement. *Spectrochimica Acta Part B: Atomic Spectroscopy* **66**:193–241.

Grieve R. A., and Robertson P. B. 1978. The terrestrial cratering record: Current status of observations. *Icarus* **38**(2):212-229.

Grieve R. A., and Shoemaker E. M. 1994. The record of past impacts on Earth. In: *Hazards due to comets and asteroids*, edited by Gehrels T., Tucson: University of Arizona Press. pp. 417–462.

Gulick S. P. S., Christeson G. L., Barton P. J., Grieve R. A. F., Morgan J. V., and Urrutia-Fucugauchi J. 2013. Geophysical characterization of the Chicxulub impact crater. *Reviews of Geophysics* **51**(1):31-52.

Gurov E. P., and Gurova H. P. 1985. Boltysh Astrobleme: Impact crater pattern with a central uplift (abstract). *Lunar and Planetary Science XVI*. pp. 310–311.

Gurov E. P., Kolesov G. M., and Gurova E. P. 1986. Composition of impactites of the Boltysh astrobleme (in Russian). *Meteoritika* **45**:150–155.

Gurov E. P., Koeberl C., and Reimold W. U. 1998. Petrography and geochemistry of target rocks and impactites from the Ilyinets Crater, Ukraine. *Meteoritics and Planetary Science* **33**(6):1317-1333.

Gurov E. P., Kelley S. P., and Koeberl C. 2003. Ejecta of the Boltysh impact crater in the Ukrainian Shield. In: *Impact Markers in the Stratigraphic Record*, edited by Koeberl C. and Martinez-Ruiz F., Heidelberg: Springer. pp. 179-202.

Hall G. E. M., and Pelchat J. C. 1994. Analysis of geological materials for gold, platinum and palladium at low ppb levels by fire assay-ICP mass spectrometry. *Chemical Geology* **115**(1-2):61-72.

Harvey J., and Day J. 2017. Highly siderophile and strongly chalcophile elements in high-temperature geochemistry and cosmochemistry. Berlin, Boston: De Gruyter. 774 p.

Herr W., Hoffmeister W., Hirt B., Geiss J., and Houtermans F. G.1961. Versuch zur Datierung von Eisenmeteoriten nach der Rhenium-Osmium-Methode. *Zeitschrift für Naturforschung* **16**(10):1053-1058.

Heumann K. G. 1992. Isotope dilution mass spectrometry. *International Journal of Mass Spectrometry and Ion Processes* **118-119**:575-592.

Hölker T., and Deutsch A. 1996. The Boltysh impact structure, Ukraine: Geochemistry of the melt sheet (abstract #1278). 27th Lunar and Planetary Science Conference. CD-ROM.

Honda M., and Imamura M. 1971. Half-life of Mn^{53}. *Physical Review C* **4**:1182–1188.

Hong H., Algeo T. J., Fang Q., Zhao L., Ji K., Yin K., Wang C., and Cheng S. 2019. Facies dependence of the mineralogy and geochemistry of altered volcanic ash beds: An example from Permian-Triassic transition strata in southwestern China. *Earth-Science Reviews* **190**:58-88.

Horan M. F., Morgan J. W., Walker R. J., and Grossman J. N. 1992. Rhenium-Osmium isotope constraints on the age of iron meteorites. *Science* **255**(5048):1118-1121.

Huber H., Koeberl C., and Egger H. 2003. Geochemical study of lower Eocene volcanic ash layers from the Alpine Anthering Formation, Austria. *Geochemical Journal* **37**(1):123-134.

Jaffe L. A., Peucker-Ehrenbrink B., and Petsch S. T. 2002. Mobility of rhenium, platinum group elements and organic carbon during the black shale weathering. *Earth and Planetary Science Letters* **198**(3-4):339-353.

Jarosewich E., Clarke R. S. Jr., Barrows J. N. 1987. The Allende meteorite reference sample. *Smithsonian Contributions to the Earth Sciences* **27**:1-49.

Johnsson M. J., and Reynolds R. C. 1986. Clay mineralogy of shale-limestone rhythmites in the Scaglia Rossa (Turonian-Eocene), Italian Apennines. *Journal of Sedimentary Research* **56**:501–509.

Jordan B. R., Yancey T. E., Heinrich P. V., Miller B. V., and McGuire K. 2019. The age and geochemistry of volcanic ash in the Catahoula Formation of Louisiana, Mississippi, and Texas, USA. *The Journal of Geology* **127**(2):207-222.

Kashkarov L. L., Nazarov M. A., Kalinina G. V., Lorenz K. A., and Kononkova N. N. 1998. Fission track dating of the Boltysh impact crater, Ukraine (abstract #1257). *29th Lunar and Planetary Science Conference*. CD-ROM.

Kelley S. P., and Gurov E. 2002. Boltysh, another end-Cretaceous impact. *Meteoritics and Planetary Science* **37**:1031–1043.

Koeberl C. 1993. Instrumental neutron activation analysis of geochemical and cosmochemical samples: A fast and reliable method for small sample analysis. *Journal of Radioanalytical and Nuclear Chemistry Articles* **168**:47–60.

Koeberl C. 1994. Tektite origin by hypervelocity asteroidal or cometary impact: target rocks, source craters, and mechanisms. *Geological Society of America Special Paper* **293**:133-151.

Koeberl C. 1998. Identification of meteoritic components in impactites. *Geological Society, London, Special Publications* **140**(1):133.

Koeberl C. 2006. The record of impact processes on the early Earth: A review of the first 2.5 billion years. In: *Processes on the Early Earth*, edited by Reimold W. U., and Gibson R. L., Boulder: Geological Society of America Special Paper 405. pp. 1–22.

Koeberl C. 2013. Asteroid Impact. In: *Encyclopedia of Natural Hazards*, edited by Bobrowsky P. T., Dordrecht: Springer Netherlands. pp. 18–28.

Koeberl C. 2014. 2.5 - The geochemistry and cosmochemistry of impacts. In: *Treatise on Geochemistry (Second Edition)*, edited by Holland H. D., and Turekian K. K., Oxford: Elsevier. pp. 73–118.

Koeberl C., and Shirey S. B. 1993. Detection of a meteoritic component in Ivory Coast tektites with rhenium–osmium isotopes. *Science* **261**(5121):595–598.

Koeberl C., and Shirey S. B. 1996. Re–Os isotope study of rocks from the Manson impact structure. In: *The manson impact structure, Iowa: Anatomy of an impact crater*, edited by Koeberl C. and Anderson R. R., Boulder: Geological Society of America Special Paper 302. pp. 331–339.

Koeberl C., and Shirey S. B. 1997. Re–Os isotope systematics as a diagnostic tool for the study of impact craters and distal ejecta. *Palaeogeography, Palaeoclimatology, Palaeoecology* **132**(1-4):25-46.

Koeberl C., Reimold W. U., and Shirey S. B. 1996. Re-Os isotope and geochemical study of the Vredefort Granophyre: Clues to the origin of the Vredefort structure, South Africa. *Geology* **24**(10):913-916.

Koeberl C., Peucker-Ehrenbrink B., Reimold W. U., Shukolyukov A., and Lugmair G. W. 2002. Comparison of the osmium and chromium isotopic methods for the detection of meteoritic components in impactites: Examples from the Morokweng and Vredefort impact structures, South Africa. *Geological Society of America Special Paper* 356. pp. 607-617.

Koeberl C., Shukolykov A., and Lugmair G. W. 2007. Chromium isotopic studies of terrestrial impact craters: Identification of meteoritic components at Bosumtwi, Clearwater East, Lappajärvi, and Rochechouart. *Earth and Planetary Science Letters* **256**(3-4):534-546.

Koeberl C., Claeys P., Hecht L., and McDonald I. 2012. Geochemistry of impactites. *Elements* **8**:37–42.

Koeberl C., Mougel B., and Moynier F. 2017. Meteoritic component in melt rocks from the Boltysh (Ukraine) and Lonar (India) impact structures: First assessment (abstract #1331). *Lunar and Planetary Science XLVII*. CD-ROM.

Kondev F. G., Wang M., Huang W. J., Naimi S., and Audi G. 2021. The NUBASE2020 evaluation of nuclear physics properties. *Chinese Physics C* **45**:030001.

Lafuente A. L., González C., Quintana J. R., Vázquez A., and Romero A. 2008. Mobility of heavy metals in poorly developed carbonate soils in the Mediterranean region. *Geoderma* **145**(3-4):238-244.

Langenhorst F., and Deutsch A. 2012. Shock Metamorphism of Minerals. *Elements* **8**:31–36.

Lee S. R., Horton J. W. Jr., and Walker R. J. 2006. Confirmation of a meteoritic component in impact-melt rocks of the Chesapeake Bay impact structure, Virginia, USA – Evidence

from osmium isotopic and PGE systematics. *Meteoritics and Planetary Science* **41**(6):819–833.

Lorenz C. A. 1999. Trace elements geochemistry in impact melts of the Bolthysh Crater, Ukraine (abstract #1597), 30th *Lunar and Planetary Science Conference*. CD-ROM.

Loroch D., Deutsch A., Berndt J., and Bornemann A. 2016. The Cretaceous/Paleogene (K-Pg) boundary at the J Anomaly Ridge, Newfoundland (IODP Expedition 342, Hole U1403B). *Meteoritics and Planetary Science* **51**(7):1370-1385.

Luck J. M., Birck J. L., and Allegre C. J. 1980. ^{187}Re–^{187}Os systematics in meteorites: early chronology of the Solar System and age of the Galaxy. *Nature* **283**(5744):256–259.

Luguet A., Nowell G. M., and Pearson D. G. 2008. $^{184}Os/^{188}Os$ and $^{186}Os/^{188}Os$ measurements by negative thermal ionisation mass spectrometry (N-TIMS): Effects of interfering element and mass fractionation corrections on data accuracy and precision. *Chemical Geology* **248**:342–362.

Luterbacher H. P., and Premoli-Silva I. 1964. Biostratigrafia del Limite Cretaceo-Terziario nell'Appennino Centrale. *Rivista Italiana di Paleontologia* **70**:67–117.

Mader D., and Koeberl C. 2009. Using instrumental neutron activation analysis for geochemical analyses of terrestrial impact structures: Current analytical procedures at the University of Vienna geochemistry activation analysis laboratory. *Applied Radiation and Isotopes* **67**:2100–2103.

Mader D., Koeberl C., and Montanari, A. 2004. Geochemistry of Langhian pelagic marly limestone sequence of the Cònero Riviera, Ancona (Italy) and the search for a Ries impact signature: A process report. In: *Cratering in marine environments and on ice*, edited by Dypvik H., Claeys P., and Burchell M., Berlin-Heidelberg: pp. 149-184.

Makishima A. 2016. Thermal ionization mass spectrometry (TIMS): silicate digestion, separation, and measurement, Weinheim: Wiley-VCH Verlag. 361p.

Mark M. G. 1954. Stable isotope dilution as an analytical tool. *Annual Review of Nuclear Science* **4**:81-92.

Malavergne V., Charon E., Jones J., Cordier P., Righter K., Deldicque D., and Hennet L. 2016. The formation of nuggets of highly siderophile elements in quenched silicate melts at high temperatures: Before or during the silicate quench? *Earth and Planetary Science Letters* **434**:197-207.

Masaitis V. L. 1974. Some ancient meteorite craters of the USSR (in Russian). *Meteoritika* **33**:64-68.

Mason B. 1971. Handbook of elemental abundances in meteorites. New York: Gordon and Breach. 555 p.

Mason B. 1979. Cosmochemistry: Meteorites, Part 1. Data of Geochemistry. US Geological Survey Professional Paper 440-B-1.

McDonald I., Koeberl C., and Gurov E. P. 2009. A meteoritic component in melt rocks from the Boltysh impact structure, Ukraine: First assessment (abstract #1252), *40th Lunar and Planetary Science Conference*. CD-ROM.

McGetchin T. R., and Settle M. 1973. Radial thickness variation in impact crater ejecta: Implications for lunar basin deposits. *Earth and Planetary Science Letters* **20**(2):226-236.

Meisel T., and Moser J. 2004. Platinum-group element and rhenium concentrations in low abundance reference materials. *Geostandards and Geoanalytical Research* **28**:233–250.

Meisel T., Krähenbühl U., and Nazarov M. A..1995. Combined osmium and strontium isotopic study of the Cretaceous-Tertiary boundary at Sumbar, Turkmenistan: A test for an impact vs. a volcanic hypothesis. *Geology* **23**(4):313–316.

Meisel T., Moser J., Fellner N., Wegscheider W., and Schoenberg R. 2001. Simplified method for the determination of Ru, Pd, Re, Os, Ir and Pt in chromitites and other geological materials by isotope dilution ICP-MS and acid digestion. *The Analyst* **126**:322–328.

Meisel T., Walker R., Anthony J., Irving J., and Lorand J. P. 2001. Osmium isotopic compositions of mantle xenoliths: A global perspective. *Geochimica et Cosmochimica Acta* **65**(8):1311-1323.

Meisel T., Burnham M., Kriete C., Bokhari S., and Schulz T. 2013. Osmium isotope and PGE reference materials OKUM and MUH-1 (abstract). In *Mineralogical Magazine* **77**(5). Pp. 1734.

Melosh H. J. 1989. *Impact cratering: A geologic process*. New York: Oxford University Press. 245p.

Mittlefehldt D. W., See T. H., and Hörz F. 1992. Dissemination and fractionation of projectile materials in the impact melts from Wabar Crater, Saudi Arabia. *Meteoritics and Planetary Science* **27**(4):361-370.

Montanari A., Koeberl C. 2000. Impact stratigraphy: The Italian record. Lecture notes in Earth Sciences 93(3). Heidelberg: Springer Verlag. 363 p.

Morgan J. W., and Lovering J. F. 1967. Rhenium and osmium abundances in chondritic meteorites. *Geochimica et Cosmochimica Acta* **31**(10):1893-1909.

Morgan J. W., Higuchi H., Ganapathy R., and Anders E. 1975. Meteoritic material in four terrestrial meteorite craters. In: *Proceedings of the 6th Lunar Science Conference*. pp. 1609-1623.

Morgan J. W., Walker R. J., and Grossman J. N. 1992. Rhenium-osmium isotope systematics in meteorites I: magmatic iron meteorite groups IIAB and IIIAB. *Earth and Planetary Science Letters* **108**(4):191-202.

Mougel B., Moynier F., Koeberl C., Wielandt D., and Bizzarro M. 2019. *Meteoritics and Planetary Science* **54**(10):2592-2599.

Mountain B. W., and Wood S. A. 1988. Chemical controls on the solubility, transport, and deposition of platinum and palladium in hydrothermal Solutions: A thermodynamic approach. *Economic Geology* **83**(3):492-510.

Oberthür T., Weiser T. W., Gast L., and Kojonen K. 2003. Geochemistry and mineralogy of platinum-group elements at Hartley Platinum Mine, Zimbabwe. *Mineralium Deposita* **38**(3):327-343.

Osinski G. R., and Pierazzo E. 2012. Impact cratering: Processes and products. In: *Impact cratering*, edited by Osinski G. R., and Pierazzo E., Chichester: Wiley-Blackwell. pp. 43–59.

Ozdemir S., Schulz T., van Acken D., Luguet A. Reimold W. U., and Koeberl C. 2019. Meteoritic highly siderophile element and Re-Os isotope signatures of Archean spherule layers from the CT3 drill core, Barberton Greenstone Belt, South Africa. *Meteoritics and Planetary Science* **54**(10):2203-2216.

Palme H., Göbel E., and Grieve R. A. F. 1979. The distribution of volatile and siderophile elements in the impact melt of East Clearwater (Quebec). 10th Lunar and Planetary Science Conference Proceedings. pp. 2465-2492.

Palme H., Lodders K., and Jones A. 2014. 2.2 - Solar system abundances of the elements. In: *Treatise on geochemistry*, 2nd ed., edited by Holland H. D., and Turekian K. K. Oxford: Elsevier. pp. 15–36.

Pearson D. G., and Woodland S. J. 2000. Solvent extraction/anion exchange separation and determination of PGEs (Os, Ir, Pt, Pd, Ru) and Re–Os isotopes in geological samples by isotope dilution ICP-MS. *Chemical Geology* **165**:87–107.

Peucker-Ehrenbrink B., and Hannigan R. E. 2000. Effects of black shale weathering on the mobility of rhenium and platinum group elements. *Geology* **28**(5):475-778.

Peucker-Ehrenbrink B., and Jahn B. 2001. Rhenium-osmium isotope systematics and platinum group element concentrations: Loess and the upper continental crust. *Geochemistry, Geophysics, Geosystems* **2**:1061.

Peucker-Ehrenbrink B., and Ravizza G. 2000. The marine osmium isotope record. *Terra Nova* **12**(5):205-219.

Peucker-Ehrenbrink B., Ravizza G., and Hofmann A. W. 1995. The marine $^{187}Os/^{188}Os$ record of the past 80 million years. *Earth and Planetary Science Letters* **130**(1-4):155-167.

Pickersgill A. E., Mark D. F., Lee M. R., Kelley S. P., and Jolley D. W. 2021. The Boltysh impact structure: An early Danian impact event during recovery from the K-Pg mass extinction. *Science Advances* **7**:1–10.

Pingitore N. E. Jr. 1982. The role of diffusion during carbonate diagenesis. *Journal of Sedimentary Petrology* **52**:227-39.

Rehkämper M., and Halliday A. N. 1997. Development and application of new ion-exchange techniques for the separation of the platinum group and other siderophile elements from geological samples. *Talanta* **44**:663–672.

Reiners P. W., Carlson R. W., Renne P. R., Cooper K. M., Granger D. E., McLean N. M., and Schoene B. 2018. Geochronology and thermochronology. Oxford: John Wiley & Sons. 482 p.

Renne P. R., Deino A. L., Hilgen F. J., Kuiper K. F., Mark D. F., Mitchell W. S., Morgan L. E., Mundil R., and Smit J. 2013. Time scales of critical events around the Cretaceous-Paleogene boundary. *Science* **339**:684–687.

Richards M. A., Alvarez W., Self S., Karlstrom L., Renne P. R., Manga M., Sprain C. J., Smit J., Vanderkluysen L., and Gibson S. A. 2015. Triggering of the largest Deccan eruptions by the Chicxulub impact. *Geological Society of America Bulletin.* **127**(11-12):1507-1520.

Robinson N., Ravizza G., Coccioni R., Peucker-Ehrenbrink B., Norris R. 2009. A high-resolution marine $^{187}Os/^{188}Os$ record for the late Maastrichtian: Distinguishing the chemical fingerprints of Deccan volcanism and the KP impact event. *Earth and Planetary Science Letters* **281**(3-4):159-168.

Rollinson H., and Pease V. 2021. *Using geochemical data: to understand geological processes,* 2nd ed. Cambridge: Cambridge University Press. 286p.

Schmidt G. 1997. Clues to the nature of the impacting bodies from platinum-group elements (rhenium and gold) in borehole samples from the Clearwater East crater (Canada) and the Boltysh impact crater (Ukraine). *Meteoritics and Planetary Science* **32**:761–767.

Schmidt G., and Palme H. 1997. Abundances of Os, Ir, Ru, Rh, Pt, and Pd in the Earth's crust. In: *The origin and fractionation of highly siderophile elements in the Earth's mantle,* edited by Brügman G., Lorand J. P., and Palme H., Mainz: European Association of Geochemistry Workshop 1997. pp. 71-72.

Schmidt G., and Pernicka E. 1994. The determination of platinum group elements (PGE) in target rocks and fall-back material of the Nördlinger Ries impact crater (Germany). *Geochimica et Cosmochimica Acta* **58**:5083-5090.

Schmidt G., Palme H., and Kratz K. L. 1997. Highly siderophile elements (Re, Os, Ir, Ru, Rh, Pd, Au) in impact melts from three European impact craters (Sääksjärvi, Mien and Dellen): Clues to the nature of the impacting bodies. *Geochimica et Cosmochimica Acta* **61**(14):2977-2987.

Schmitz B., and Asaro F. 1996. Iridium geochemistry of volcanic ash layers from the early Eocene rifting of the northeastern North Atlantic and some other Phanerozoic events. *Geological Society of America Bulletin* **108**(4):489-504.

Schulte P., Alegret L., Arenillas I., Arz J. A., Barton P. J., Bown P. R., Bralower T. J., Christeson G. L., Claeys P., Cockell C. S., Collins G. S., Deutsch A., Goldin T. J., Goto K., Grajales-Nishimura J. M., Grieve R. A., Gulick S. P., Johnson K. R., Kiessling W., Koeberl C., Kring D. A., MacLeod K. G., Matsui T., Melosh J., Montanari A., Morgan J. V., Neal C. R., Nichols D. J., Norris R. D., Pierazzo E., Ravizza G., Rebolledo-Vieyra M., Reimold W. U., Robin E., Salge T., Speijer R. P., Sweet A. R., Urrutia-Fucugauchi J., Vajda V., Whalen M. T., and Willumsen P. S. 2010. The Chicxulub asteroid impact and mass extinction at the Cretaceous-Paleogene boundary. *Science* **327**(5970):1214-1218.

Schulz T., Luguet A., Wegner W., van Acken D., and Koeberl C. 2016. Target rocks, impact glasses, and melt rocks from the Lonar crater, India: Highly siderophile element systematics and Sr-Nd-Os isotopic signatures. *Meteoritic and Planetary Science* **51**(7):1323-1339.

Shaw T. J., Gieskes J. M., and Jahnke R. A. 1990. Early diagenesis in differing depositional environments: The response of transition metals in pore water. *Geochimica et Cosmochimica Acta* **54**(5):1233-1246.

Shen J. J., Papanastassiou D. A., and Wasserburg G. J. 1996. Precise Re-Os determinations and systematics of iron meteorites. *Geochimica et Cosmochimica Acta* **60**(15):2887-2900.

Shiraki K. 1997. Geochemical behavior of chromium. *Resource Geology* **47**(6):319-330.

Shirey S. B., and Koeberl C. 1997. Re-Os isotope systematics as a diagnostic tool for the study of impact craters and distal ejecta. *Palaeogeography, Palaeoclimatology, Palaeoecology* **132**(1-4):25–46.

Shirey S. B., and Walker R. J. 1998. The Re-Os isotope system in cosmochemistry and high-temperature geochemistry. *Annual Review of Earth and Planetary Science* **26**:432-500.

Shoemaker E. M. 1987. Meteor Crater, Arizona. In: *Rocky Mountain section of the Geological Society of America (Centennial Field Guide Volume 2)*, edited by Beus S. S., Boulder: Geological Society of America. pp. 399-404.

Shukolyukov A., and Lugmair G. W. 1998. Isotopic evidence for the Cretaceous-Tertiary impactor and its type. *Science* **282**(5390):927–929.

Shukolyukov A., and Lugmair G. W. 2006. Manganese-chromium isotope systematics of carbonaceous chondrites. *Earth and Planetary Science Letters* **250**:200-213.

Sinnesael M., De Vleeschouwer D., Coccioni R., Claeys P., Frontalini F., Jovane L., Savian J. F., and Montanari A. 2016. High-resolution multiproxy cyclostratigraphic analysis of environmental and climatic events across the Cretaceous-Paleogene boundary in the classic pelagic succession of Gubbio (Italy). In: *The Stratigraphic record of Gubbio: Integrated stratigraphy of the late Cretaceous–Paleogene Umbria-Marche pelagic basin,* edited by Menichetti M., Coccioni R., and Montanari A., Boulder: Geological Society of America Special Paper 524. pp. 115-137.

Sinnesael M., De Winter N. J., Snoeck C., Montanari A., and Claeys P. 2018. An integrated pelagic carbonate multi-proxy study using portable X-ray fluorescence (pXRF): Maastrichtian strata from the Bottaccione Gorge, Gubbio, Italy. *Cretaceous Research* **91**:20–32.

Sinnesael M., Montanari A., Frontalini F., Coccioni R., Gattacceca J., Snoeck C., Wegner W., Koeberl C., Morgan L.E., de Winter N.J., DePaolo D.J., and Claeys P. 2019. Multiproxy Cretaceous-Paleogene boundary event stratigraphy: An Umbria-Marche basinwide perspective. In: *250 million years of Earth history in central Italy: Celebrating 25 years of the geological observatory of Coldigioco*, edited by Koeberl C., and Bice D. M., Boulder: Geological Society of America Special Paper 542. pp. 133–158.

Smoliar M., Walker R. J., and Morgan J. W. 1996. Re-Os ages of group IIA, IIIA, IVA, and IVB iron meteorites. *Science* **271**(5252):1099-1102.

Sprain C. J., Renne P. R., Clemens W. A., and Gregory P. W. 2018. Calibration of chron C29r: New high-precision geochronologic and paleomagnetic constraints from the Hell Creek region, Montana. *Geological Society of America Bulletin* **130**(9-10):1615-1644.

Stöffler D., and Grieve R. 2007. Impactites. In: *Metamorphic rocks*, edited by Fettes D., and Desmons J., Cambridge: Cambridge University Press. pp. 82–92.

Stosch H. G. 2016. Neutron activation analysis of the rare earth elements (REE) – With emphasis on geological materials. *Physical Sciences Reviews* **1**:20160062.

Sun W., Zhi X., Peng Z., Wang Z., Ge N., and Zhou X. 1998. Os isotopic composition of the earth's primitive upper mantle. *Science Bulletin* **43**(18):1575-1579.

Tagle R., and Berlin J. 2008. A database of chondrite analyses including platinum group elements, Ni, Co, Au, and Cr: Implications for the identification of chondritic projectiles. *Meteoritics and* **43**(3):541-559.

Tagle R., and Hecht L. 2006. Geochemical identification of projectiles in impact rocks. *Meteoritics and Planetary Science* **41**(11):1721-1735.

Taylor S. R., and McLennan S. M. 1985. *The continental crust: its composition and evolution*, Oxford: Blackwell Scientific Publications. 312 p.

Taylor S. R., and McLennan S. M. 1995. The geochemical evolution of the continental crust. *Reviews of Geophysics* **33**(2):241-265.

Trinquier A., Birck J. -L., Allègre C. J., Göpel C., and Ulfbeck D. 2008. ^{53}Mn–^{53}Cr systematics of the early Solar System revisited. *Geochimica et Cosmochimica Acta* **72**(20):5146-5163.

Turekian K. K. 1982. Potential of ^{187}Os/^{186}Os as a cosmic versus terrestrial indicator in high iridium layers of sedimentary strata. In: *Geological implications of impacts of large asteroids and comets on the Earth*, edited by Silver L. T., and Schultz P. H., Boulder: Geological Society of America Special Paper 190. pp. 243-249.

Turekian K. K., and Wedepohl K. H. 1961. Distribution of the elements in some major units of the Earth's crust. *Geological Society of America Bulletin* **72**(2):175-191.

Vanhaecke F., and Degryse P. 2012. *Isotopic analysis: fundamentals and applications using ICP-MS*, Weinheim, Germany: Wiley-VCH Verlag. 555 p.

Völkening J., Walczyk T., and Heumann K. 1991. Osmium isotope ratio determinations by negative thermal ionization mass spectrometry. *International Journal of Mass Spectrometry and Ion Processes* **105**:147–159.

Walker R. J., and Morgan J. W. 1989. Rhenium-Osmium systematics of carbonaceous chondrites. *Science* **243**(4890):519-522.

Walker R. J., Horan M. F., Becker H., Grossman J. N., and Rubin A. E. 2002. Comparative ^{187}Re-^{187}Os systematics of chondrites: Implications regarding early solar system processes. *Geochemica et Cosmochimica Acta* **66**:4187–4201.

Wasson J. T. 1985. Meteorites: Their record of early solar-system history. New York: Freeman. 267 p.

Weisberg M. K., McCoy T. J., and Krot A. N. 2006. Systematics and evaluation of meteorite classification. In: *Meteorites and the early solar system II*, edited by Lauretta D. S. and Sween H. Y. Tucson: University of Arizona Press. pp. 19–52.

Wimpenny J., Gannoun A., Burton K. W., Widdowson M., James R. H., and Gíslason S. R. 2007. Rhenium and osmium isotope and elemental behaviour accompanying laterite formation in the Deccan region of India. *Earth and Planetary Science Letters* **261**(1-2):239-258.

Van Acken D., Brandon A. D., and Lapen T. J. 2012. Highly siderophile element and osmium isotope evidence for postcore formation magmatic and impact processes on the aubrite parent body. *Meteoritics and Planetary Science* **47**(10):1606-1623.

Xiong Y., and Wood S. A. 1999. Experimental determination of the solubility of ReO_2 and the dominant oxidation state of rhenium in hydrothermal solutions. *Chemical Geology* **158**(3-4):245-256.

List of Tables

List of Figures

Appendix

Table A1. Analyses of major elements and trace element contents of various Boltysh melt rocks and basement rocks determined with EMP and INAA; after Grieve et al. (1987).

	Melt rocks					**Basement**	
	1	**2**	**3**	**4**	**5**	**6**	**7**
SiO_2 [wt%]	69.44	68.31	68.51	68.75	68.09	68.53	70.27
TiO_2	0.41	0.41	0.40	0.41	0.35	0.49	0.40
Al_2O_3	14.31	14.42	14.28	14.34	14.07	14.84	13.72
Fe_2O_3	2.10	1.37	0.62	1.36	1.28	1.38	1.38
FeO	1.03	1.93	2.50	1.83	2.26	2.23	2.76
MnO	0.02	0.04	0.05	0.04	0.07	0.04	0.04
MgO	1.13	1.33	1.24	1.24	1.41	0.50	1.08
CaO	1.95	2.00	1.92	1.96	2.04	1.33	1.40
Na_2O	3.26	4.00	3.40	3.55	3.20	2.86	2.87
K_2O	4.68	3.26	4.00	3.98	3.95	7.00	4.88
P_2O_5	0.16	0.15	0.14	0.15	0.17	0.12	0.15
S	0	0	0.02	0.01	-	0.01	0.01
Total	98.49	97.22	97.08	97.62	96.89	99.33	97.82
Ba [ppm]	712	707	695	705	547	1123	803
Cr	52	58	57	56	24	26	2
Zr	178	166	179	174	-	273	-
Sr	209	204	210	208	203	218	170
Rb	183	174	179	179	185	265	250
Y	16	13	13	14	-	29	-
Nb	10	23	11	15	-	16	-
Zn	54	55	58	56	-	143	-
Ni	40	46	44	43	58	16	4
V	35	36	34	35	-	12	-
Co	20	18	25	21	5	25	2

Boltysh melt rocks from drill core B50 (in depths between 580-595m) and B11475(in a depth of about 793m) which were analyzed by Grieve et al. (1987): ***1*** *Average of 6 microcrystalline matrix rocks;* ***2*** *Average of 3 fresh glassy matrix rocks;* ***3*** *Average of 4 devitrified glassy matrix rocks;* ***4*** *Average of 13 melt rocks, analyzed here;* ***5*** *Average of major element contents in 52 and trace element contents in 13 melt rocks (Gurov et al. 1986);* ***6*** *Average of 4 basement samples analyzed in Grieve et al. (1987);* ***7*** *Average of major elements in 40 and trace elements in 3 basement samples (Gurov et al. 1986). Total Fe as FeO. Major element concentrations are given in wt% and trace element concentrations are given in ppm.*

Oxygen Correction

Oxygen has three natural isotopes, ^{16}O, ^{17}O, and ^{18}O, which are present in different relative abundances. Because all oxygen isotopes bond with the Os in the sample, the total mass of the osmium oxide is affected. Therefore, an oxygen isotope composition interference correction was applied (Luguet et al. 2008). The oxygen and osmium isotope abundances were taken from Kondev et al. (2021).

Wet Chemistry Recipes

The samples were loaded onto pre-cleaned Biorad® AG1-X8 100-200# (1 ml) anion exchange resin in Biorad® polypropylene columns with a 10 ml reservoir. After treatment with several acids (HCl and HNO_3), the PGE elements were eluted, separated from each other, and collected in two steps, yielding Re-Ir-Pt-Ru samples and Pd samples (e.g., Pearson and Woodland 2000; Rehkämper and Halliday 1997). These samples underwent a second chromatography using LN-Spec columns and 1M HCl for further purification. After evaporation at 70°C, the samples are ready for mass spectrometry. For more details see Figure A1.

OKUM Reference material

Table A2. Average Re, Os, Ir, Pt, Ru, and Pd concentrations obtained in OKUM (komatiite) using the high-pressure asher isotope dilution technique compared with literature data.

OKUM (komatiite)	Ru	Pd	Re	Os	Ir	Pt
Measured average (n=8)	4.04 ± 0.27	13.08 ± 0.96	0.46 ± 0.01	0.92 ± 0.02	0.86 ± 0.02	12.4 ± 1.3
Certificate Geo Labs (2001)	4.25 ± 0.30	11.7 ± 0.5	-	-	0.99 ± 0.07	11.0 ± 0.6
Savard et al. (2010)	4.15 ± 0.05	12.20 ± 0.73	0.566 ± 0.04	0.790	0.943 ± 0.04	11.44 ± 0.22
RSD	1.3%	3.5%	9.8%	7.6%	4.6%	4.0%

HSE Column Chemistry	
ANION COLUMN (1ml AG1-X8 Resin)	
Resin Cleaning	10 ml H2O
	10 ml 6M HNO3
	10 ml conc. HCl
	2 ml H2O
Equilibration	2 ml 1M HCl
	2 ml 0.5M HCl
Load sample	10 ml 0.5M HCl
	5 ml 1M HCl
	2 ml 0.8 M HNO3
	2ml 0.8 M HNO3
Collect Re-Ir-Pt-Ru	15ml conc. HCl
	2 ml H2O
Collect Pd	15ml conc. HCl
Collect Pd	10 ml conc. HCl
Collect Pd	10 ml conc. HCl
Dried down and both cuts redissolved in 1 ml 1M HCl	

LN-Spec COLUMN	
Resin cleaning	4 ml H20
	4 ml 6M HCl
	4 ml 6M HCl
	4 ml 2M HF
	4 ml 6M HCl
	4 ml 2M HF
	4 ml H20
Equilibration	4 ml 1M HCl
Load and Collect Pd	1 ml 1M HCl
Collect Pd	4 ml 1M HCl
Load and collect Re-Ir-Pt-Ru	1 ml 1M HCl
Collect Re-Ir-Pt-Ru	5 ml 1M HCl
Cleaning	4 ml 2M HF
	4 ml 2M HF
	4 ml 6M HCl
	4 ml 2M HF
	4 ml 6M HCl
	4 ml 2M HF

Figure A1. Detailed recipe for the chromatographic exchange chemistries.